LINKING PHOTOSYNTHETIC AND CARBON METABOLISM IN MICROALGAE FOR BIOFUEL APPLICATIONS

By

ANAGHA KRISHNAN

A dissertation submitted to the

Graduate School-New Brunswick

Rutgers, The State University of New Jersey

and

The Graduate School of Biomedical Sciences

In partial fulfillment of the requirements

For the degree of

Doctor of Philosophy

Graduate Program in Microbiology and Molecular Genetics

Written under the direction of

G. Charles Dismukes

And approved by

_____

_____

_____

_____

New Brunswick, New Jersey

JANUARY, 2016

ABSTRACT OF THE DISSERTATION

Linking photosynthetic and carbon metabolism in microalgae for biofuel applications

By ANAGHA KRISHNAN

Dissertation Director:

Dr. G. Charles Dismukes

Microalgae predominantly partition photosynthetically fixed carbon into proteins, starch and lipids. Of these, carbohydrates and lipids are desired as they are the precursors for biofuel production. Photosynthetic electron transport is closely coupled to carbon partitioning, thus frustrating efforts to substantially increase the yield of the desired terminal product without compromising photosynthetic fitness. The objective of this thesis was to investigate the role of starch biosynthesis with respect to photosynthesis and carbon partitioning in a model microalga *Chlamydomonas reinhardtii*. For this, I have used a series of starch deficient mutants together with nitrogen deprivation to modulate the normal carbon partitioning. Nitrogen deprivation is known to redirect biosynthesis away from proteins to starch and lipids, and towards lipids in mutants lacking starch biosynthesis genes. Starch-deficient mutants showed a 20-40% lower biomass accumulation under both nutrient replete and deplete conditions. Interrogation of the photosynthetic metabolic flux (water→PSII/PSI→ ATP & NADPH → 3PG) revealed that above a threshold light intensity, starch deficiency attenuated NADPH reoxidation by the Calvin-Benson-Bassham (CBB) cycle, which attenuated water oxidation at PSII by product inhibition. Even with starch biosynthesis blocked in the starch-deficient mutant, a high gluconeogenic flux was maintained by redirecting carbon

through the oxidative pentose phosphate (OPP) shunt and ultimately away from starch. Thus, upon loss of the ability to synthesize starch, water oxidation is attenuated to balance energy consumption, while the OPP shunt becomes the dominant pathway for repartitioning of the residual photosynthate that can be produced.

The goal of the second part of the thesis was to use metabolic principles to develop a cyanobacterial mutant capable of attaining high H_2 yield. Cyanobacteria catabolize the photosynthetically assimilated glycogen under anaerobic auto-fermentative conditions and produce hydrogen via the enzyme, hydrogenase. By sequentially enhancing the glycolytic rate together with the elimination of competing pathways in a euryhaline cyanobacterium, *Synechococcus sp*. PCC 7002 mutant with high hydrogenase gene expression, we were able to boost H_2 production by 8-fold over the wild-type strain.

Thus, my dissertation, addresses understanding how to control the metabolism of photosynthetic microbes and using targeted metabolic engineering to transform microalgae into efficient cell factories for biofuel production.

ACKNOWLEDGEMENTS

Ph.D is a group activity and I want to thank everyone involved in mine. I am deeply grateful to my advisor, Dr. G. Charles Dismukes for his patience, guidance and teaching, that made me look at biology from a chemistry point of view. His attention to details, perfectionism and professionalism is what I hope to imbibe and take back with me from this Ph.D. In addition, I would like to thank the members of my dissertation committee, Dr. Desmond Lun, Dr. Pal Maliga and Dr. Robert Niedermann and for their encouragement in completing this dissertation work. I have to also thank Dr. Andrew Vershon (MMG program director) for his constant support. In addition, I need to make a special mention of my undergraduate thesis mentor, Dr. Sharmila Bapat and my Teaching Assistantship mentor, Dr. Susan Skelly, for their guidance and advice.

I am indebted to a number of people who have helped me through the course of my Ph.D. I thank Dr. Matthew Posewitz and Huiya Gu for their help and contribution towards my *Chlamydomonas* work and Dr. Donald Bryant and Dr. Shuyi Zhang for the cyanobacterial project. I need to acknowledge all my lab mates, past and present, in the Dismukes Lab for their friendship. I would like to specially thank Nick Skizim for being my first mentor and introducing me to the world of H_2. In addition, I am extremely grateful for Drs. Elizabeth Burrows and David Vinyard for having been a very significant part of my journey. Dr. Kumaraswamy Kenchappa, apart from being a significant co-author on my work, has been my friend and guide through the ups and downs of Ph.D. I have to thank Prof. Gennady Ananyev for letting me use all of his amazing instruments even after I ended up breaking multiple of his LEDs. I have to thank Drs. Tiago Guerra, Kelsey McNeely and Nick Bennette for their guidance. Xiao Qian, Yuan Zhang and Colin Gates have been constant companions in my metabolic quest. Finally, the other members of the Dismukes' chemistry subgroup, David Robinson, Clyde Cady, Paul Smith, Graeme Gardner and Anders Laursen for their perspectives that enable me to make my presentations comprehensible to a broader audience

I need to make a special mention of my friends Ashish Bohora, Abhijit Ambegaonkar, Moulik Balasubramanian, Arunika Das, Ved Datar, Aishwarya Deshpande and Chetan Tonde for having made my life fun and comfortable for the last six years.

My acknowledgement would be incomplete without me thanking my parents, Mr. A. Krishnan and Mrs. Mala Krishnan and my dearest brother Ajay Krishnan, who were the rock that supported me in turbulent times. Without their encouragement, I would not come to my current position. Last but not the least, I have to thank my loving husband, Shashank Kanade, whose unwavering confidence and companionship made be capable of tiding over any wave.

Lastly, part of my doctoral work was supported by multiple doctoral grants from the Waksman Institute (Charles-Joanna Busch Fellowship and Benedict-Michael fellowship) and Koft-Umbreit Fellowship for summer research which is gratefully acknowledged. The work was supported by Air Force Office of Scientific Research (MURI grant FA9550-05-1-0365).

Table of Contents

Table of Figures

Table of Tables

Table of Schemes

Chapter I: Introduction

1. Background: Microalgae for biofuels

Microalgae are a diverse group of fast growing, microorganisms comprising of free living, photosynthetic, prokaryotic or eukaryotic organisms that can convert CO_2 into potential bioproducts. Occupying a diverse range of habitats, microalgae have developed enormous metabolic flexibility (Richmond, 2004), (Hu *et al.*, 2008) and contribute to half of the global photosynthetic activity (Wiessner *et al.*, 1995). The concept of using microalgae as biofuel feedstock gained importance during the oil embargo in the 1970s, with the Department of Energy establishing the 'Aquatic Species Program' (Sheehan, 1998). Originally, only the carbohydrate fraction of microalgae was suggested as a feedstock for biogas production (Meier, 1955). However, later on, it was found that nutrient stressed microalgae could accumulate lipids (triacylglycerols and diacylglycerols) which could be harvested and directly used as fuels. With recent advances in metabolic engineering, microalgae have become excellent platforms to produce designer biofuels in addition to inherent metabolic products such as oils, starch and H_2 (Sheehan, 1998),(Schenk *et al.*, 2008), (Dismukes *et al.*, 2008), (Rittmann, 2008; Gimpel *et al.*, 2013), (Radakovits *et al.*, 2010), (Hannon *et al.*, 2010), (Hu *et al.*, 2008), (Chisti, 2008), (Brennan *et al.*, 2010), (Brune *et al.*, 2009). Especially from a biofuels standpoint, a diverse range of fuel precursors have been produced at least at the pilot scale including but not limited to : 1) biodiesel through transesterification (Chisti, 2007), (Hu *et al.*, 2008), (Miao *et al.*, 2004)., 2) photobiological and fermentative bioH_2 production (Melis, 2002), 3) biomethane production through anaerobic digestion (McKendry, 2002),(McKendry, 2002), 4) bioethanol through alcoholic fermentation, 5) bio-oil and syngas through thermochemical liquefaction and pyrolysis (McKendry, 2002), (Miao *et al.*, 2004) and 6) electricity through direct combustion (Brennan *et al.*, 2010). The enormous metabolic flexibility of microalgae allows the use of both aerobic and anaerobic metabolisms for biofuel production.

Besides being the most productive phototrophic organisms, microalgae also confer additional advantages over the existing terrestrial agricultural/forest biomass sources. Unlike terrestrial crops, microalgae are a) devoid of recalcitrant woody matter (cellulose) (Wijffels *et al.*, 2010), (Georgianna *et al.*, 2012), (Dismukes *et al.*, 2008) b) can be cultivated in marginal, saline or wastewater throughout the year without seasonal constraints and c) can thrive in light environments not used by terrestrial plants. Finally, algal biofuels can be produced locally making them a viable alternative for developing countries as well as providing energy security.

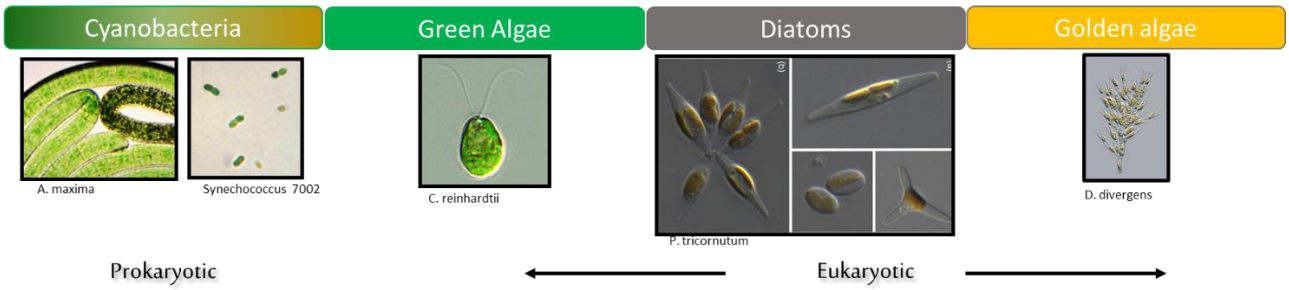

Figure 1-1 Representative examples of microalgae

Many microalgal species are known to accumulate about (20-50) % of their cellular dry weight as lipids such as triacylglycerols and diacylglycerols (Griffiths *et al.*, 2009), (Chisti, 2007), (Tornabene *et al.*, 1983). These lipids can yield biodiesel through transesterification or on further distillation and cracking can yield gasoline or jet fuel. Current yields for the existing wild strains are about 20 g $m^{-2}day^{-1}$ equaling 60-70 dry tons per hectare per year of biomass or 20 tons of oil useful for biodiesel production. These yields are over 10 times higher than any other dry land crops such as Jatropha or Castor, and 3 to 4 times higher than those achieved with oil palm which requires irreplaceable rain forest habitat. Algae also have important implications from the overall land usage. Algae required to replace 1200 billion liters of petroleum used by the United States can be cultivated on only 30 million hectares and can yield upto 40,000 liters per hectare per year (Georgianna *et al.*, 2012). Additionally, algal products have many alternative markets including animal/fish feedstock, nutrichemicals and industrial chemical precursors that provide economic stability for investment.

2. Technological barriers to algal biofuels

High growth rates, reasonable growth densities and high oil contents have all been cited as reasons to invest significant capital to turn algae into biofuels. Numerous technoeconomic analyses of algal oil production costs have already been conducted (Venteris *et al.*, 2013). Cost data for the year 2008, estimated the US cost between \$10.87 $gallon^{-1}$ and \$13.32 $gallon^{-1}$ (Sun *et al.*, 2011) with recent reports from the National Alliance for Advanced Biofuels and Bioproducts (NAABB) consortium claiming further reduction to \$8 $gallon^{-1}$. Yet, the current costs make algal biofuels less competitive in comparison to fossil fuels and without further improvements, microalgal fuels are economically unviable. It is a widely accepted fact that the current technology is limited by

a) developing suitable algal strains: in terms of oil productivity, crop protection, nutrient and resource allocation, and the production of co-products

b) process development to harvest biomass and extract biofuel precursors (Fishman *et al.*, 2010), (Hannon *et al.*, 2010).

The current solar to biomass conversion efficiency of microalgae (3%) fall well short of the theoretical upper limit (8-10%) (Melis, 2009). In addition, the higher lipid accumulators (more suitable for biofuel production) have been empirically found to possess lower growth rates. This led to the prediction that significant improvements in biofuel production are possible only through better understanding of algal physiology and carbon partitioning which will enable the development of robust transgenic strains that produce high levels of lipids without compromising fitness. This topic is a rich area of research that is yielding significant progress as reported in scientific journals. Significant improvements in growth, crop protection against heat stress and parasitic contamination and in lipid production is projected to reduce the production cost further to \$4.5 gallon $^{-1}$ (Hannon *et al.*, 2010), (Pienkos *et al.*, 2009). For this, a thorough understanding of the molecular mechanisms and the feedbacks underlying microbial conversion pathways is essential.

3. Photoautotrophic growth and carbon allocation for high lipid production

3.1) Nutrient starvation for lipid production and modification of carbon partitioning

In microalgae, biomass composition and therefore, the amount of lipid accumulated is highly dependent on environmental and growth conditions (Becker, 1994). Under favorable growth conditions, even the known oleaginous algae produce very low amounts of triacyl glycerols (TAG) (Liang *et al.*, 2013), (Becker, 1994). Only on the exposure to stress, either chemical or physical, does large amounts of TAG accumulation occurs (Sharma *et al.*, 2012). Nutrient starvation, especially nitrogen starvation is one of the most widely and successfully applied methods to induce and increase the lipid production by up to 53% (Sharma *et al.*, 2012). Upon N starvation, protein and nucleic acid synthesis is inhibited, while the photosynthetic electron transport chain remains active, albeit at lower efficiencies. To prevent the overreduction of the electron transport chain,

various algae accumulate energy-rich storage compounds such as starch and storage lipids (TAGs) (Guschina *et al.*, 2006), (Siaut *et al.*, 2011), (Hu *et al.*, 2008), (Li *et al.*, 2010),(Rodolfi *et al.*, 2009), (Wang *et al.*, 2009), (Moellering *et al.*, 2010), (Work *et al.*, 2010), (Fan *et al.*, 2011). On imposing N starvation, there is a shift in allocation of carbon from proteins to starch and lipids making nitrogen starvation an excellent method to study biosynthetic remodeling. Understanding of the carbon decision tree - the temporal and spatial coordination of biochemical pathways responsible for biosynthesis and catabolism of the major carbon sinks - is in part the focus of this thesis.

3.2) Microalgal energetics and central carbon metabolism under photoautotrophic conditions

Photosynthesis is the fundamental process that converts solar energy into chemical energy where ATP and NADPH produced by the "light reactions" of photosynthesis fuel the "light-independent reactions" of carbon fixation. Photosynthetically fixed carbon enters central carbon metabolism and a series of enzymatic reactions convert the carbon into metabolic precursors that are destined for biopolymers such as lipids, proteins and carbohydrates.

Photosynthesis: The photosynthetic electron transport chain begins with water oxidation at Photosystem II (PSII). Electrons from water are transferred through a series of electron carriers to Photosystem I (PSI). Simultaneously, the excitation of PSI relays electrons via a second series of carriers, ultimately reducing ferredoxin (Fd). Ferredoxin-NADP+ reductase (FNR) use ferredoxin as the substrate for reducing NADP+ to NADPH. Photosynthetic electron transport also establishes a proton (H+) gradient across the thylakoid lumen that is used for generating ATP. As a major photosynthetic electron sink under photoautotrophic conditions, the Calvin-Benson-Basham cycle (CBB cycle) uses two NADPH and three ATP molecules to fix one CO2 molecule into 3-phosphoglycerate (3PG). Triose phosphates (Triose-P) generated in the CBB cycle are directed to three major carbon sinks: carbohydrates, amino acids and lipids. Even though the light-driven redox chemistry of light reactions and the enzymatic reactions of metabolism are spatially separated, they are tightly coupled and necessary for the balancing of ATP and NADPH (Ott *et al.*, 1999). This

form of self-regulation protects the photosystems from irreversible damage. Changing the carbon partitioning will have a direct impact on photosynthetic efficiency and ultimately algal yield.

Terminal sinks and energetics under photoautotrophic conditions: The primary product of CO_2 fixation 3PG enters into central carbon metabolism and is ultimately destined to either a structural or a storage biopolymer or used for energy generation and cell homeostasis. Central carbon metabolism is composed of multiple sub-pathways including the Calvin Benson Bassham cycle (CBB), glycolysis, gluconeogenesis, the oxidative pentose phosphate pathway (OPP), and the tri-carboxylic acid (TCA) cycle.

Under standard growth conditions, the major sinks for fixed carbon are proteins, cell wall carbohydrates and membrane lipids (Boyle *et al.*, 2009). While under stress conditions, energy-rich storage compounds such as starch and storage lipids (oil) become the dominant sinks. All the energy stored in the biopolymers is either directly or indirectly originating from light when algae is grown under photoautotrophic conditions. The ATP and NADPH originating from the light reaction are also used for other processes than to produce terminal biopolymers, e.g. to reducing nitrogen and sulfur as well as cell homeostasis. The energetic requirement of each of the terminal sinks is one of the key factors that governs the amount of energy partitioned between the storage sink and the cellular growth leading to variations in growth rates. The energy consumption makes central carbon metabolism a key link in solar to biomass energy conversion in microalgae.

Based on the metabolic pathways used for the sink generation, thermodynamically, lipids are the most expensive terminal product while starch is the least energy requiring product. Glucose derived by the condensation of 3PG is polymerized to starch and requires 4.2 ATP/C and 2 NADPH/C polymerized (Subramanian *et al.*, 2013), (Raven, 1982), while the energetic requirement for TAG/structural lipid biosynthesis ranges from 5.84 ATP/C and 2.84 NADPH/C to 6.3 ATP/C and 2.9 NADPH/C (Subramanian *et al.*, 2013), (Raven, 1982). On the other hand, protein biosynthesis in a freshwater algae requires about 4.98 ATP/C and 2.77 NADPH/C (Raven,

1982). Typical algal (total) biomass productivities range from 15-30 g dry weight m^{-2} day^{-1} (Batan *et al.*, 2010), containing about (Campbell *et al.*, 2011) 4.3 to 7.0 kcal/gdw (Illman *et al.*, 2000), (Williams *et al.*, 2010). Typically, the oleaginous strains have higher energy densities (Subramanian *et al.*, 2013). Consistent with the thermodynamic requirements, there is a trade-off between cell division rates and the accumulation of the storage products. Typically, organisms with higher lipid densities have slower growth rates. Nonetheless, it is important to note that product generation is not purely governed by thermodynamic constraints but by a number of other factors including the light absorption spectrum, size/orientation of the light harvesting complex, efficiency of photon absorption and energy transfer, kinetic rate constants of the various electron transfer reactions, availability of substrate metabolites, metabolic compartmentalization and feedback control, respiration rates, and the partitioning of reduced carbon between new cell growth and division and energy storage (Cardol *et al.*, 2011), (Radakovits *et al.*, 2010). Thus, both kinetic and thermodynamic constraints need to be taken into account while optimizing biofuel production by microalgae and improving microalgal strain performances definitely requires a better understanding of the mechanisms and regulation of carbon fixation and carbon allocation between biosynthetic pathways.

4. Fermentative metabolism and carbon allocation for high H_2 production

Though microalgae have a dominant aerobic metabolism that uses oxygen dependent respiration and photosynthesis for energy generation, certain algal species have retained their original ability of anaerobic fermentation. Together with using microalgae for lipid/biomass production, microalgae can also be used for bioH_2 production by harnessing the fermentative metabolic capacity. H_2 is a clean fuel and burns without releasing CO_2. Unlike the previously described eukaryotic algae, prokaryotic cyanobacteria, prefer to follow dark fermentation preceding the photoautotrophic growth and produce H_2. Cyanobacteria possess a heteropentameric enzyme called hydrogenase catalyzing the reversible reaction

$$2H^+ + NAD(P)H \leftrightarrow H_2 + NAD(P)^+$$

The second part of the thesis (Chapter 4) addresses fermentative metabolism in the prokaryotic microalgae cyanobacteria, and how metabolic engineering can be effectively used to improve fermentative H_2 production by cyanobacteria.

4.1) Microalgal energetics and the central carbon metabolism under fermentative conditions

Anaerobic metabolism under dark anoxic conditions is initiated by degradation of photosynthetically assimilated glycogen into monomeric glucose molecules that can either enter the pentose phosphate pathway or undergo glycolytic breakdown (Fig. 1-2).

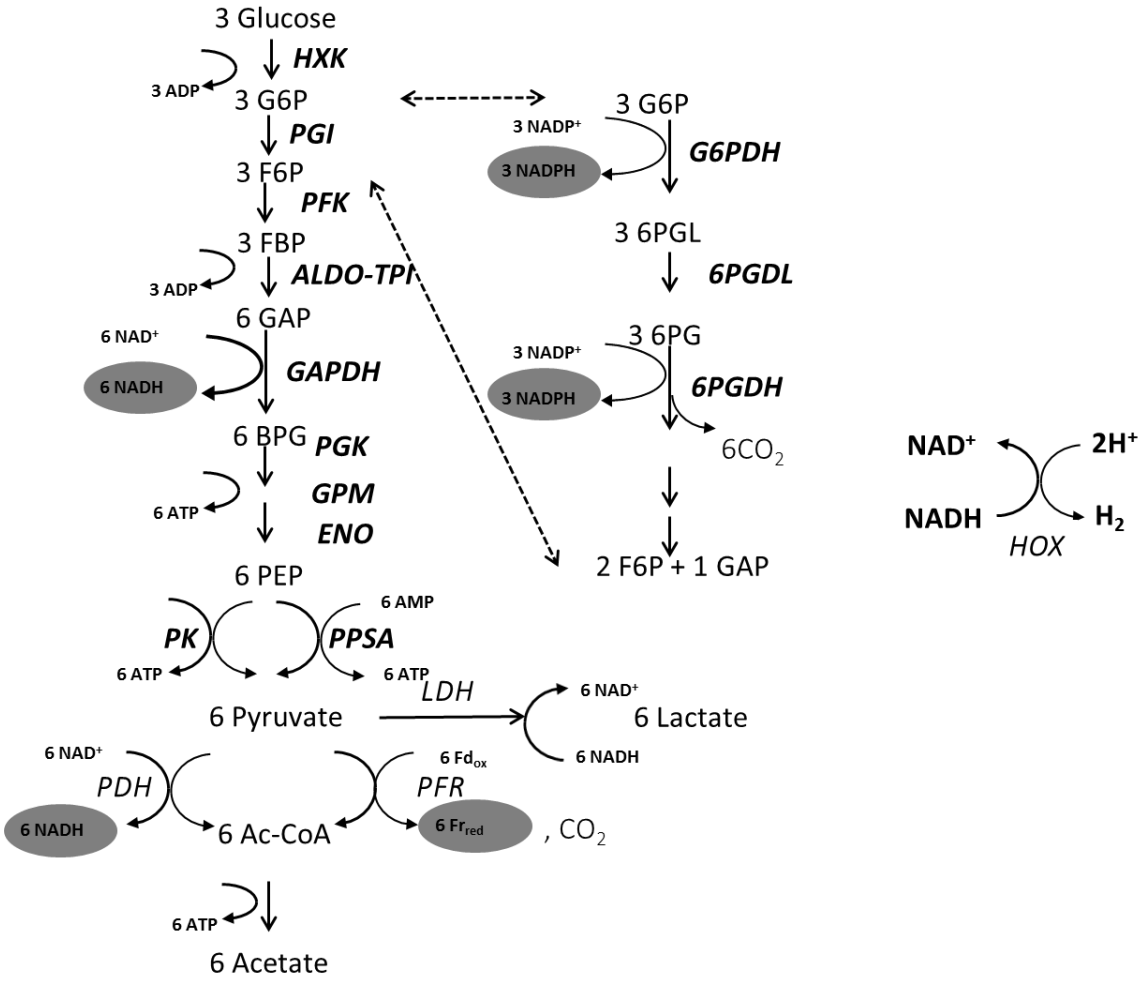

Figure 1-2. **Fermentative metabolic pathways in *Synechococcus* 7002.** Fermentative metabolic pathways in *Synechococcus* 7002 adapted from (McNeely et al., 2010). Abbreviations: OPP, oxidative pentose phosphate pathway; G6P, glucose-6-phosphate; F-6-P, fructose-6-phosphate; FBP, fructose bisphosphate; GAP, glyceraldehyde 3-phosphate; DHAP, dihydroxyacetone phosphate; BPG, bisphosophoglycerate, PEP, phosphoenol pyruvate; PYR, pyruvate; Ac-CoA, acetyl-CoA; HXK, hexokinase; PFK, phosphofructokinase; ALDO-TPI, aldolase-triose phosphate isomerase; GAPDH, glyceraldehyde 3- phosphate dehydrogenase; PGK, phosphpglycerate kinase; GPM, phosphoglycero mutase; ENO, enolase; PPSA, phosphoenol pyruvate synthase; PK, pyruvate kinase; PDH, pyruvate dehydrogenase; PFR, pyruvate ferredoxin oxidoreductase; LDH, lactate dehydrogenase, HOX, hydrogenase.

The OPP pathway generates 6 NADPH and 1 NADH as opposed to the glycolytic pathway which generates only 2 NADH molecules per equivalent of glucose. As OPP pathway produces greater NADPH, redirection of carbon through this pathway has been shown to enhance H_2 production (Kumaraswamy *et al.*, 2013). Pyruvate produced via the above catabolic routes then enters various fermentative processes to replenish the available NAD^+. The major end products of fermentation include acetate, formate, lactate, ethanol together with hydrogen and CO_2 (Gfeller *et al.*, 1984). Of these, lactate, ethanol and H_2 production compete with each other for the reductant generated through catabolism and in turn lower the H_2 productivity. The biggest drawback for H_2 production from cyanobacteria are the fluxes and yield for H_2 production. If improved, H_2 offers a carbon-free, energy intensive molecule that would be the first choice of renewable energy.

5. Scope of the thesis

The scope of this thesis is two-fold: Chapters 2 and 3 are focused towards understanding the cellular distribution of carbon, referred to as carbon partitioning in microalgal cells and provide insights into the metabolic pathways that control the flow of carbon to the respective sink. How a change in carbon partitioning feedback controls photosynthetic electron transport is also addressed. Further, in Chapter 4, I present the results of an iterative metabolic engineering strategy guided by prior knowledge of cyanobacterial fermentative metabolism to increase biohydrogen production. Thus, the overall goal of my research has been understanding and harnessing the potential of algae as biofuel platforms.

The following three manuscripts presented as three separate chapters in the dissertation are:

1) Krishnan, A.; Kumaraswamy, G.K.;Vinyard, D.J.; Gu, H.; Ananyev, G.; Posewitz, M.;Dismukes, G.C. “Metabolic and photosynthetic consequences of a lack of starch biosynthesis in the green alga Chlamydomonas reinhardtii sta6 mutant.” The Plant Journal, 2015, epub DOI: 10.1111/tpj.12783

2) Krishnan, A.; Gu, H.; Kumaraswamy, G.K.; Ananyev, G.M.; Posewitz, M.; Dismukes, G.C. "The carbon decision tree of Chlamydomonas reinhardtii: How starchless strains redirect carbon away from starch." Submitted to *The Journal of Experimental Botany*.

3) Krishnan, A.; Zhang, S.; Liu, T.; Bryant, D.; Dismukes, G.C. "Consequences of *ccmR* deletion on respiration, fermentation and H_2 metabolism in cyanobacterium *Synechococcus sp*. PCC 7002" Submitted to *Biotechnology and Bioengineering*.

An overall summary in Chapter 5 highlights the main conclusions of the work.

Chapter 2 - Metabolic and photosynthetic consequences of blocking starch biosynthesis in the green alga *Chlamydomonas reinhardtii sta6* mutant

Anagha Krishnan[1], G. Kenchappa Kumaraswamy [1], David J. Vinyard[1,2], Huiya Gu[3], Gennady Ananyev[2], Matthew Posewitz[3], G. Charles Dismukes[1,2,]*

[1]Waksman Institute of Microbiology, Rutgers, the State University of New Jersey, Piscataway, NJ 08854, [2]Department of Chemistry & Chemical Biology, Rutgers, the State University of New Jersey, Piscataway, NJ 08854, [3]Department of Chemistry and Geochemistry, Colorado School of Mines, Golden, CO 80401

Summary

The ADP-glucose pyrophosphorylase (AGPase) deletion strain of *Chlamydomonas reinhardtii*, *sta6,* cannot make starch but is known to accumulate lipids under nitrogen-deprived photoautotrophic growth. However, *sta6* has a lower rate of biomass accumulation under nitrogen replete photoautotrophic conditions, which offsets its biotechnological value. To investigate the underlying metabolism under nutrient replete photoautotrophic growth, we have monitored pool sizes of the adenylates, pyridine nucleotides, and central carbon metabolites via LC-tandem-MS and compared fluxes through the photosynthetic electron transport chain and biomass partitioning (total carbohydrates, proteins and lipids). Deletion of starch synthesis in *sta6* accounts for 20% of the biomass loss, while neither protein nor lipid content changed relative to control strains with a functional AGPase. Although the rate of photosynthetic electron transfer (PET; water → CO_2 via PSII + *cytb6f* + PSI) is greatly reduced in *sta6*, the addition of artificial electron acceptors to PSII or PSI completely restored the partial fluxes through each photosystem to control levels, confirming native functionality of both photosystems.

RuBisCO protein levels were normal, while the Calvin-Benson-Basham (CBB) metabolite levels - particularly RuBP - were greatly reduced, indicating diminished substrate for carboxylation in *sta6*. Carbon metabolites in the lower branch of glycolysis accumulated greatly, notably the precursors to fatty acid synthesis (malonyl-CoA, acetyl-CoA) and proteins (glutamate and glutamine), but neither lipid nor protein content changed. Energy imbalance was found to be a key indicator of the metabolic blockage and diminished biomass in the *sta6* starchless mutant, as seen by greatly reduced reoxidation of NADPH and 3-fold larger ATP pool size.

1. Introduction

Microalgal strains partition photosynthetically fixed carbon into terminal products for biosynthesis and storage, including proteins, lipids and starch in amounts that vary appreciably by genus, species and culturing conditions (Becker, 1994); (Subramanian *et al.*, 2013); (Benamotz *et al.*, 1985). Along with growth rate and tolerance to environmental stresses, these traits determine their suitability for biotechnological applications. The search for natural strains that accumulate desired products has been augmented by genetic approaches that aim to create transgenic lines better suited in one or more of these desired traits. For example, in *Chlamydomonas reinhardtii (Chlamydomonas* throughout) (*Chlorophyceae*), genetically blocking alternative competing pathways, including starch biosynthesis increased lipid content by 2-fold to 8-fold relative to control strains in N-deprived media (Radakovits *et al.*, 2010; Work *et al.*, 2010); (Wang *et al.*, 2009); (Li *et al.*, 2010); (Li *et al.*, 2010). The most widely characterized *Chlamydomonas* starchless mutant, *sta6*, contains a deletion in the small subunit of ADP glucose pyrophosphorylase (AGPase) which results in higher lipid production, and has been extensively investigated (Work *et al.*, 2010); (Goodson *et al.*, 2011); (Li *et al.*, 2010); (Li *et al.*, 2010) (Siaut *et al.*, 2011); (Fan *et al.*, 2012); (Wang *et al.*, 2009) (Blaby *et al.*, 2013). Goodson and coworkers observed that following growth of *sta6* the removal of all nitrogen and addition of acetate to the medium led to cells so engorged with lipids that they floated to the surface (Goodson *et al.*, 2011) (Goodenough *et al.*, 2014). However, *sta6* cells have been reported to display diminished photosynthetic activity compared to WT cells under some autotrophic and mixotrophic conditions (Li *et al.*, 2010) (Work *et al.*, 2010). Notably, *sta6* displayed an altered energy partitioning at PSII and a reduced photochemical yield attributed to lower Fv'/Fm' (chlorophyll fluorescence parameter representing the maximum quantum efficiency of PSII photochemistry under continuous illumination) and qP (approximates the proportion of PSII reaction centers that are open under a given light intensity) relative to the reference strains (Li *et al.*, 2010), indicating that the starchless phenotype exhibits consequences

as far upstream as water oxidation by PSII. The reduced levels of water oxidation and CO_2 fixation in *sta6* renders this strain undesirable from an overall bioenergy perspective. To date, identification of metabolic bottlenecks induced by the absence of starch accumulation and the precise mapping of photosynthetic electron transport (PET) chain alterations in *sta6* have not been determined and are explored in this research.

Deletion of AGPase in *sta6* eliminates the conversion of glucose 1-P to ADP-glucose, the activated substrate used in covalent glucose linkage reactions. In the majority of prokaryotes, AGPase is a homotetrameric protein, while in eukaryotes it is a heteromeric enzyme (Ballicora *et al.*, 2004) with separate small and large subunits. However, in both cases AGPase targets glucose for incorporation into carbon and energy storage polysaccharides. In *Arabidopsis*, deletion of the small subunit of AGPase led to a 33% reduction in photosynthetic O_2 evolution, while loss of the large subunit resulted in a moderate decrease of 8% (Sun *et al.*, 1999). Similarly, in cyanobacterial mutants lacking AGPase, photosynthetic O_2 evolution is highly inhibited (Grundel *et al.*, 2012) (Suzuki *et al.*, 2010) indicating the importance of AGPase activity not only in producing starch/glycogen but also maintaining photosynthetic activities by providing photosynthetic ATP and NADPH sinks.

Herein we adopt a highly quantitative metabolomics approach to determine changes in intracellular pool sizes of key metabolites, adenylate energy charge, and pyridine nucleotide redox poise. We combine this approach with measurements of proteins, lipids, carbohydrates, biomass, and photosynthetic electron transport to identify the metabolic and photosynthetic chokepoints in the production of energy carriers and carbon precursors to starch and lipid biosynthesis in *sta6*, and the starch accumulating control strain, *cw15.*

2. Experimental Procedures

2.1) Strains and Culture conditions:

Chlamydomonas strains CC-4349 *cw15* mt^- (Goodenough 330A, henceforth, *cw15*) and *cw15 sta6* (BAFJ5, henceforth, *sta6*) (Wang *et al.*, 2009) (Genty *et al.*, 1989; Zabawinski *et al.*,

2001) were obtained from the *Chlamydomonas* Resource Center (University of Minnesota). *cw15* was chosen as the control strain as it was earlier thought to be the clonal parent to *sta6*. During the writing of the manuscript, Blaby and co-workers (Blaby *et al.*, 2013) showed that it is not the original parent, as they do not share the same mating type. However, *cw15* was kept as the control strain in this study because it a) has an intact starch biosynthetic pathway (Blaby *et al.*, 2013), b) analogous to *sta6* lacks a cell wall, and c) does not require arginine for growth, making it suitable for autotrophic photosynthetic studies. Liquid cultures were grown in phosphate buffered, Sueoka's high salt medium (HS) supplemented with 5mM $NaHCO_3$ and 9.4 mM NH_4Cl (Harris *et al.*, 2009). The cultures were maintained on an orbital shaker (100 rpm) under continuous illumination (100 μE m^{-2} s^{-1} PAR) at 25ºC. For growth rate measurements, flasks were inoculated at a density of ~$6x10^5$ cells mL^{-1} and cell density was measured daily using a Neubauer counting chamber. Growth data was fitted to a Gompertz function (Zwietering *et al.*, 1990) to calculate the specific growth rate and doubling time. For all other characterizations, cells were grown in semi-continuous cultures at a density of 8.8-11 x 10^6 cells mL^{-1}. For biomass measurements, precultures were grown to ~15-20 x 10^6 cells mL^{-1} then resuspended at 2.5 × 10^6 cells/ml in fresh HS medium. Samples were taken immediately after resuspension (0h) and at 96 h.

2.2) Chlorophyll measurements:

Chlorophyll concentration was determined spectrophotometrically by methanol extraction using extinction coefficients from Porra (Porra *et al.*, 1989).

2.3) In vivo measurements of oxygen evolution:

Light saturated OER were measured using a membrane covered Clark O_2 (*Hansatech*) electrode at 25ºC in HS media containing 5 mM $NaHCO_3$. Samples were illuminated with red light. Light dependent respiration (LDR) was measured within 30 s post darkness and subtracted from the light dependent OER to get the gross OER. Appropriate electron acceptors and inhibitors were added directly to the sample chamber. Titration curves for PSII and PSI electron acceptors, 2, 5-dichloro-

p-benzoquinone (DCBQ) and N-dimethyl-4-nitrosoaniline (PNDA) are shown in Fig. 2-1. LDR was not subtracted while reporting data using artificial electron acceptors.

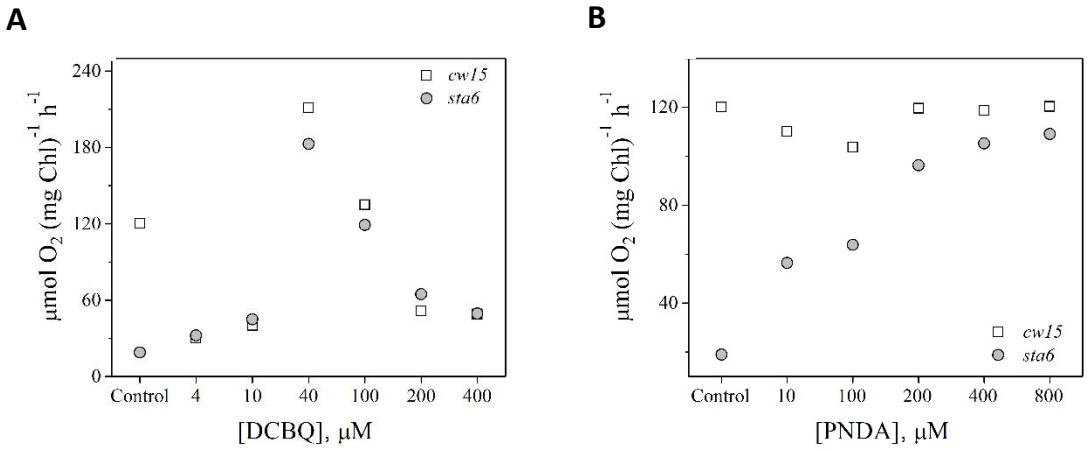

Figure 2-1 Titration of light saturated O_2 evolution rate to determine the optimal electron acceptor concentration for: A) DCBQ and B) PNDA.

2.4) Relative electron transport rate and non-photochemical measurements:

Electron transport rates and NPQ were measured on a pulse-amplitude modulated (PAM) fluorometer (model *FL-3000*; *Photon Systems Instruments)* (Schreiber *et al.*, 1997). Cultures were diluted to 2.5 µg Chl mL^{-1} in HS media containing 5mM $NaHCO_3$ and incubated in the dark for 15 min before each experiment. Samples were illuminated for 10 minutes before saturating pulse was applied. Electron transport rates and NPQ were calculated using, ETR = PAR x 0.5 x 0.84 x Φ_{PSII}, where Φ_{PSII} is equal to $(F_m'-F_t')/F_m'$ and NPQ = (F_m/F_m') - 1 (Genty *et al.*, 1989).

2.5) Fast Repetition Rate (FRR) Fluorometry measurements:

Chlorophyll-a variable fluorescence yields were measured using a home-built laser fast repetition rate (FRR) fluorometer (Ananyev *et al.*, 2005). Whole cells were concentrated to 50 µg mL^{-1} chlorophyll, dark adapted for 120 s, then subjected to a train of 50 single turnover laser flashes (STF) (665nm, 32,000 µE m^{-2} s^{-1}) at either 4Hz (Low STF frequency) or 100Hz (High STF frequency). To maximize the signal to noise ratio, the pulse train was repeated 75 times with 120 s of dark incubation between consecutive experiments. Variable fluorescence yield was calculated using $F_v=(F_m-F_o)/F_m$ (Maxwell *et al.*, 2000).

2.6) Time resolved O_2 evolution:

Time-resolved OER were measured using a home-built bare-Pt electrode controlled by Labview software (Zakrzhevskii *et al.*, 1978) which allows kinetic resolution of the transit time to electron acceptor pools downstream of PSII (PQ, $NADP^+$, CO_2). Cells were concentrated to 20 µg ml^{-1} chlorophyll, 8 microliters were loaded onto the 8 mm diameter electrode, dark incubated for 15 min, and illuminated with red light (400 µE m^{-2} s^{-1}). The full kinetics of O_2 evolution was recorded over 2 min. O_2 signals thus generated reflect the size of the electron acceptor pools and transit times to fill them (Zakrzhevskii *et al.*, 1978). O_2 peak associated with the reduction of the PQ pool was isolated by subtracting the slower filling pools by linear extrapolation to the baseline and the total O_2 evolved was determined from the current using Faraday's law of electrolysis.

2.7) Pyridine nucleotide fluorescence kinetics:

NAD(P)H fluorescence induction kinetics were measured in whole cells with a home-built setup similar to an instrument described previously (Mi *et al.*, 2000). A UV-LED (365 nm wavelength) in combination with an optical filter (2 mm UG 11, Schott) was used as the excitation light source for NAD(P)H modulated at 100kHz. Bright red LED (660 nm, Hewlett-Packard) was used as actinic light. For fluorescence emission detection, we used a low noise photomultiplier (R2059, *Hamamatsu, Japan*) with a maximum sensitivity at 420 nm protected by a combination of a long-pass filter (KV418, *Schott*), a short-pass filter (DT Cyan), and a blue-green glass filter (BG39, *Schott)* to eliminate both the UV-measuring light and chlorophyll fluorescence. An NMR tube with an outer diameter of 5 mm was used as the sample holder and the detection and excitation pathways were perpendicular. A multifunctional DAC board PCI-6036E (*National Instruments*) was used for data acquisition.

2.8) Metabolite extraction and analysis

Cultures (8.8-11 x 10^6 cells mL^{-1}) were quenched in 60:40 MeOH/water mixture and centrifuged at 5000 rpm for 2 min at 0^{o}C. The supernatant was discarded and the pellet was resuspended in ice-cold 60:40 methanol:water mixture. The suspension was sonicated for one min then incubated at -20^{o}C for 20 min. Further, the samples were centrifuged for 5 min at 5000 rpm at 0^{o}C. The supernatant was vacuum dried (Centri Vap Benchtop Vacuum Concentrator, *Labconoco*) and the resulting pellet was resuspended in LC-MS grade water. Samples were injected into an *Agilent* 6490 QQQmass analyzer coupled to HPLC (*Agilent Technologies*) for metabolite analysis (Kenchappa *et al.*, 2013). Concentrations of each metabolite per cell were calculated using the calibration curve. Fold changes were calculated as a ratio of concentration of metabolites in low light and high light conditions, respectively.

2.9) Lipid, glucose and protein analysis

Total lipids were converted to fatty acids for GC-FID analysis as described previously (Radakovits *et al.*, 2012) and analyzed using an Agilent 7890A gas chromatograph and DB5ms column with flame ionization detection. Total sugar was analyzed using the anthrone assay (Morris, 1948) (Meuser *et al.*, 2012). Protein levels were determined using the DC protein assay kit (Bio-Rad) according to the manufacturer's instructions.

3. Results

3.1) Photoautotrophic growth and biomass accumulation

Fig. 2-2 A compares sta6 and cw15 growth rates in photoautotrophic HS medium supplemented with 5 mM NaHCO3 , illuminated using 100 µE m-2s-1 (white light). The *sta6* mutant grew slower relative to cw15, with 30% longer doubling time (p= 0.03). Both strains reached stationary phase simultaneously, but sta6 had a ~1/3 lower cell density relative to the control strain. As the cultures grew, the light penetration decreased because of self-shading with transmitted intensity dropping as low as 25 µE m-2s-1 in stationary phase cultures.

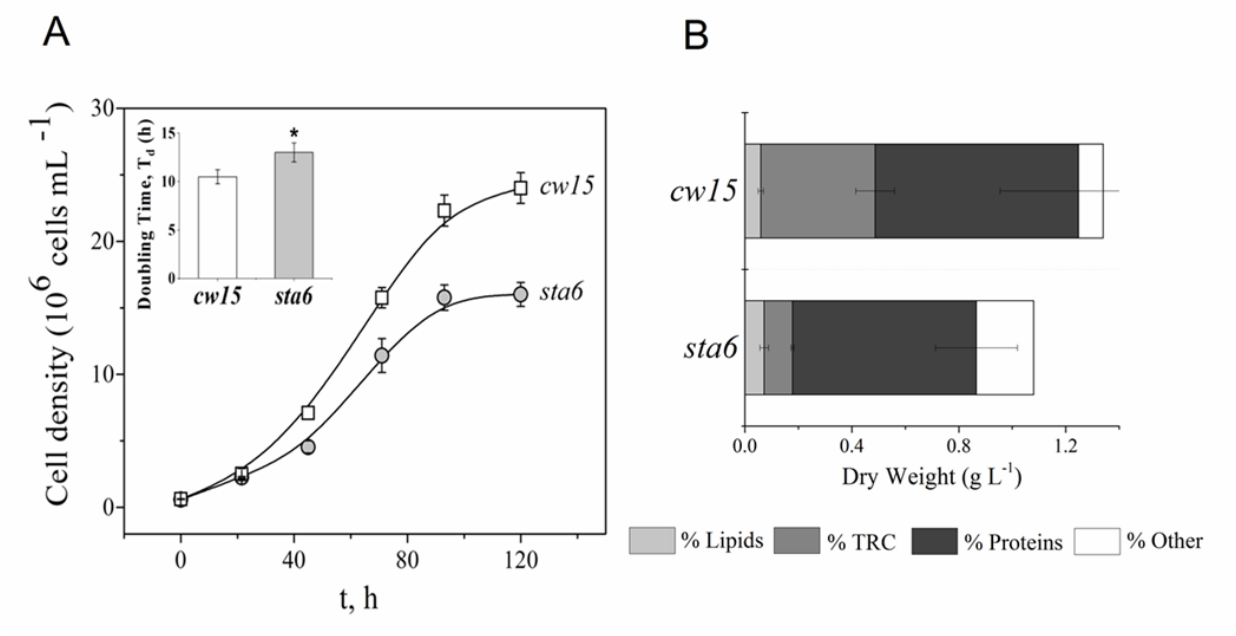

Figure 2-2 **Photoautotrophic growth phenotypes for *cw15* and *sta6*.** Growth rates measured under photoautotrophic conditions. The inset shows the doubling time based on fits to Gompertz curves. The asterisk indicates a statistically significant difference compared with *cw15* ($P<0.05$). B) Biomass composition of cw15 and sta6 under N-replete photoautotrophic conditions measured after 4 days of growth. The y axis represents the dry weight in grams. Values are means and standard errors of three biological replicates.

At stationary phase (after 96 h of growth), the three major biochemical fractions (total reducing carbohydrate, lipids and proteins) were quantified in *sta6* and *cw15* (Fig. 2-2 B and Table 2-1). In addition, we also measured the biomass distribution in two other starch synthesizing reference strains, CC124 and D66 to assess biomass distribution across multiple control strains. The dry cell weights (DCWs) of the *sta6* mutant cultures were ~20-35% lower than the DCWs of all the three reference strains. Total reducing carbohydrate (TRC) content in *sta6* was between 2-5 times lower than the control strains. Additionally, *sta6* has slightly increased protein content relative to D66 and CC124, however, it is not statistically different when compared to *cw15*.

Biomass (HS medium)	*sta6*	*cw15*	CC124	D66
DW (0hr)	0.13 ± 0.04	0.07 ± 0.00	0.18 ± 0.03	0.12 ± 0.04
DW (96hr)	1.08 ± 0.05	1.34 ± 0.13	1.29 ± 0.11	1.49 ± 0.06
DW Flux ($gl^{-1}d^{-1}$)	0.23 ± 0.02	0.32 ± 0.02	0.27 ± 0.02	0.34 ± 0.03
Lipid (96hr)	0.072 ± 0.016	0.059 ± 0.010	0.106 ± 0.008	0.109 ± 0.023
%Lipid	6.6 ± 1.2	4.4 ± 0.3	8.3 ± 1.2	7.3 ± 1.5
Total reducing Carbohydrate (TRC) (96hr)	0.106 ± 0.006	0.428 ± 0.072	0.246 ± 0.029	0.493 ± 0.142
%TRC	9.88 ± 0.14	31.8 ± 2.4	19.1 ± 1.2	33.0 ± 8.8
Protein (96hr)	0.688 ± 0.153	0.761 ± 0.293	0.645 ± 0.109	0.702 ± 0.083
%Protein	62.4 ± 18.0	56.1 ± 16.5	49.9 ± 7.2	47.5 ± 7.3
Mass balance	80.5 ± 16.3	92.2 ± 19.2	77.2 ± 8.7	87.8 ± 6.0

Table 2-1 Biomass composition of *sta6* and three reference strains, *cw15*, CC124 and D66, under NH_4Cl replete, photoautotrophic culturing conditions. Values are reported as g L-1 and data represent three independent biological replicates.

These results indicate that the loss of starch biosynthesis, does not result in the repartitioning of carbon from TRC to lipids and proteins under nutrient replete conditions; instead cellular biomass is reduced by an amount that is similar to the attenuated TRC levels in *sta6* relative to the control strains. Diminished biomass accumulation implies that a primary adaptation in this starchless mutant is diminished/altered photosynthetic electron transport.

3.2) Photosynthetic oxygen evolution rate, PSII quantum yield of charge separation and electron transport rate

To quantify the effect of a lack of starch biosynthesis on photosynthesis; photosynthetic O_2 evolution rates (OER) were measured for *sta6* and *cw15* with a Clark electrode and illuminated with a range of light intensities (λ_{max} = 620 nm). At light levels up to 60 µE $m^{-2}s^{-1}$, *sta6* and *cw15* have comparable OER but as the light intensity increased above this threshold, the differences between *cw15* and *sta6* increased and at a light intensity of 680 µE $m^{-2}s^{-1}$, *sta6* shows a 3.5-fold lower OER than *cw15* (Fig. 2-3A). It important to note that cultures were grown using 60-80 µE $m^{-2}s^{-1}$ of white light, and then OER assayed across a range of light intensities. The lower OER in *sta6* (Fig. 2-3A), indicates that either PSII itself is impaired and/or that reactions downstream of PSII are affected at light intensities >60 µE $m^{-2}s^{-1}$. To differentiate between the two processes we probed both the light-induced electron transport rate (ETR) through PSII and the quantum yield of PSII charge separation and the turnover efficiency of the water-oxidizing complex (WOC).

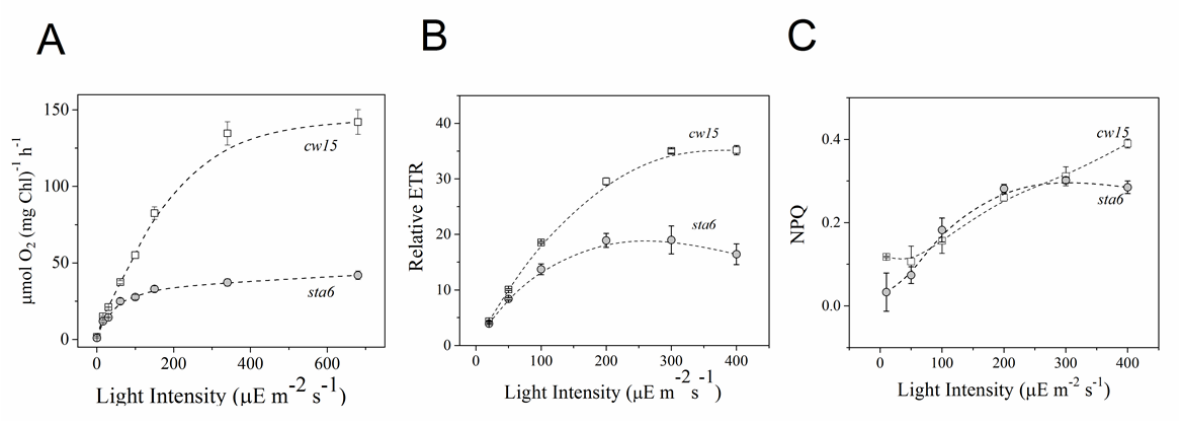

Figure 2-3 **Oxygen, electron transport rate and NPQ**. A) Oxygen evolution rates at different light intensities (16, 30, 61, 100, 150, 340 and 680 μE m^{-2} s^{-1}) measured (at t = 6 T_d Figure 2-2 A), and B) Relative electron transport rate (ETR) and C) NPQ measured by PAM fluorometer as a function of increasing actinic light intensities. Data represent the mean of three biological replicates with standard error.

Light-induced electron transport rate (ETR) through PSII was measured using a pulse amplitude modulated (PAM) fluorometer (Schreiber *et al.*, 1997) (Fig. 2-3 B). This method reports on the fraction of open PSII centers capable of photoreducing Q_A as a function of the light intensity of concurrent background illumination. Although widely used to measure ETR (flux), this signal is a static measure of Q_A population. It is proportional to the sum of ETR flux and photochemical quenching that does not lead to electron transfer beyond PSII. For this reason, the PAM type measurement of ETR includes non-flux contributions to photochemical quenching within PSII that produce no O_2. The ETR curves show a trend qualitatively similar to OER, with *sta6* and *cw15* showing no significant differences at the lowest light intensities, but with differences between *sta6* and *cw15* emerging at ~75 µE $m^{-2}s^{-1}$. *sta6* shows substantially lower ETRs at light intensities above 200 µE $m^{-2}s^{-1}$. At the maximum light intensity used for the measurement (~ 400 µE $m^{-2}s^{-1}$) ETR in *sta6* is ~2-fold lower than *cw15*. ETR in *sta6* also saturates at a lower light intensity (200 µE $m^{-2}s^{-1}$). The % differences observed in OER are larger than the differences in ETR (Fig. 2-4) above light intensities of 100 µE $m^{-2}s^{-1}$. This may be attributed to alternate oxygen consuming pathways (also see section 2.3). To investigate the possibility of non-photochemical quenching (NPQ)-dependent decrease in ETR, NPQ was quantified simultaneously with ETR using (Schreiber *et al.*, 1997) and calculated as given in "Experimental Procedures". *sta6* and *cw15* do not show significant differences in NPQ (Fig. 2-3 C), thus the difference in ETR are not due to differences in excitation quenching in the antenna.

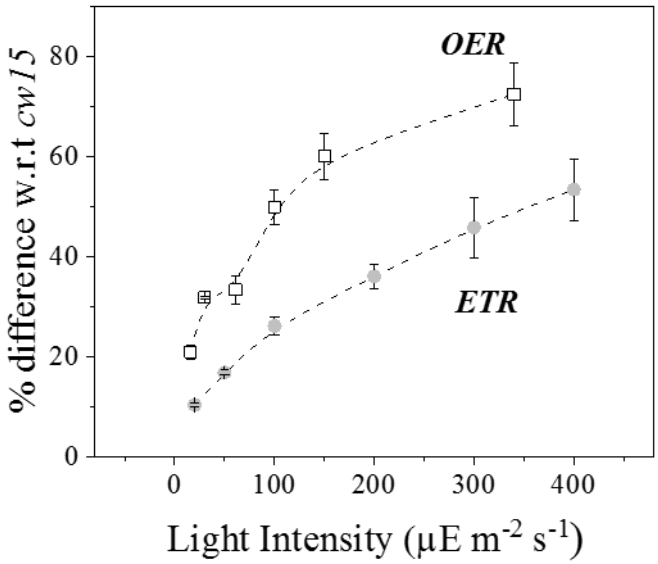

Figure 2-4 **Discrepancy between OER and ETR.** % difference between OER and ETR between *cw15* and sta6 calculated as (*cw15*-*sta6*)/(*cw15*) × 100 at light intensities between 16-400 µE m^{-2} s^{-1}.

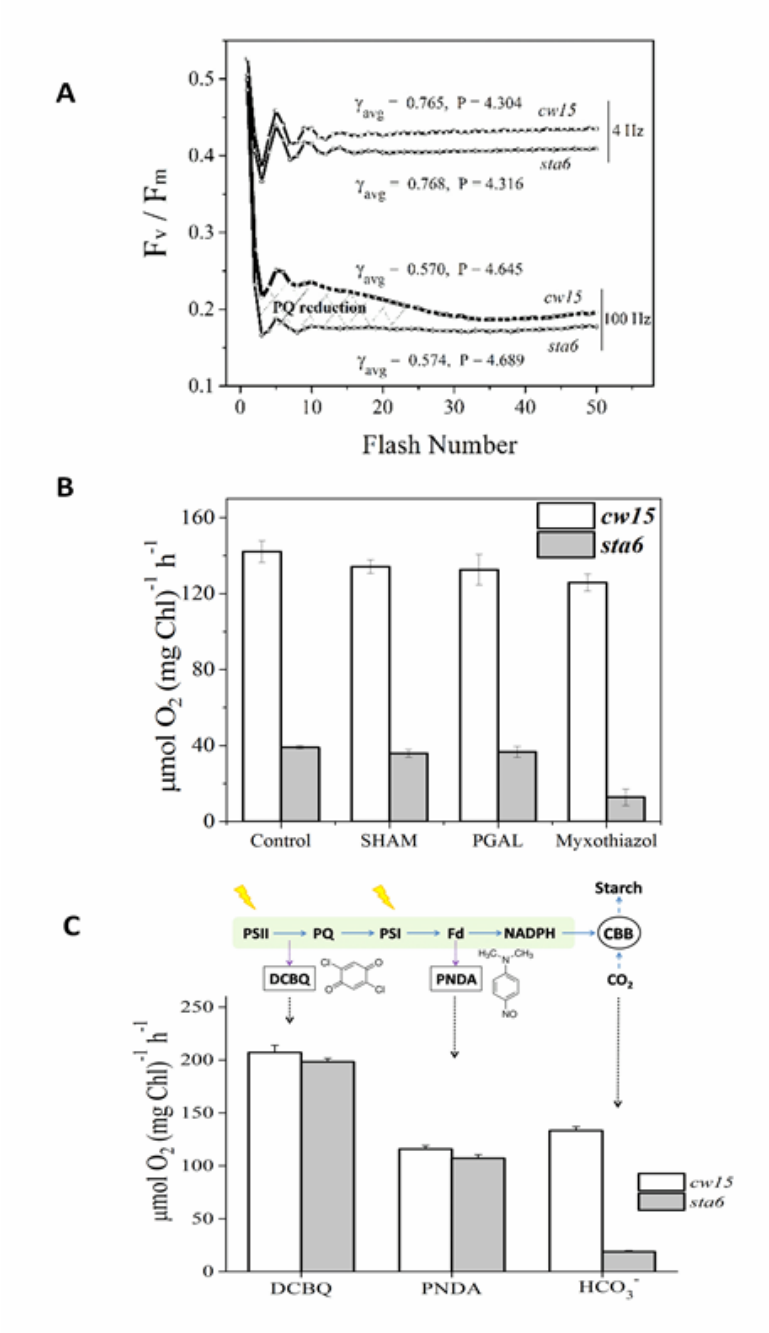

Figure 2-5 ***sta6* is limited by electron acceptor.** A) Average chl variable fluorescence yield (Fv/Fm) from PSII produced by 50 single turnover pulses at two flash rates, 4 Hz and 100 Hz. The average Kok hit parameter, γ_{avg}, was determined by fitting the data to the VZAD model. γ_{avg} = 1- α(miss) - β(double hit) - δ(backward) - ε(inactivated). Cycle period, P, was determined by Fourier transformation. The shaded region represents the reduced PQ pool. B) OER of *cw15* and *sta6* in the presence of inhibitors to alternate electron flow pathway. Control has 5 mM bicarbonate, SHAM (20 μM) inhibits AOX, PGAL (2 mM) inhibits PTOX, Myxothiazol (2 μM) inhibits respiration. C) Light saturated O_2-evolution rates in the presence of artificial electron acceptors (40 μM DCBQ or 400 μM PNDA or 5mM $NaHCO_3$) Data represent the mean of three biological replicates with standard error.

To examine if an impaired PSII-WOC activity is the cause of the low OER and ETR phenotype, the quantum yield of PSII charge separation and flux through the WOC were measured using Chl variable fluorescence emission (Fv/Fm) with a fast repetition rate fluorometer (FRRF) at two flash frequencies (Ananyev *et al.*, 2005). Compared to *cw15, sta6* exhibits slightly lower steady-state dark-adapted (F_v/F_m) under both low (4 Hz, $\langle F_v/F_m \rangle \approx$ 0.43-0.41) and high (100 Hz, $\langle F_v/F_m \rangle \approx$ 0.24 -0.18) flash frequencies (Fig.2-5 A). Following an initial dark adaptation, the rate of damping of the period-four oscillations in F_v/F_m was similar for both strains and decreased at higher flash rates (Fig. 2-5 A), indicating both strains have normal initial WOC functioning. Fits of the oscillations to an advanced Kok model (VZAD algorithm) (Vinyard *et al.*, 2013) produce almost identical hit parameter (γ_{avg}) and period (P) at both flash frequencies, indicating no significant difference in the initial turnover probability of the WOC in the two strains. However, the initial rate of damping of individual oscillations in F_v/F_m drops off rapidly with higher flash rate (γ_{avg} dropping to 0.57 at 100 Hz, Fig. 2-5 A) and the non-oscillating portion of Fv/Fm in *sta6* is missing the portion attributed to filling of the PQ pool (hatched area in Fig. 2-5 A) (Kolling *et al*., 2009). Thus, *sta6* is characterized by a slower rate of emptying the reduced plastoquinol PQH_2 pool relative to *cw15*.

Thus, both strains have a normal functioning WOC and PSII charge separation, but *sta6* has an inhibited PQH_2 oxidation rate, reflecting a blockage in electron flow downstream of the PQH_2 pool. This blockage is responsible for the sharp break in OER flux above light intensity > 100 μE $m^{-2}s^{-1}$ (Fig. 2-3A).

3.3) Alternative oxygen consuming pathways

As previously mentioned, at higher light intensities there is an imbalance in the extent of inhibition reported by OER vs. ETR, with OER predicting a lower intensity threshold and larger activity gap at saturation between *sta6* and *cw15* (Fig. 2-4). This difference indicates the presence of alternative O_2 consuming pathways that influence OER and ETR differently at light intensities above 100 μE

$m^{-2}s^{-1}$. The main pathways that consume O_2 are respiration and alternative oxidases (AOX) in the mitochondrion, and plastoquinol terminal oxidase (PTOX), Mehler reaction and photorespiration in the chloroplast. Inhibition of AOX and PTOX (also known as chlororespiration) by specific inhibitors propyl gallate (PGAL, 2mM) and salicylhydroxamic acid (SHAM, 20µM) did not have any significant effect on the OER (at 680 µE $m^{-2}s^{-1}$) in both *cw15* and *sta6* (Fig. 2-5 B). However, inhibition of mitochondrial respiration by myxothiazol (inhibiting the cytochrome bc1 complex of the respiratory chain) leads to a 70% loss of OER in *sta6,* while only minor loss (10%) in *cw15* (Fig. 2-5B) (at 680 µE $m^{-2}s^{-1}$).Thus, only in *sta6* does mitochondrial respiration act as an important shunt to partially consume the excess light-induced reductant generated in the chloroplast. Further measurements of Mehler reaction and photorespiration were not performed, though Fig. 2-4 clearly indicates their possible contributions to reductant consumption.

3.4) Normal PET rates through PSII and PSI can be restored in sta6.

The foregoing results suggest that under high light intensities, photosynthesis in *sta6* is limited by the reactions occurring downstream of PSII, either within the electron transport chain itself (light dependent reactions) or by the carbon fixation reactions (light independent reactions). To distinguish between these options, artificial electron acceptors were used to alleviate choke points in the PET chain and the corresponding OER was measured at 680 µE $m^{-2}s^{-1}$. As shown in Fig. 2-5 C, in the presence of 2, 5-dichloro-p-benzoquinone (DCBQ) (40 µM), which accepts electrons from the Q_B site of PSII, the OER of both *sta6* and *cw15* increased to an approximately equal level of ~200 µmol O_2 mg Chl^{-1} hr^{-1}. With N-dimethyl-4-nitrosoaniline (PNDA) (400 µM), which accepts electrons from PSI via ferredoxin (FDX), both strains had an equal OER of ~110 µmol O_2 mg Chl^{-1} hr^{-1}. This experiment reveals that *sta6* has a structurally intact electron transport chain similar to *cw15* through FDX, with normal fluxes and similar electron acceptor pool sizes (for PQ and Fdx). Bicarbonate addition to ensure saturating levels for carbon fixation reactions (Fig. 2-5 C), did not

reverse the disparity in OER between *cw15* and *sta6*. Thus, the OER in *sta6* is limited downstream of FDX by carbon fixation reactions.

To isolate the location of flux chokepoints, we measured the light induced yield of O_2 from a thin solution of cells (0.8 mm) using a bare platinum (rate) electrode illuminated at 400 µE $m^{-2}s^{-1}$. This method resolves kinetic features of the electron acceptor pools downstream of PSII (Zakrzhevskii *et al.*, 1978). A typical O_2 evolution trace after dark adaptation displays three distinct time-resolved features. The first is a sharp transient peak from reduction of the PQ pool, the second is a broad peak arising from the reduction of $NADP^+$, the third is a continuous slope from CO_2-dependent O_2 evolution. The initial peak has a rise time of 300 ms due to O_2 diffusion to the electrode and is determined by the finite thickness of the sample. The area under this peak (see experimental procedure) is directly proportional to the difference in electron fluxes filling and emptying the oxidized PQ pool. The PQ peak intensity and area are indistinguishable for *sta6* and *cw15*. In *cw15* a second O_2 feature appears as an inflection (Fig. 2-6 top), but is masked by a much larger continuous slope that disappears when CO_2 is removed (not shown) or when the PET inhibitor 3-(3,4-dichlorophenyl)-1,1-dimethylurea (DCMU) is added (Fig. 2-6 bottom). This CO_2-dependent water oxidation rate is 7-fold greater in *cw15* than in *sta6* over the indicated illumination period (400 µE $m^{-2}s^{-1}$).

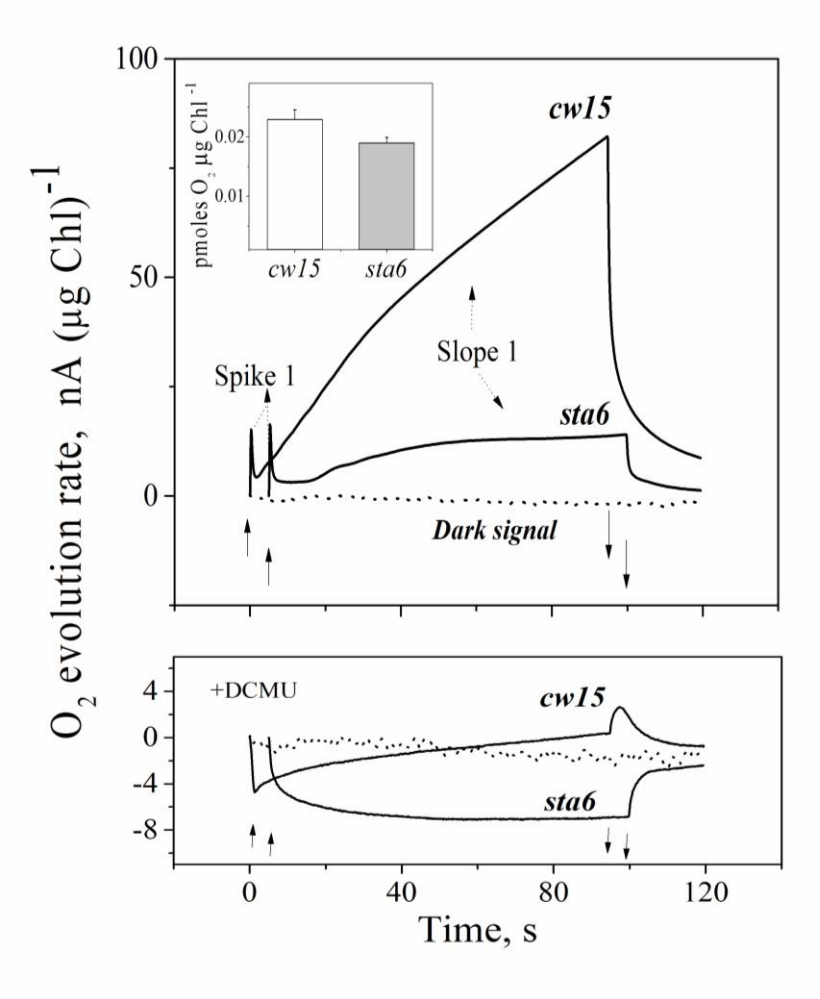

Figure 2-6 **Time resolved oxygen evolution rate.** Light saturated OER on a bare-Pt electrode recorded as nanoAmperes $(\mu g\ Chl)^{-1}$ in the presence of bicarbonate as the sole electron acceptor. Data represent the average of three biological replicates. Light was turned on or off at points indicated by solid arrows. Transient O_2 evolution shows two distinct phases, spike 1 representing the PQ pool reduction while the continuous slope representing carbon fixation (top panel). The inset shows the PQ pool size equivalent calculated as indicated in experimental procedures. Bottom panel shows the effect of 10 µM DCMU on the OER. Dotted line represents the dark current recorded on the electrode in the absence of illumination.

To quantify the transient flux into and out of the NADP(H) pool the relative light-induced yield of the reaction: PSI donor $\rightarrow NADP^+$ was monitored by the fluorescence change from reduced NAD(P)H *in vivo*. NAD(P)H kinetics in whole cells was measured using a home-built fluorometer (excitation at 365 nm, detection at 420 nm) similar to (Mi *et al.*, 2000). Samples were exposed to a dark-light-dark regime of 5-4-7 min using saturating light (400 µE $m^{-2}s^{-1}$, 660 nm). An average curve from three biological replicates for *sta6* and two for *cw15* is shown in Fig. 2-7 A. The rise and decay times and the amplitude changes of the fluorescence yield are given in Table 2-2. Light induced changes in NAD(P)H fluorescence display dynamics similar to previous reports (Cerovic *et al.*, 1993; Mi *et al.*, 2000). We observe a rise in NADPH fluorescence emission during actinic illumination, signifying light-driven reduction of $NADP^+$, followed by a steady-state phase where the $NADP^+$ reduction and NAD(P)H oxidation rates are matched. Post illumination, in darkness the fluorescence decays followed by recovery to the initial steady-state dark level. In the presence of the artificial PSI electron acceptor PNDA, both *sta6* and *cw15* produce no change in NAD(P)H fluorescence upon illumination.

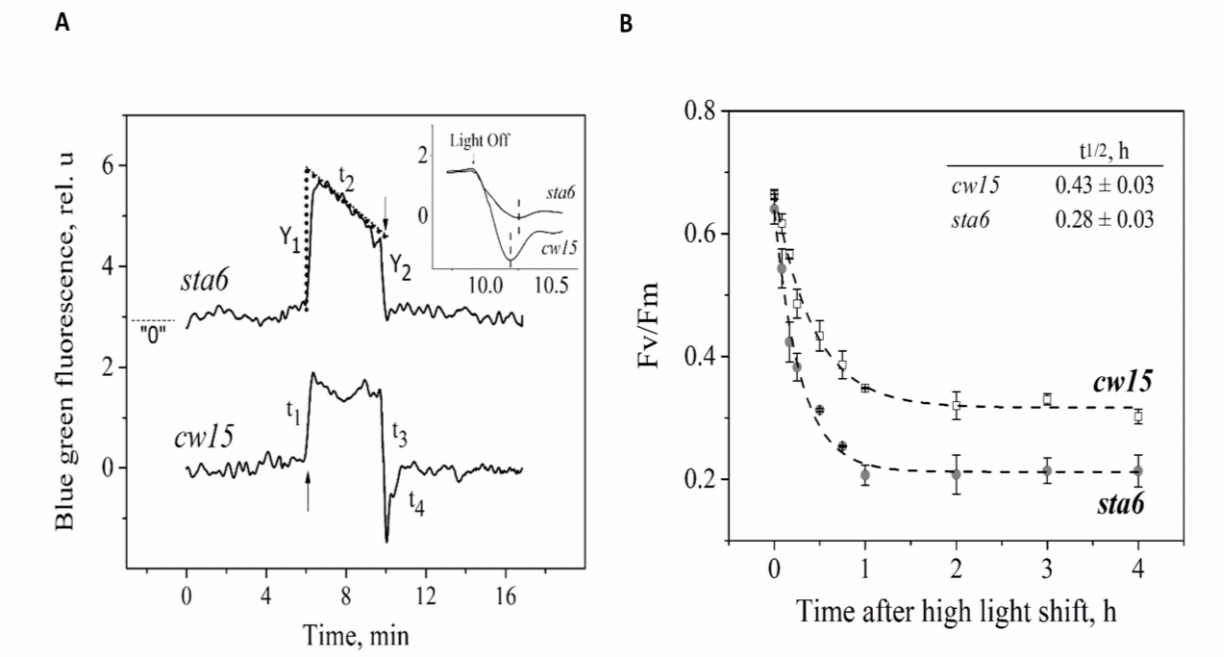

Figure 2-7 **NADPH fluorescence and photoinhibition**. A) Effect of actinic illumination on induction of continuous level of blue-green fluorescence arising from NAD(P)H. Actinic illumination was provided by saturating red light (660 nm, Intensity =400 µE m^{-2} s^{-1}). *sta6* has been offset by 3 units in both the figures. Fluorescence decay during illumination (lifetime denoted by t_2 in *sta6*) was fitted to a linear decay slope and extrapolated to "light on" time to calculate the maximal photoreduced NADPH (Y1) in the absence of oxidation of NADPH. Y2 denotes the oxidized NADPH post illumination. t_1, t_2, t_3, t_4 are the rise and decay times as described in the text. Magnification of the decay kinetic is given in the inset. For both A and B, light was turned on or off at points indicated by solid arrows B) Photoinhibition at 400 µE m^{-2} s^{-1}. $t_{1/2}$ for photoinhibition is given in the inset table. Data represent the mean of three biological replicates with standard error.

	cw15	***sta6***	**Fold Change (*sta6*/*cw15*)**
Rise time, t_1 (s)	7.2 (0.3)	7.2 (0.42)	1.0 (0.07)
Reoxidation time, t_2 (min)	$\leq t_1$	2.9 (0.67)	
Decay time, t_3 (s)	14 (0.6)	20 (2.4)	1.4 (0.12)
Re-reduction rate, t_4 (s)	39 (0.6)	-	
Maximum photoreduced NADPH , Y_1 (rel. u.)	1.5 (0.04)	2.6 (0.3)	1.7 (0.12)
Oxidized NADPH post illumination, Y_2 (rel. u)	2.8 (0.3)	1.9 (0.2)	0.68 (0.15)

Table 2-2 **Kinetics of NADP+ reduction and NADPH reoxidation.** Values represent the average of three biological replicates and standard error of mean is given in parentheses. The NAD(P)H fluorescence yield rises from the dark adapted level to the maximal photoreduced level in identical times for both strains (t_1= 7.2 sec). During the illumination period the larger photoinduced amplitude in *sta6* decays slowly to 50% with a lifetime of ~2.9 minutes (t_2), while the lower photoinduced amplitude for *cw15* does not decay appreciably on the measurement timescale. The larger amplitude and gradual decaying slope of light-induced NADPH in *sta6* is attributed to slower NADPH reoxidation. This was verified by turning off the actinic light and monitoring the decay rate of the NADPH fluorescence amplitude (Y_2), which is indeed slower in *sta6* (t_3 = 20 sec) than *cw15* (t_3 = 14 sec) and "overshoots" to a level lower than the initial dark steady-state. The t_3 decay rate in *cw15* is followed by recovery to the initial steady-state level within 39 sec (t_4) as the non-equilibrium level of oxidized $NADP^+$ is (re)reduced in the dark. Such oscillating behavior is commonly associated with regenerative cycles. This latter phase is absent in *sta6*. Taken together, the lack of overshoot, slower t_3 decay, and slow decay of the actinic phase (t_2) all support the conclusion of a slower reoxidation rate of actinically generated NADPH in *sta6*. For *cw15*, the lack of observable decay of the actinically generated NADPH phase indicates a rate of NADPH reoxidation faster than the time resolution of the instrument (~1 sec).

3.5) sta6 is more sensitive to photoinhibition

Sensitivity to photoinhibition upon prolonged high light exposure was determined by measuring the loss of PSII quantum yield (as Fv/Fm) in samples incubated under light (400 μE m^{-2} s^{-1}, 620 nm) over a period of 6 h (Fig. 2-7 B). *sta6* exhibits a 35% faster photoinhibition rate (halftime = 0.28 h vs. 0.43 h) than in *cw15*, indicating the importance of starch biosynthesis for tolerance to high light stress.

3.6) sta6 is inefficient in draining upper glycolytic intermediates at high light intensity

Given that OER and ETR are significantly inhibited at high light intensities and the metabolic block occurs downstream of the PET, comparative metabolic analysis of low (LL) and high light (HL) treated samples was performed to reveal the metabolic consequences of the decrease in NADPH reoxidation. The pool sizes of the various metabolites involved in the central carbon metabolism were measured using LC-MS/MS (Bennette *et al.*, 2011) under ambient growing conditions (~60-80 μE $m^{-2}s^{-1}$, low light) and after a 2 h exposure to high light (400 μE $m^{-2}s^{-1}$). Concentrations of the metabolites are presented in Table 2-3. Metabolites pertaining to the CBB cycle and upper glycolysis are summarized graphically in Fig. 2-8 A and 2-8 B. Simultaneously, the biomass contents (lipids, TRC and protein) were also measured (Fig. 2-8 C) using the same cultures.

Upon transfer to HL, neither protein nor lipids showed a significant change in the two strains. However, the TRC content per cell increased by 25% in *cw15* while being unchanged in *sta6* (Fig. 2-8 C). Thus, under 2 h exposure to HL, fixed carbon predominantly assimilates as starch, while blocking starch biosynthesis at AGPase in *sta6*, carbon assimilation into all biopolymers is impeded.

Metabolite analysis revealed that under HL, *cw15* shows an increase in the CBB cycle intermediates including RuBP (5-fold), R5P (4-fold) and X5P (9-fold) compared to LL. GAP and 3PG levels also increase by about 2-fold (Fig 2-8 A, Table 2-3). This increase correlates with the enhanced carbon

assimilation in the *cw15* (Fig. 2-8 C). Even though the TRC content increases in *cw15* (Fig. 2-8 C), there is no increase in the pool size of the upper glycolytic intermediates indicating an efficient drain of the upper glycolytic metabolites into carbohydrate biosynthesis. By contrast in *sta6*, we observe large increases in levels of many CBB cycle metabolites, especially GAP and 3PG levels increase by 11-fold and 7-fold respectively. Additionally, we observe enhanced levels of the upper glycolytic intermediates G1P, G6P and F6P by 5-fold, 4-fold and 8-fold respectively, even though there is no significant increase in the TRC content. Thus, under high light conditions and in the absence of AGPase, there is an inefficient drain of upper glycolytic intermediates that normally flow into starch biosynthesis.

A lower ATP recycling rate can limit electron transport chain flux (Sharkey *et al.*, 1986) . To test this, the adenine nucleotide concentrations were quantified using LC-MS and the cellular energy charge (CEC) was calculated (Table 2-3). *sta6* exhibits appreciably larger concentrations of all adenine nucleotides (ATP, ADP and AMP) between 1.5- 2.8 fold (ATP) higher in *sta6* relative to *cw15* under both LL and HL. Additionally, *sta6* has a marginally larger pool size of the phosphorylated pyridine nucleotides, 1.3 ($NADP^+$ + NADPH) -fold larger relative to *cw15* (Table 2-3). This increase in both NADP(H) and adenylates likely reflects the cellular response to its inability to use the CBB intermediates in forming starch. Although the cellular energy charge did not differ in the two strains in either of the light regimes, the method we used may not be rapid enough to prevent equilibration. Stable CEC is known to be essential for normal cellular function (Kramer *et al.*, 2011).

Metabolites	Abbrev.	*cw15* SS[1]	*cw15* HL[2]	*sta6* SS[1]	*sta6* HL[2]	Fold Change-*cw15 (HL/SS)*[3]	Fold Change-*sta6 (HL/SS)*[3]	*p-value* (*cw15*) [4]	*p-value* (*sta6*) [4]
Glycolysis and CBB intermediates									
ADP-Glucose	ADP-glc	0.019 (0.003)	0.010 (0.001)	0.001 (0.001)	0.001 (0.000)	0.515 (0.102)	0.675 (0.311)	*0.043*	*0.470*
Glucose-1-phosphate	G1P	0.115 (0.006)	0.086 (0.017)	0.063 (0.004)	0.357 (0.091)	0.745 (0.152)	5.63 (1.19)	*0.179*	*0.022*
Glucose-6-phosphate	G6P	0.101 (0.001)	0.076 (0.025)	0.064 (0.004)	0.291 (0.104)	0.753 (0.246)	4.53 (1.14)	*0.373*	*0.046*
Fructose-6-phosphate	F6P	0.058 (0.006)	0.055 (0.029)	0.038 (0.001)	0.313 (0.118)	0.950 (0.509)	8.27 (1.63)	*0.927*	*0.050*
Glyceraldehyde phosphate	GAP	0.077 (0.002)	0.195 (0.048)	0.040 (0.002)	0.474 (0.183)	2.51 (0.626)	11.8 (2.58)	*0.059*	*0.041*
3-Phosphoglycerate	3PG	3.00 (0.091)	5.69 (0.812)	0.386 (0.058)	2.87 (1.091)	1.89 (0.277)	7.45 (1.04)	*0.030*	*0.035*
Phosphoenolpyruvate	PEP	0.736 (0.041)	1.27 (0.210)	0.160 (0.014)	0.702 (0.264)	1.72 (0.302)	4.38 (1.695)	*0.067*	*0.110*
Acetyl-CoA	AcCoA	0.116 (0.003)	0.231 (0.030)	0.205 (0.014)	0.119 (0.042)	1.99 (0.263)	0.581 (0.209)	*0.018*	*0.125*
Ribulose-1,5-bis-phosphate	RUBP	0.082 (0.011)	0.337 (0.019)	0.019 (0.002)	0.099 (0.037)	4.10 (0.583)	5.10 (0.906)	*0.000*	*0.038*
Ribose-5-phosphate	R5P	0.012 (0.002)	0.039 (0.006)	0.013 (0.002)	0.046 (0.016)	3.18 (0.680)	3.62 (1.37)	*0.015*	*0.108*
Xylose-5-phosphate	X5P	0.015 (0.003)	0.071 (0.026)	0.010 (0.002)	0.091 (0.031)	4.77 (2.08)	9.34 (3.76)	*0.105*	*0.059*
Sedoheptulose-7-phosphate	S7P	0.074 (0.022)	0.575 (0.145)	0.061 (0.017)	0.507 (0.174)	8.21 (3.6)	7.74 (3.01)	*0.063*	*0.027*
Lipid Precursor									
Malonyl CoA	MaCoA	0.001 (0.000)	0.001 (0.000)	0.018 (0.000)	0.028 (0.002)	0.968 (0.296)	1.59 (0.071)	*0.9195*	*0.026*

Metabolites	Abbrev.	*cw15* SS[1]	*cw15* HL[2]	*sta6* SS[1]	*sta6* HL[2]	Fold Change- *cw15 (HL/SS)*[3]	Fold Change- *sta6 (HL/SS)*[3]	*p-value* (*cw15*) [4]	*p-value* (*sta6*) [4]
TCA cycle and Amino acids									
Succinate	SUCC	0.712 (0.058)	1.49 (0.131)	0.304 (0.044)	0.594 (0.164)	2.09 (0.251)	1.95 (0.608)	*0.006*	*0.161*
Malate	MAL	1.86 (0.108)	2.63 (0.201)	1.17 (0.152)	1.67 (0.456)	1.41 (0.136)	1.42 (0.429)	*0.028*	*0.360*
α-Ketoglutarate	AKG	0.452 (0.017)	1.13 (0.334)	0.169 (0.030)	0.343 (0.096)	2.50 (0.746)	2.03 (0.675)	*0.112*	*0.159*
Glutamate	GLU	3.32 (0.177)	5.80 (0.378)	2.28 (0.106)	5.35 (1.29)	1.44 (0.147)	2.34 (0.578)	*0.004*	*0.077*
Glutamine	GLN	0.046 (0.002)	0.062 (0.001)	0.082 (0.019)	0.057 (0.018)	1.34 (0.071)	2.08 (0.276)	*0.003*	*0.056*
Sugars									
Sucrose	SUCR	0.011 (0.004)	0.014 (0.002)	0.007 (0.001)	0.044 (0.017)	1.20 (0.421)	6.10 (2.488)	*0.598*	*0.062*
Energy Carriers									
AMP	AMP	1.66 (0.171)	1.60 (0.830)	2.09 (0.521)	2.67 (1.19)	2.16 (0.656)	2.71 (1.329)	*0.137*	*0.217*
ADP	ADP	2.20 (0.206)	2.84 (0.363)	3.43 (0.396)	3.98 (2.23)	1.28 (0.231)	1.15 (0.572)	*0.549*	*0.717*
ATP	ATP	3.40 (0.183)	3.92 (0.826)	6.48 (1.35)	6.21 (1.21)	1.15 (0.256)	0.958 (0.285)	*0.923*	*0.727*
Cellular energy charge (calculated)									
$= \frac{ATP + (0.5 * ADP)}{ATP + ADP + AMP}$	CEC	0.682 (0.060)	0.637 (0.023)	0.620 (0.022)	0.638 (0.076)				

Metabolites	Abbrev.	*cw15* SS[(1)]	*cw15* HL[(2)]	*sta6* SS[(1)]	*sta6* HL[(2)]	Fold Change- *cw15 (HL*/SS)[(3)]	Fold Change- *sta6 (HL*/SS)[(3)]	*p-value* (*cw15*) [(4)]	*p-value* (*sta6*) [(4)]
Pyridine nucleotides									
(NAD^+ + NADH)		1.92 (0.043)	3.06 (0.286)	2.74 (0.118)	2.348 (0.670)	1.43 (0.048)	0.767 (0.300)	*0.454*	*0.752*
($NADP^+$ + NADPH)		0.636 (0.052)	0.873 (0.073)	0.781 (0.027)	1.13 (0.262)	1.22 (0.088)	1.29 (0.246)	*0.213*	*0.783*

Table 2-3 **LC-MS/MS results for various metabolites**. Standard error of mean are represented in parentheses. (1)(2) Represent the concentration of the metabolites in *sta6* and *cw15* under low light conditions(1) (steady state) and high light conditions(2) and calculated as µmoles per 10^8 cells. (3)Represents the fold change in concentration of the metabolites between LL and HL in *sta6* and *cw15* calculated as [HL]/[LL]. (4) Represents the p-value

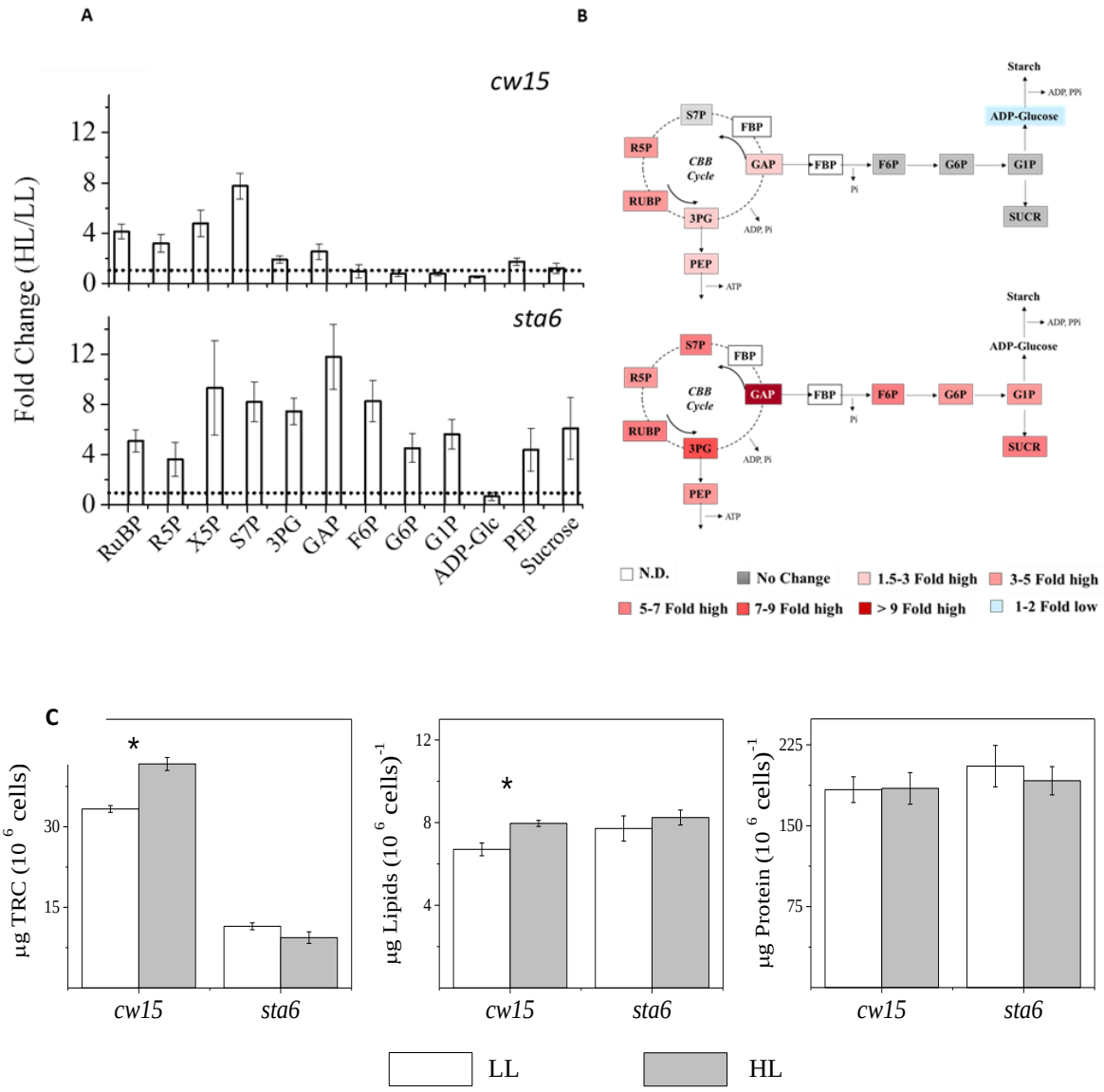

Figure 2-8 **Metabolite and biomass distribution**. Summary of metabolomics data for CBB cycle and gluconeogenic pathway. A) The fold changes in the metabolites occurring during low light to high light transition in *sta6* and *cw15*. Dotted line in A represents no-fold change B) Schematic representation of the fold changes of the metabolites given in A. C) Biomass distribution (Total reducing carbohydrates, TRC; lipids and proteins) during the low light to high light shift. White bars represent the biomass content under low light condition and grey bars represent the biomass after HL shift. Data represent the mean of three biological replicates with standard error.

3.7) Photosynthetically fixed carbon in sta6 is redirected towards lower glycolysis

Metabolites of central carbon metabolism outside of the CBB cycle involved in biosynthesis of amino acids, fatty acid and alternative CO_2 fixation (C4) were quantified and compared across the two strains (Table 2-3). In *sta6*, the high energy phosphate ester, phosphoenolpyruvate (PEP) increased by 4-fold, further signaling the accumulation of excess cellular phosphate and energy. Amongst the TCA cycle metabolites, succinate and α-ketoglutarate increased uniformly in both strains. Although *sta6* does not accumulate protein, the amino acid precursors glutamine and glutamate, increased both at LL and HL intensities compared to *cw15*. Significantly, from the perspective of lipid biosynthesis, the level of the fatty acid precursor malonyl-CoA is 18-fold higher in *sta6* compared to *cw15*, and increased further to 28-fold upon high light shift, although the total lipid content in *sta6* was indistinguishable from *cw15*.

4. Discussion

The use of various starchless mutants as test strains in search of higher lipid producers has been investigated in multiple prior studies (Work et al., 2010; Goodson et al., 2011; Li et al., 2010a; Li et al., 2010b; Siaut et al., 2011; Fan et al., 2012; Wang et al., 2009; Blaby et al., 2013; Goodenough et al., 2014). These studies also found that loss of starch synthesis and lower growth rates were strongly correlated, but the consequences on the individual PET reactions and carbon partitioning via pathways and into terminal products had not been examined systematically at the molecular level until now. In Scheme 2-1 we summarize our data describing the molecular phenotype arising from loss of AGPase in the *Chlamydomonas* starchless mutant, *sta6*.

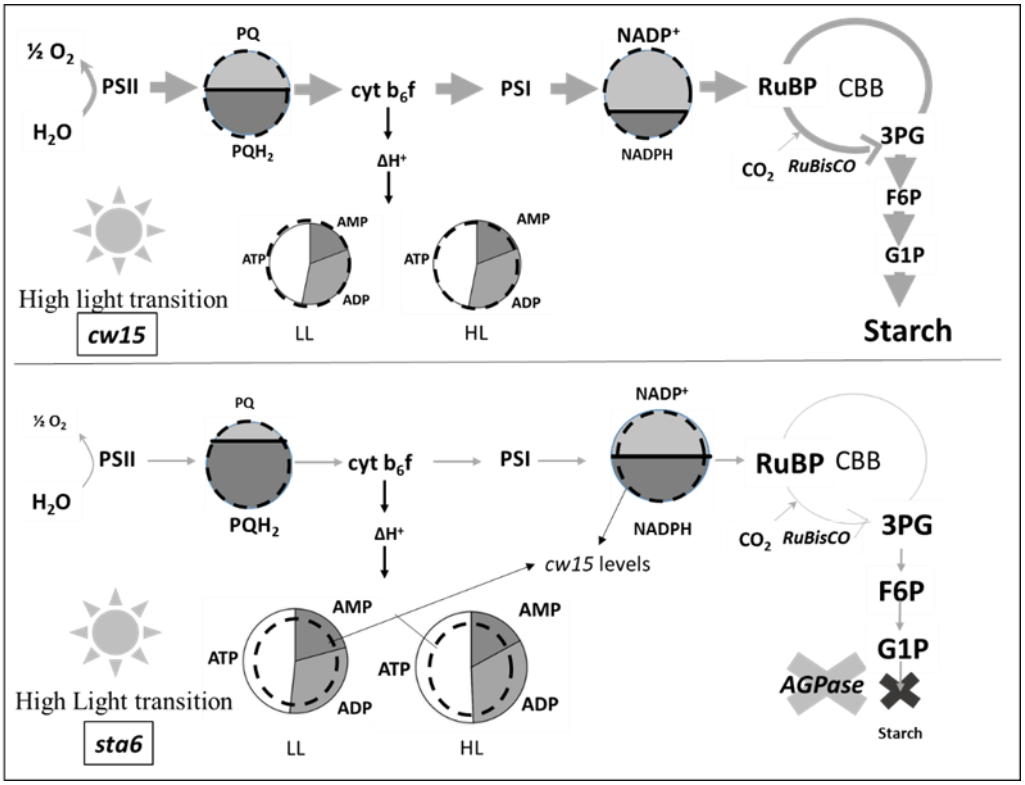

Scheme 2-1 **Schematic representation of metabolism in *sta6*.** Schematic representation of light dependent and independent reactions of photosynthesis in the *sta6* strain (deletion in the small subunit of AGPase, denoted by X), while *cw15* is the control strain. Thick and thin arrows represent large and small electron fluxes through WOC, PET and the CBB cycle, with *sta6* having a 2-fold slower electron flux than *cw15*. Small and large font sizes indicate (qualitative) differences in relative contents. Circle areas are quantitatively proportional to the total pool sizes in the cell (dashed circle for *cw15*, solid circles for *sta6*). Dashed circle in the sta6 panel shows the pool size of the metabolite in *cw15* super imposed onto *sta6* pool size indicating that sta6 has a larger pool size of NADP(H) (1.2-fold) and adenylates (1.6-fold) vs *cw15*, but similar plastoquinone pool sizes. The ratio of NADPH/NADP+ and plastoquinol/plastoquinone pool sizes is qualitatively represented by the dark and light gray colors.

Starch (or glycogen in cyanobacteria) biosynthesis is essential for (at least) four purposes: a) consuming the photosynthetically generated reductant (NADPH) and ATP (Kramer and Evans, 2011), b) providing the gluconeogenic route needed for replenishing the CBB cycle intermediates, c) as a low osmotic potential storage product for carbon and energy need during dark, and d) photoprotection against oxidative damage. In the absence of starch biosynthesis arising from a non-functional AGPase, all of these functions are disrupted. Especially at high light, starting with the primary impact on the rate of CO_2-dependent water oxidation, *sta6* has a 3.5-fold slower rate than *cw15* under the conditions in Fig. 2-3 A. This leads to a buildup in the reductant poise ($NADPH/NADP^+$), the extent of carbohydrate phosphorylation, and the adenylate nucleotides, the latter presumably in an attempt to compensate for the slower turnover rate (Scheme 2-1). Accumulation of several phosphorylated carbohydrates (Table 2-3) (Scheme 2-1) and the upper glycolysis intermediates (G1P, G6P and F6P) occurs which do not drain efficiently to terminal sinks. This outcome together with the 2.8 fold larger adenylate pool size will result in a corresponding decrease in the available free Mg^{2+} in the stroma of the chloroplast. As Mg^{2+} is a required activator for RuBisCO and other CCB enzymes, allosteric down regulation of RuBisCO-dependent CO_2 fixation activity is expected in *sta6* if not offset. This down regulation appears to be directly responsible for the slowing of NADPH oxidation and ultimately slowing all PET reactions as far upstream as water oxidation by PSII. The CCB cycle appears to be the main target impacted by the AGPase mutation in *sta6* as none of the individual PET enzyme fluxes exhibit inhibition relative to the *cw15* control when measured in isolation. Our results with PET electron acceptors (Fig. 2.5 C) confirm that, like typical wild algal strains (Rochaix, 2011), reoxidation of the PQ pool is retained in *sta6* as the slowest kinetic step of the PET chain. *sta6* uses mitochondrial respiration to relieve its slowly responding, over reduced, PET chain (Fig. 2.5 B). By contrast, inhibition of mitochondrial respiration in *cw15* leads to a comparatively insignificant effect on OER. Thus, respiration appears to be critical for sustaining the low level of photosynthetic oxygen

evolution in *sta6*. Consistent with this observation, $P700^+$ kinetics are impaired when respiration is inhibited in *sta6* (Johnson *et al.*, 2012). Under conditions where *sta6* is unable to maintain redox homeostasis, *sta6* does not depend on PTOX or AOX but potentially Mehler reaction or photorespiration to reduce O_2 and relieve the excess reductant. Thus alternate oxygen consuming pathways become important as redox valves in *sta6.*

The large 4-fold increase in PEP concentration in *sta6* is interesting to note as this molecule is known to function in another CO_2 fixation pathway via phosphoenolpyruvate carboxylase (PEPC) which may therefore become more important in *sta6*. PEPC catalyzes the reaction combining bicarbonate (HCO_3^-) and PEP to form oxaloacetate. This is an anaplerotic reaction important for amino acid (Ala, Asp, Glu) synthesis. PEPC dependent carbon fixation can even exceed the amount of carbon fixed via the CBB cycle in some unicellular algae under nitrogen limited conditions (Guy *et al.*, 1989).

sta6 maintained smaller metabolite pool sizes of hexose phosphates (hexose-P) under low light. In the absence of starch biosynthesis with limited carbon fixation, the fixed carbon might be dynamically redirected to TCA cycle to sustain the high levels of protein required for growth leading to a smaller pool size of hexose-P. While, under HL, the TCA cycle appears to become saturated (Table 2-3) forcing an accumulation of the hexose-P. Future metabolic flux analysis can guide in understanding this dynamic redirection of metabolites.

Even though over-reduction of the PET chain is relieved in part by mitochondrial respiration in *sta6* (Fig. 2.5 B), prolonged exposure to high light leads to an accelerated photoinhibition relative to *cw15* (Fig. 2.7 B), indicating that starch production is an important safeguard against photodamage. The light-driven accumulation of excess NADPH and reduced ferredoxin are widely observed to lead to the formation of reactive oxygen species (ROS) in many aquatic phototrophs and plants. A similar phenotype is observed in several other characterized AGPase mutants (Sun et al., 1999; Grundel et al., 2012; Suzuki et al., 2010). Given that starch is the least energy intensive

terminal product among starch, proteins and lipids, it may serve as a low-barrier energy storage buffer to both protect against light energy fluctuations and to enable the biosynthesis of these more energy intensive biopolymers during low light periods, similar to that postulated in higher plants (Caspar *et al.*, 1985), (Stitt *et al.*, 1989), (Ludewig *et al.*, 1998), (Weise *et al.*, 2011) (Geigenberger, 2011).

Carbon that enters central metabolism from the CBB cycle may take two possible routes: the upper gluconeogenesis pathway leading into C6 and C5 carbohydrates, or the lower glycolytic pathway leading to acetyl-CoA that can branch either into the TCA cycle to synthesize amino-acids or to malonyl-CoA to synthesize lipids. Several groups have reported increased lipid yields in *sta6* after switching cells to nitrogen deprived growth medium (Work et al., 2010; Goodson et al., 2011; Li et al., 2010a; Li et al., 2010b; Siaut et al., 2011; Fan et al., 2012; Wang et al., 2009). Increased lipid accumulation is not observed under nutrient replete, photoautotrophic conditions *in sta6*, rather growth is stunted. However, there is a major increase in both acetyl-CoA and malonyl-CoA levels in *sta6*. Malonyl-CoA formation is catalyzed by ACCase through an ATP-dependent carboxylation reaction of biotin that transfers a carboxyl group to acetyl-CoA (Berg et al., 2002). The ACCase reaction is considered to be the committed step in fatty acid synthesis as there is no other use for this intermediate other than fatty acid production. It is regulated by reversible phosphorylation catalyzed by an AMP-dependent protein kinase (AMPK) (Berg et al., 2002). ACCase is inhibited by its' phosphorylation, while the unphosphorylated form has carboxylase activity. AMPK itself acts as an adenylate nucleotide sensor, being activated by high AMP levels and inhibited by high ATP levels (Berg et al., 2002; Hardie et al., 2002). As such the kinase activity becomes self-limiting at high ATP concentrations. Accumulation of malonyl-CoA in *sta6* indicates a reversal of inhibition of ACCase relative to *cw15*. Given that ATP accumulates in *sta6* (Table 2-3), we predict that the higher ATP content likely inhibits AMPK and, in turn, enhances the carboxylase activity of ACCase. Thus, a simple overexpression of ACCase may not be enough to

enhance ACCase activity, but needs to occur in parallel with lowering the level of phosphorylation of ACCase, which is achieved by suppression of AMPK phosphorylation activity. Taken together, higher ATP accumulation in *sta6* cells metabolically poises it for higher levels of fatty acyl biosynthesis as seen by elevated levels of acetyl-CoA and especially malonyl-CoA, but downstream blockage in the fatty acid synthesis complex prevents utilization. Thus under photoautotrophic nutrient replete conditions, the activity of the fatty acid synthesis complex, or glycerolipid biosynthetic enzymes appear to be limiting lipid biosynthesis. If the activity of these enzymes are increased (as under nitrogen starvation), it may enable *sta6* to utilize the enhanced Ma-CoA. Transcriptomic studies on *C.reinhardtii* have shown a significant increase in the acyl transferases such as acyl-CoA:diacylglycerol acyltransferase (DGAT) and phospholipid:diacylglycerol acyltransferase (PDAT)) and suggested the involvement of transcription factor NRR1 in potentially regulating the expression of certain DGAT genes (Boyle *et al.*, 2012). Thus, factors beyond precursor availability control lipid biosynthesis.

In conclusion, our data indicate that in *C. reinhardtii*, starch biosynthesis plays a critical role in regulating multiple functions largely through the accumulation/utilization of excess redox and adenylate cofactors. Future research efforts should examine mechanisms to effectively leverage the greatly increased malonyl-CoA levels for enhanced lipid biosynthesis which if successful could allow higher NADPH reoxidation rate and restore high levels of photosynthetic growth.

Chapter 3: The carbon decision tree of *Chlamydomonas reinhardtii*: How starchless mutant strains redirect carbon metabolism.

Anagha Krishnan[1], Huiya Gu[2], G. Kenchappa Kumaraswamy [1], Gennady Ananyev[3], Matthew Posewitz[2], G. Charles Dismukes[1,3,]*

[1]Waksman Institute of Microbiology, Rutgers, the State University of New Jersey, Piscataway, NJ 08854, [2]Department of Chemistry and Geochemistry, Colorado School of Mines, Golden, CO 80401, [3]Department of Chemistry & Chemical Biology, Rutgers, the State University of New Jersey, Piscataway, NJ 08854,

Summary

Imposed nutrient starvation is a widely used tool to shift microbial cellular metabolism to favor selected bioproducts, but typically causes reduced phototsynthetic rates and biomass accumulation. Under nitrogen (N) starvation, the microalga *Chlamydomonas reinhardtii* redirects biosynthesis from proteins to starch and lipids, and in mutants lacking starch biosynthesis enzymes, preferentially to lipids. To understand the molecular basis for this altered carbon partitioning, a comparative analysis of the intracellular pools of central carbon metabolites and their ^{13}C fluxes upon N deprivation in strains with and without modified starch synthesis was performed. Both transient ^{13}C-metabolites fluxes produced from fixed $NaH^{13}CO_3$ and steady-state metabolite pool sizes reveal sustained fluxes through gluconeogenesis as system wide responses to N starvation in all strains. Simultaneous measurements of adenylate nucleotides (ATP, ADP, AMP) revealed a tight correlation between elevated cellular energy charge (CEC) and the flux into gluconeogenesis. Gluconeogenic flux is maintained even in mutants blocked at starch polymerization, but carbon is redirected to the oxidative pentose phosphate (OPP) pathway via G6P, initially forming GAP and DHAP, and ultimately into fatty acid precursors (Mal-CoA). Activation of the OPP pathway produces a significant loss of fixed carbon as CO_2 and the co-generation of excess reductant (3

NADPH per G6P). Thus, the starchless mutant strains use the OPP pathway as a shunt to reallocate photosynthate fated for starch, instead into lipids at the expense of reduced biomass accumulation.

1. Introduction

The use of microalgae as cell factories for making fuel precursors is being extensively investigated, with a focus on improving cell growth rates and boosting product yields, typically lipids and isoprenoids (Chisti, 2013); (Melis, 2013). The fastest growing strains often exhibit the lowest lipid productivity. Indeed, these rates have been shown to be inversely correlated (Rodolfi *et al.*, 2009);(Hu *et al.*, 2008); (Wijffels *et al.*, 2010). There is both a kinetic and thermodynamic origin to this inverse correlation. Under rapid growth conditions in nutrient replete media, functional proteins and membrane lipids are the synthesized first, with amino acid biosynthesis being the major sink for primary photosynthate (50-60% of the dry weight). This is typically followed by glycogen/starch accumulation as energy storage carbohydrates. Storage forms of lipids such as triacylglycerides (TAGs) are the slowest to accumulate. This sequence is not surprising as TAGs have twice the energy content of starch per carbon atom and correspondingly consume more reductant for biosynthesis. By contrast, nutrient starvation especially nitrogen (N) starvation, inhibits protein biosynthesis and stimulates the accumulation of non-polar lipids in the form of TAGs (up to 50%) and starch (up to 60%) (Siaut *et al.*, 2011); (Breuer *et al.*, 2012), but severely decreases photoautotrophic growth rates and thus total biomass yields (Chisti, 2007); (Hu *et al.*, 2008). This loss of photosynthesis leads to greater reliance on reduced carbon sources for growth and repair (homeostasis).

Rerouting of carbon flux under nitrogen deprivation results in accumulation of starch and lipid at the expense of protein biosynthesis in many algal strains (Rodolfi *et al.*, 2009); (Hu *et al.*, 2008) including the *Chlorophyceaen* alga *Chlamydomonas reinhardtii (henceforth, C. reinhardtii)* (Ball *et al.*, 1990). Msanne et al, have shown that starch and lipid accumulation are temporally separated under N starvation (Msanne *et al.*, 2012), and this has been shown to be regulated at the mRNA transcript level (Blaby *et al.*, 2013); (Goodenough *et al.*, 2014). In *C. reinhardtii*, starch accumulates first in response to nitrogen starvation, primarily serving as a short-term carbon and

energy store, while TAGs accumulate after more prolonged periods of N starvation (Siaut *et al.*, 2011); (Zhu *et al.*, 2014); (Blaby *et al.*, 2013).

A key unknown is the complex regulation of carbon partitioning into the various terminal sinks that has hindered efforts to substantially alter carbon allocation between lipids and other products while maintaining growth rate (Melis, 2013). The partitioning of assimilated carbon between TAGs and carbohydrates is a highly regulated process, as indicated by the activity of the various transcription factors and the observed changes in the transcriptome and proteome (Wase *et al.*, 2014); (Blaby *et al.*, 2013); (Miller *et al.*, 2010); (Goodenough *et al.*, 2014). At the metabolite level, both of these sinks share the same precursors. The primary product of CO_2 fixation, 3PG can feed directly into starch biosynthesis through gluconeogenesis or can be directed into lower glycolysis to produce acetyl-CoA and malonyl-CoA, precursors for fatty acids (FA) (Fig. 3-1). In *Chlamydomonas*, both starch and fatty acid synthesis occurs in the same intracellular compartment, the chloroplast, and thus direct competition for these metabolites should occur. Hypothesizing a direct competition for carbon precursors, several groups have already reported success in increasing lipids by eliminating starch biosynthesis (Work *et al.*, 2010); (Blaby *et al.*, 2013); (Goodenough *et al.*, 2014); (Wang *et al.*, 2009); (Goodson *et al.*, 2011); (Siaut *et al.*, 2011); (Breuer *et al.*, 2014); (Li *et al.*, 2010); (Miller *et al.*, 2010). However, the work with genetically complemented strains showed increased levels of both lipids and starch (Work *et al.*, 2010), as well as modulated levels of photosynthetic activities as a function of sink strength, suggesting that the carbon partitioning between lipids and starch is more complex than mere competition for precursors (Work *et al.*, 2010); (Ramazanov *et al.*, 2006); (Breuer *et al.*, 2012); (Miller *et al.*, 2010).

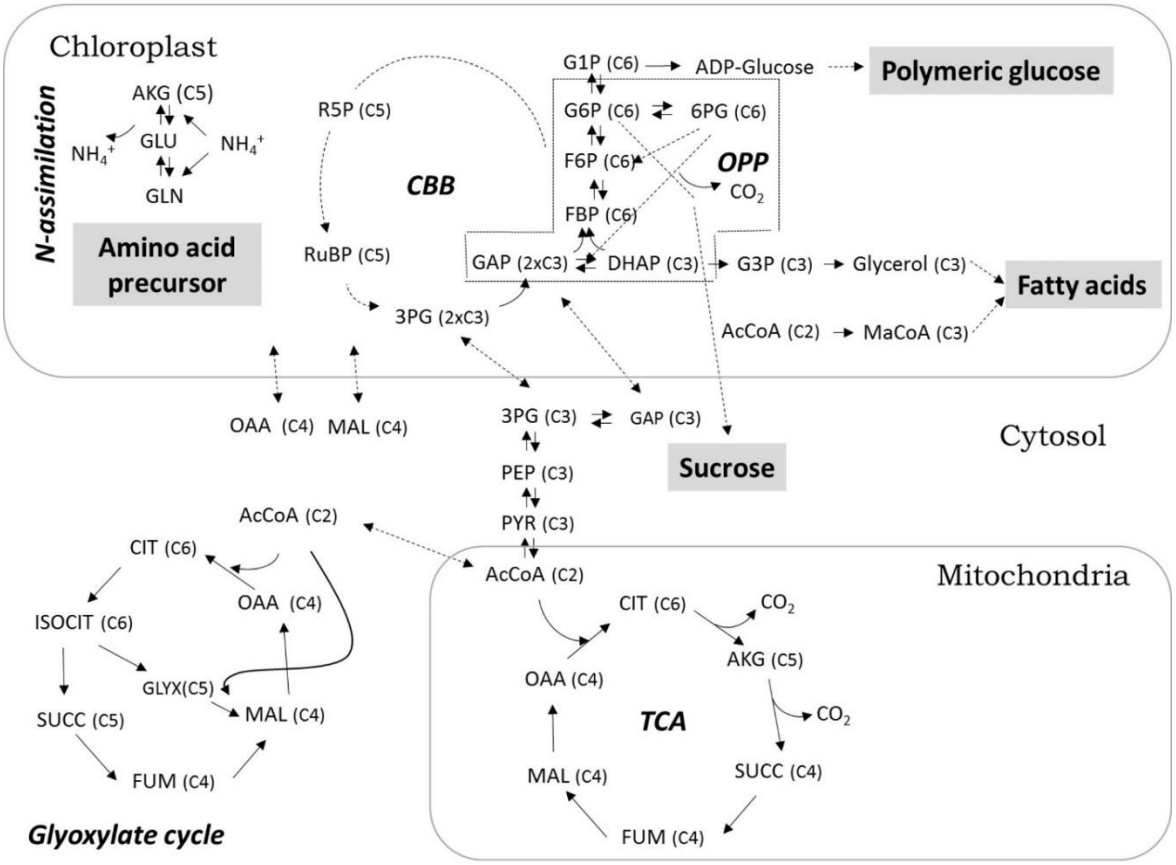

Figure 3-1 **Metabolic pathways in *Chlamydomonas reinhardtii*** .Metabolic pathways in *Chlamydomonas reinhardtii* adapted from (Johnson et al., 2013). Abbreviations: CBB, Calvin Benson Bassham cycle; OPP, oxidative pentose phosphate pathway; TCA, tricarboxylic acid cycle; G1P, glucose-1-phosphate; G6P, glucose-6-phosphate; F-6-P, fructose-6-phosphate; FBP, fructose bisphosphate; GAP, glyceraldehyde 3-phosphate; DHAP, dihydroxyacetone phosphate; 3PG, 3 phosophoglycerate; RUBP, ribulose bisphosphate; Glu, glutamate; Gln, glutamine; PEP, phosphoenol pyruvate; PYR, pyruvate; Ac-CoA, acetyl-CoA; CIT, citrate; AKG, α-ketoglutarate; SUCC, succinate; FUM, fumarate; MAL, malate; OAA, oxaloacetate; ISOCIT, isocitrate; GLYX, glyoxylate

Understanding the carbon decision tree - the temporal and spatial coordination of biochemical pathways responsible for biosynthesis and catabolism of the major carbon sinks is still fragmentary in microalgae. Here, we apply LC-tandem-MS methods to determine steady-state metabolite concentration changes during nitrogen starvation and time-resolved ^{13}C metabolite kinetics. We identify the main metabolic nodes where redirection of carbon between pathways occurs during nutrient stress, leading to accumulation of starch, or lipids, in both wild type and starchless mutant strains. In contrast to most prior work, we have used autotrophic conditions to strictly avoid any dependence on external reduced carbon. We find that under nitrogen starvation there is selective inhibition of the TCA cycle and active allocation of carbon into gluconeogenesis, irrespective of the presence or absence of starch. Rather than directly channeling the fixed carbon to fatty acids, the starchless mutants use the oxidative pentose phosphate pathway (OPP) to redirect the carbon entering gluconeogenesis to alternate sinks. In addition, we provide evidence indicating ATP/AXP (cellular energy charge) as a potential effector for regulating this metabolic switch.

2. Experimental Procedures:

2.1) Strains and Culture conditions:

cw15 sta6 (BAFJ5, henceforth, *sta6*) (Wang *et al.*, 2009), (Zabawinski *et al.*, 2001), CC-124 wild type mt- [137c] (henceforth CC124), CC-4425 *cw15* nit2-203 mt+ [D66] (henceforth D66), and CC-4349 *cw15* mt^+ (Goodenough 330A, henceforth, *cw15*) were obtained from the Chlamydomonas resource center (University of Minnesota). The starchless mutant strain (*sta7-10*) in the CC425 background (henceforth *sta7*), and its genetic complement (*c19*) were isolated as described previously (Work *et al.*, 2010). The lineages of the six strains is summarized in Supporting Information (Fig. 3-2).

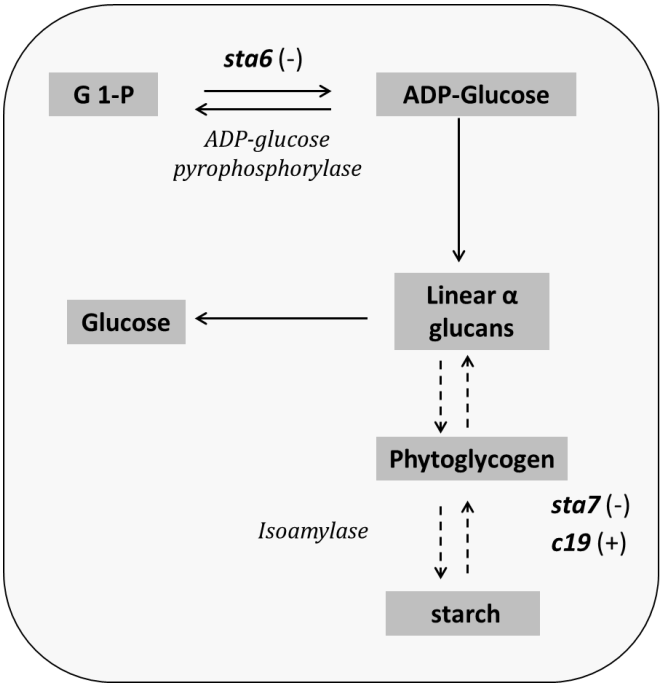

sta6	Starch-less, produces soluble sugars (9.8% sugar)
sta7	Starch-little (phytoglycogen), highly branched polymeric sugars (19.5% sugar)
c19	*sta7*-complement, high starch and lipids biosynthesis
cw15	Cell-wall less control (31.8% sugar)
D66	Cell-wall less control
CC124	Cell-wall containing control

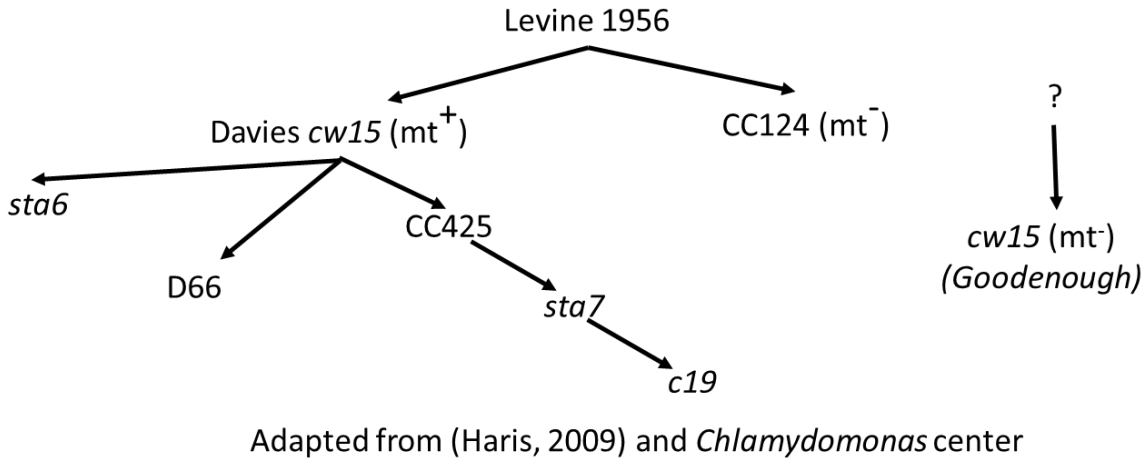

Figure 3-2 **Relationships among the strains chosen for carbon partitioning analysis**.

sta6 and *sta7* are unable to produce starch owing to genetic lesions that block starch synthesis in these strains. In *sta6*, the small catalytic subunit of ADP glucose pyrophosphorylase is disrupted via insertion of pArg7.8 into the genome of CC-4568 strain and as a result, the ADP-glucose fated for starch biosynthesis is not synthesized. This mutant accumulates less than 1% of the starch observed in the WT cells under nutrient starvation (Ball *et al.*, 1990), (Work *et al.*, 2010) The *sta7* mutant contains a disrupted isoamylase gene due to insertion of the pJD67 into the genome of the CC-425 background strain. Isoamylase is an important debranching enzyme needed for the proper formation of crystalline starch. In the absence of isoamylase, *sta7* has a severely attenuated starch accumulation phenotype and instead accumulates a glycogen like product (Mouille *et al.*, 1996), (Dauvillee *et al.*, 2001; Work *et al.*, 2010). *c19* clone was previously isolated by complementing *sta7* with the isoamylase gene (Work *et al.*, 2010). *c19* was found to accumulate higher levels of starch and lipids as compared to *sta7* under nitrogen starvation in the presence of acetate (Work *et al.*, 2010) and is used as one of the starch synthesizing controls in this study. Previous research has shown significant variability in starch and lipid accumulation in different laboratory strains (Siaut *et al.*, 2011). Therefore, for generalizing our results we examined three starch synthesizing control strains *cw15*, D66 and CC124. Comparing a range of strains should enable the identification of a global response pattern to nitrogen starvation while the addition of starchless mutant strains will help in elucidating carbon partitioning.

Liquid cultures were grown in phosphate buffered, Sueoka's high salt medium (HS) supplemented with 9.4 mM NH_4Cl (Harris *et al.*, 2009). The cultures were maintained on an orbital shaker (120 rpm) under continuous illumination (80-100 $\mu E\ m^{-2}\ s^{-1}$ PAR) at 26^{o}C and maintained under 1% CO_2/air atmosphere. For nitrogen starvation experiments, cultures were grown to late log phase in nitrogen replete HS media, harvested, washed with NH_4Cl free HS media (HS-N) and resuspended at ~2.5 x 10^6 cells ml^{-1} in either HS media replete with NH_4Cl (HS+N) or HS-N media. Samples

for analysis were taken at multiple time points as indicated in the main text. Cell counts were analyzed using a Z2 counting chamber.

2.2) Lipid, glucose and protein analysis

Total lipids were quantified using GC-FID after converting lipids to fatty acid methyl ester via transesterification (Work *et al.*, 2010,); (Radakovits *et al.*, 2012). The anthrone assay was used to quantify the total reducing carbohydrate content (Morris, 1948). Total protein content was determined using the DC protein assay kit (Bio-Rad, Hercules, CA) according to the manufacturer's instructions.

2.3) Metabolite extraction and analysis

LC-MS/MS analysis was done as described previously (Krishnan, 2015). Briefly, 1.8 ml of *C. reinhardtii* cultures were injected into 0.2 ml of an 80:20 MeOH:water mixture for fast quenching and centrifuged at 5000 rpm for 2 min at -10^{o}C. The supernatant was carefully removed and the pellet was resuspended in 60µL ice-cold extraction solvent (60:40 MeOH:water). The suspension was sonicated in a bath sonicator for one min then incubated at -20^{o}C for 20 min. To remove cell debris, the samples were centrifuged for 5 min at 5000 rpm at -10^{o}C. Supernatant was vacuum dried (CentriVap Benchtop Vacuum Concentrator, *Labconoco*) and the resulting pellet was resuspended in LC-MS grade water. These samples were injected into an *Agilent* 6490 triple quadrupole mass analyzer coupled to a high performance liquid chromatograph (HPLC, *Agilent Technologies*) for targeted metabolite analysis (Kenchappa *et al.*, 2013). Standard solutions at 5 different concentrations were used to obtain calibration curves for each metabolite. Final concentrations of each metabolite per 10^6 cells were calculated using the calibration curve. Fold changes were calculated as a ratio of concentration of metabolites at the given test condition divided by the time 0 (T_0). Cellular energy charge (CEC) was calculated as:

$$CEC = \frac{ATP + 0.5 \times ADP}{ATP + ADP + AMP}$$

To analyze metabolic flux, ^{13}C-labeling was performed using 10mM ^{13}C $NaH^{13}CO_3$ in addition to the already existing 5mM ^{12}C $NaH^{12}CO_3$ in the medium (see main text). Briefly, the cultures were grown to late log phase, washed with HS-N medium and resuspended in either HS+N or HS-N medium supplemented with 5mM $NaH^{12}CO_3$ to acclimate the cells to bicarbonate as the carbon source. HS+N cultures were allowed to grow for 3 h and then used for ^{13}C-labeling. For HS-N labeling analysis, cultures were grown for 21 h in HS-N medium, washed and resuspended in fresh media (HS-N + 5mM ^{12}C $NaH^{12}CO_3$) to avoid any artifacts in ^{13}C-labeling caused by the accumulation of waste products or by nutrient depletion (Yuan *et al.*, 2008). These samples were allowed to grow for another 3 h, thus covering the total growth period of 24 h under –N conditions and then used for ^{13}C-labeling. 10mM ^{13}C $NaH^{13}CO_3$ was added to the cell culture to initiate labeling. Samples for metabolite analysis were withdrawn at 0 s (prior to ^{13}C-label addition), 30 s, 1 min, 2 min, 4 min, 15 min and 30 min, and analyzed by LC-MS/MS as described above. The fraction of ^{13}C-labeled fraction of metabolites was determined as described previously (Hasunuma *et al.*, 2010). Briefly, the ^{13}C-labeled fraction % of a metabolite containing n carbon atoms is calculated as

$$13C\ fraction\ (\%) = 100 * \sum_{i=1}^{n} \frac{i \times mi}{n}$$

where mi is the total ion count for the isotopomer of the metabolite containing i ^{13}C atoms. Metabolic turnover rate was calculated from the initial slope of the ^{13}C fraction vs time from 0-2 min (Hasunuma *et al.*, 2010).

2.4) Pyridine nucleotide fluorescence kinetics:

Intrinsic NAD(P)H fluorescence emission was measured in whole cells with a home-built fluorometer as described previously (Williams *et al.*, 2010), (Krishnan *et al.*, 2015), (Mi *et al.*, 2000). For NAD(P)H excitation, an LED (365 nm wavelength) in combination with an optical filter (2 mm UG 11, Schott) was used, while emission intensity was detected by a filtered low noise

photomultiplier (PMT, R2059, *Hamamatsu, Japan*). To eliminate scattered measuring light and chlorophyll fluorescence emission into the PMT, a combination of a long-pass filter (KV418, *Schott*), a short-pass filter (DT Cyan), and a blue-green glass filter (BG39, *Schott)* were used that restricted transmission to 420∓10 nm. The detection and excitation pathways were perpendicular. Red actinic illumination was provided by a bright LED (660± 5 nm), Hewlett-Packard). An NMR tube (outer diameter 5 mm) was used as the sample holder. Cells were harvested every 24 h post nitrogen starvation, washed and resuspended in 20% ficoll solution made in HS+N media and containing 5 mM bicarbonate. Ficoll was used to slow the settling rate of cells in the fluorometer. The sample emission was normalized to the same total pyridine nucleotide ($NADP^+$ + NADPH) content determined by LC-MS/MS (0.25 μM ml^{-1}). Samples were dark adapted for 25 min to get a stable base line before beginning the actual measurements.

3. Results:

3.1) N starvation induces C flux changes between lipids, proteins and carbohydrates.

Fig. 3-1 is a schematic representation of the central carbon metabolism of *C. reinhardtii* based on the model described by Johnson and Alric (Johnson *et al.*, 2013). To analyze carbon partitioning under N starvation, six *C. reinhardtii* strains were chosen: two starchless mutants (*sta6* and *sta7*) and four starch synthesizing strains (CC124, D66, *cw15* and *c19*) *(See Materials and methods,* Fig. 3-2*).* For quantifying biomass accumulation under N starvation, all the strains were precultured photoautotrophically to late log phase in HS+N medium and kept under a 1 % CO_2/air atmosphere (*See Materials and methods*). Cultures were then centrifuged and resuspended in HS-N medium at fixed cell densities and allowed to grow for 96 h under 80-100 μE m^{-2} s^{-1} of white light. The major biochemical products, including total reducing carbohydrates (TRC), lipids and proteins were quantified in all six strains at 0h, 24h and 96h after initiation of nitrogen starvation (Fig. 3-3). As controls, the strains were also grown in HS+N media.

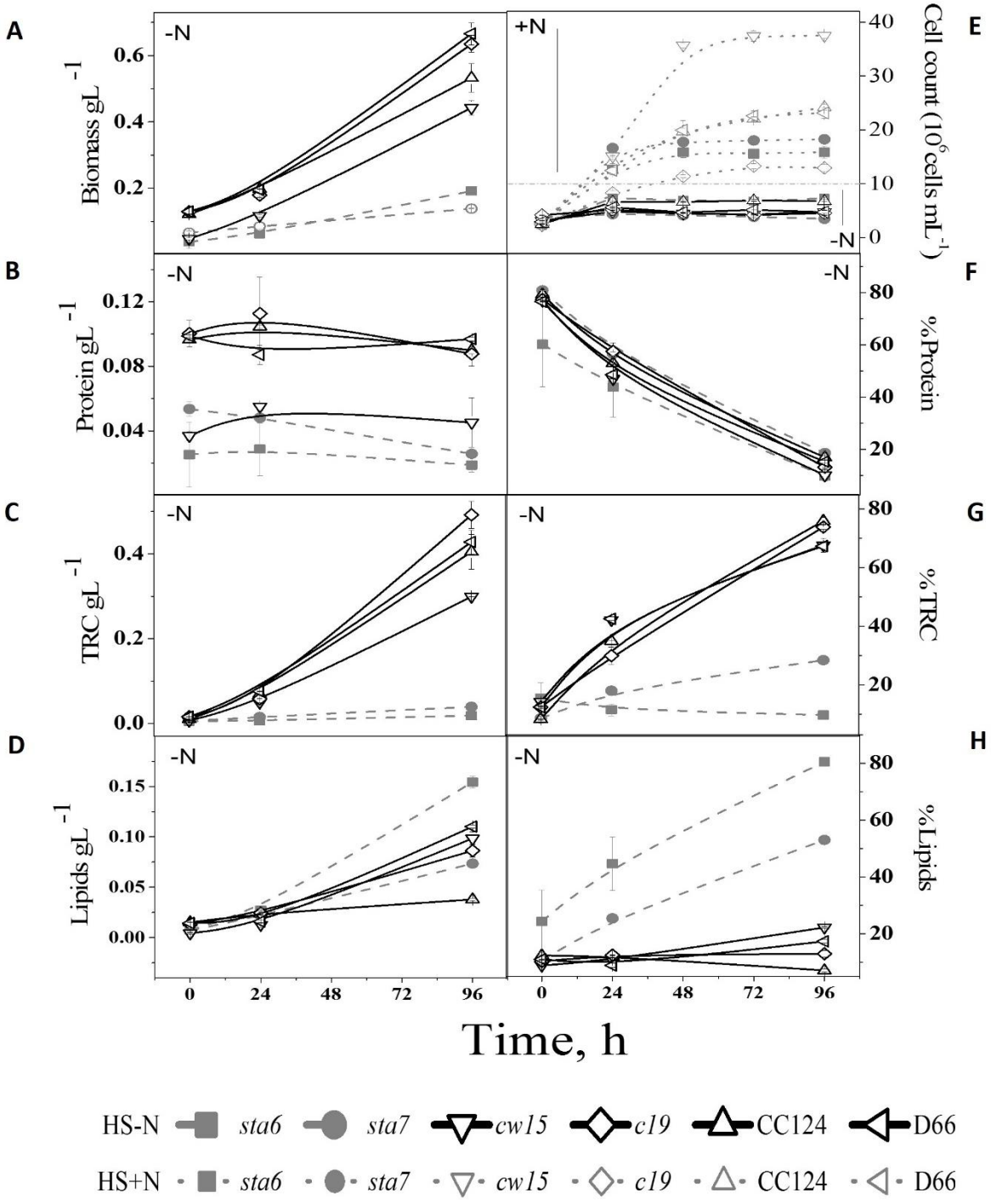

Figure 3-3 **Changes in biomass composition of six *C. reinhardtii* cultures under nitrogen starvation**. A) Total biomass content (g L-1), B) total protein, C) total reducing carbohydrate, and D) total lipid content in (g L-1). E) is the growth curve displaying the changed in cell density over time for all the six strains in nitrogen replete media (+N) above the dotted line and N-free media (–N) below the dotted line. F) proteins, G) total reducing carbohydrates (TRC), and H) lipids during N starvation, each expressed as percentage of the total biomass. Values are the average of 3 measurements ± SE.

As expected, after 96 h of nitrogen starvation, all strains grew much slower relative to nitrogen replete culturing, experiencing at most one cell doubling (Fig. 3-3 B). However, the calculated biomass (given by the sum of the three major fractions: TRC + proteins + lipids) increased at least 2.5 fold (Fig. 3-3 A), indicating active carbon fixation taking place under nitrogen starvation rather than merely remodeling of carbon from preexisting biomass. Among the starchless mutant strains, *sta6* and *sta7*, accumulated 2-5 fold less biomass than the starch-synthesizing control strains after 96 h of N starvation (Fig. 3-3 A).

As expected, in the absence of N, starch (measured as total reducing carbohydrates, TRC) and lipids become the dominant sinks in starch competent strains (Fig. 3-3 C & D), while in *sta6* and *sta7* there was no significant increase in TRC content over 96 h of N starvation (Fig. 3-3 C & G). This contrasts with the absolute protein content (Fig. 3-3 B), which did not change appreciably or had a minor loss (*sta7*). After normalization to total calculated biomass, the protein fraction of total cellular biomass decreased by up to 4.5 fold (Fig 3-3 F). Amongst all the strains, *sta6* accumulated the highest lipid content on a dry weight basis under these photoautotrophic conditions (Fig. 3-3 D & H). The other starchless mutant, *sta7*, had a smaller increase in lipid content versus *sta6* on a weight basis (g L^{-1}), though it synthesized more lipids compared to starch competent strains on a % biomass basis (Fig. 3-3 D & H). Among the starch synthesizing strains, CC124 had the lowest lipid content (-N) at 96 h, consistent with the reported range found among the different *C. reinhardtii* control strains (Siaut *et al.*, 2011). The presence of a cell wall in CC124, which supports a higher osmotic pressure unlike the other strains, may contribute to its reduced lipid content (Johnson *et al.*, 2013).

3.2) Metabolic responses to N starvation.

Given that the starchless mutants preferentially partition carbon into lipids, we sought to identify how this is represented in the profile of intracellular metabolites by determining the concentrations of the central carbon metabolites for all six strains (+/- N) using LC-MS/MS

methods (Bennette *et al.*, 2011), (Krishnan, 2015). Initially, a time-coarse profile was taken, with sampling at 0, 24 and 96 h after the initiation of N starvation. For 0 h measurement, the samples were suspended in HS+N medium at the same cell density as that in the HS-N medium. The experimental setup is shown in Fig. 3-4 F. Individual metabolite concentrations are given in Table 3-1. The time-course results of all the detected metabolites are summarized in Fig 3-4 A. Columns represent the fold-change in the metabolites occurring at the different starvation points for each individual strain. Fold-changes are calculated relative to the initial metabolite concentrations at time zero, T_0. Because we are comparing six strains of different lineages, we chose to bin these in units of 3-fold differences to focus on major trends. Greater detail can be found in Table 3-1.

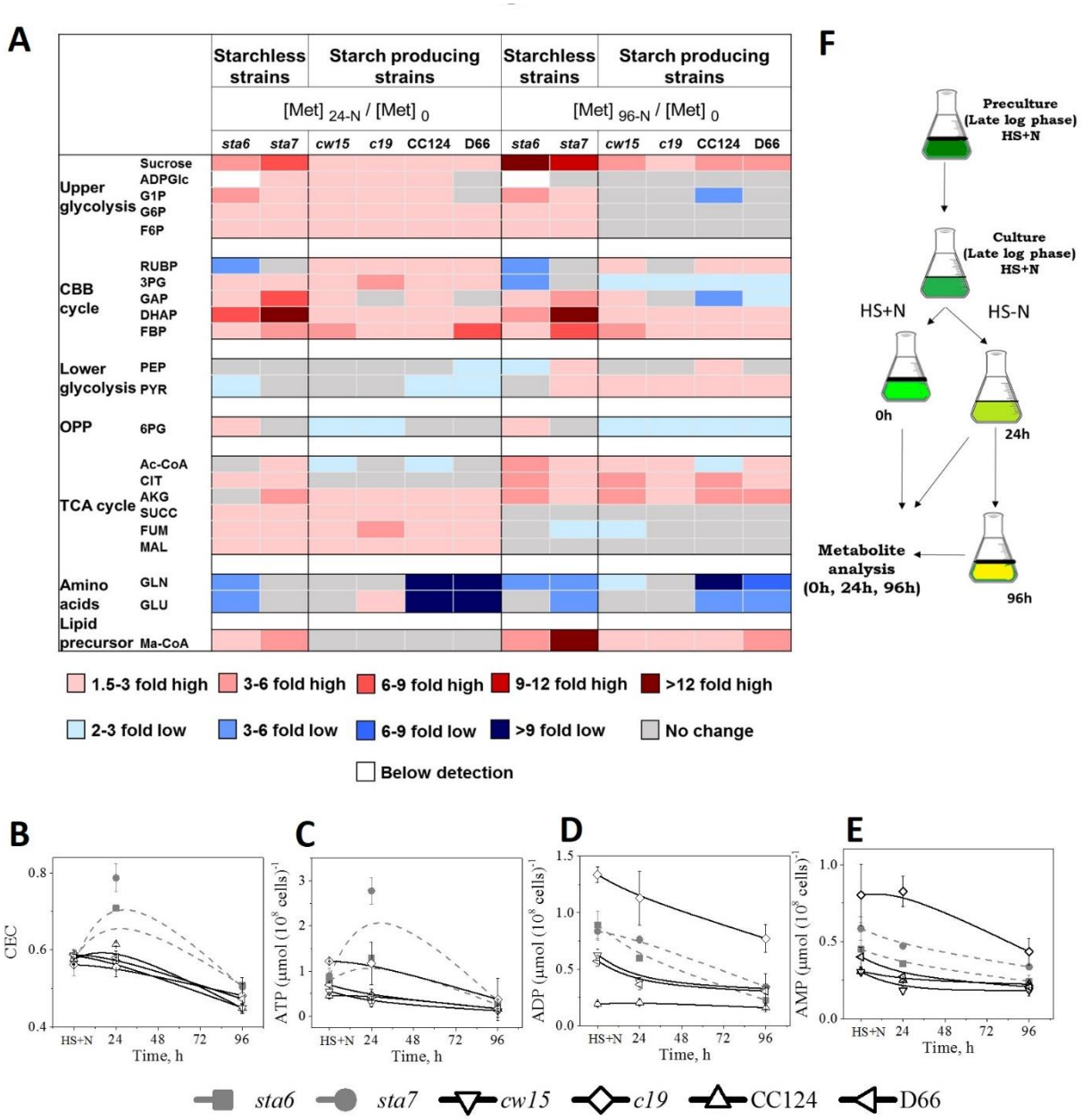

Figure 3-4 **Metabolite concentration changes at two time points following transfer of cells to N-free or to fresh N-replete media**. A) Heat map showing the ratio of metabolite concentrations [N-free/N-replete] after 24h (first 6 columns) and 96h (last 6 columns) of nitrogen starvation. Metabolite pool sizes are given in Table 3-1. Panels B) C) D) and E) give changes in cellular energy charge (CEC), ATP, ADP, and AMP content at each time point during nitrogen starvation. Values are the average of 3 measurements ± SE. Panel F) is a schematic represention of the experimental set up.

Pathway	**Metabolites**		Concentration (μmol /10^8 cells)												
			Time	*sta6*		*sta7*		CC124		*cw15*		*c19*		D66	
				Avg	SE	*Avg*	SE	*Avg*	SE	*Avg*	SE	*Avg*	SE	*Avg*	SE
Gluconeogenesis	**Glucose-1-Phosphate**	**G1P**	0	0.208	0.016	0.567	0.013	0.944	0.077	0.578	0.095	0.726	0.024	0.414	0.063
			24-N	0.378	0.051	1.454	0.109	1.587	0.145	1.022	0.122	1.192	0.189	0.614	0.019
			96-N	0.337	0.082	1.252	0.086	0.295	0.241	0.361	0.241	0.703	0.072	0.492	0.157
	Glucose-6-Phosphate	**G6P**	0	0.198	0.012	0.576	0.031	0.950	0.061	0.681	0.118	0.828	0.069	0.424	0.061
			24-N	0.325	0.069	1.501	0.002	1.534	0.115	1.097	0.144	1.416	0.202	0.730	0.009
			96-N	0.380	0.053	1.247	0.122	0.804	0.143	0.710	0.009	0.872	0.179	0.395	0.139
	Fructose-6-Phosphate	**F6P**	0	0.088	0.009	0.289	0.011	0.451	0.045	0.306	0.058	0.448	0.035	0.214	0.039
			24-N	0.164	0.040	0.684	0.049	0.834	0.036	0.584	0.066	0.734	0.093	0.475	0.011
			96-N	0.190	0.033	0.569	0.004	0.470	0.094	0.416	0.001	0.273	0.035	0.255	0.087
CBB cycle	**Ribulose bisphosphate**	**RUBP**	0	0.218	0.028	0.227	0.012	0.412	0.088	0.356	0.038	0.412	0.107	0.511	0.124
			24-N	0.069	0.036	0.215	0.026	0.897	0.091	0.644	0.109	0.745	0.100	1.007	0.031
			96-N	0.061	0.002	0.309	0.030	0.653	0.197	0.832	0.184	0.630	0.081	1.098	0.324
	3 Phosphoglycerate	**3PG**	0	0.526	0.023	0.493	0.121	0.404	0.030	1.583	0.164	0.711	0.297	0.237	0.033
			24-N	0.850	0.190	1.086	0.041	0.808	0.120	3.200	0.178	2.290	0.825	0.370	0.016
			96-N	0.104	0.005	0.532	0.291	0.201	0.176	0.655	0.061	0.426	0.051	0.097	0.074
			0	0.026	0.005	0.302	0.019	1.155	0.239	0.637	0.064	0.883	0.024	0.494	0.097

	Dihydroxy acetone phosphate	**DHA P**	24-N	0.196	0.044	3.824	0.264	2.496	0.182	1.352	0.259	2.606	0.382	1.384	0.100
			96-N	0.110	0.047	5.572	0.236	1.841	0.093	1.666	0.054	1.555	0.107	0.858	0.093
	Fructose Bisphosphate	**FBP**	0	0.019	0.001	0.037	0.016	0.716	0.072	0.134	0.009	0.219	0.057	0.327	0.046
			24-N	0.035	0.003	0.205	0.038	1.229	0.127	0.453	0.046	0.573	0.237	2.301	0.577
			96-N	0.034	0.012	0.309	0.051	1.199	0.274	0.725	0.035	0.410	0.048	0.611	0.090
	Glyceraldehyde 3 phosphate	**GAP**	0	0.000	0.000	0.002	0.000	0.007	0.002	0.004	0.000	0.004	0.000	0.004	0.001
			24-N	0.001	0.000	0.015	0.002	0.011	0.002	0.007	0.001	0.005	0.003	0.005	0.001
			96-N	0.001	0.000	0.008	0.001	0.012	0.000	0.006	0.002	0.005	0.000	0.005	0.001
Lower glycolysis	**Phosphoenol pyruvate**	**PEP**	0	0.067	0.007	0.053	0.011	0.068	0.005	0.203	0.028	0.215	0.046	0.026	0.005
			24-N	0.042	0.015	0.052	0.006	0.052	0.011	0.153	0.034	0.135	0.075	0.014	0.004
			96-N	0.023	0.068	0.095	0.036	0.129	0.046	0.133	0.093	0.138	0.007	0.015	0.016
	Pyruvate	**PYR**	0	0.347	0.105	0.573	0.101	0.549	0.133	0.521	0.068	0.802	0.099	0.217	0.038
			24-N	0.124	0.152	0.681	0.200	0.260	0.160	0.454	0.101	0.655	0.193	0.113	0.207
			96-N	0.297	0.333	1.294	0.484	1.263	0.010	0.989	0.068	1.620	0.247	0.647	0.253
TCA cycle	**Acetyl-CoA**	**Ac-CoA**	0	0.011	0.019	0.058	0.005	0.029	0.007	0.023	0.002	0.112	0.016	0.009	0.001
			24-N	0.013	0.001	0.094	0.004	0.014	0.000	0.012	0.002	0.122	0.040	0.010	0.002
			96-N	0.043	0.015	0.150	0.023	0.017	0.001	0.037	0.000	0.209	0.017	0.015	0.001
	Citrate	**CIT**	0	0.015	0.019	0.024	0.002	0.016	0.003	0.029	0.000	0.050	0.008	0.015	0.002
			24-N	0.024	0.021	0.043	0.004	0.018	0.065	0.028	0.001	0.056	0.027	0.020	0.008

			96-N	0.064	0.009	0.041	0.007	0.073	0.026	0.124	0.010	0.103	0.024	0.040	0.007
	α-ketoglutarate	**AKG**	0	0.031	0.003	0.150	0.017	0.064	0.005	0.021	0.003	0.258	0.002	0.238	0.009
			24-N	0.044	0.004	0.520	0.103	0.109	0.819	0.026	0.002	0.463	0.040	0.458	0.135
			96-N	0.145	0.014	0.275	0.023	0.196	0.135	0.143	0.030	0.502	0.024	0.907	0.266
	Succinate	**SUCC**	0	0.094	0.011	0.282	0.036	0.219	0.069	0.100	0.010	0.441	0.013	0.050	0.003
			24-N	0.192	0.001	0.458	0.069	0.394	0.017	0.216	0.030	0.830	0.089	0.107	0.005
			96-N	0.082	0.020	0.239	0.054	0.192	0.037	0.141	0.028	0.493	0.070	0.071	0.006
	Fumarate	**FUM**	0	0.334	0.037	0.380	0.026	0.558	0.096	0.508	0.055	0.260	0.018	0.270	0.047
			24-N	0.618	0.055	1.131	0.274	0.935	0.105	0.917	0.107	0.841	0.139	0.670	0.016
			96-N	0.230	0.041	0.211	0.211	0.605	0.157	0.231	0.189	0.337	0.162	0.271	0.170
	Malate	**MAL**	0	0.188	0.011	0.724	0.113	0.743	0.125	0.309	0.023	0.823	0.089	0.344	0.045
			24-N	0.357	0.021	1.758	0.157	1.167	0.152	0.552	0.060	1.786	0.297	0.857	0.054
			96-N	0.150	0.057	0.950	0.074	0.811	0.181	0.228	0.029	1.162	0.177	0.486	0.194
	Glutamine	**GLN**	0	0.082	0.010	0.027	0.006	0.050	0.003	0.030	0.006	0.021	0.001	0.063	0.022
Others			24-N	0.015	0.002	0.026	0.011	0.002	0.001	0.025	0.005	0.025	0.016	0.003	0.000
			96-N	0.019	0.000	0.006	0.000	0.004	0.000	0.012	0.000	0.020	0.002	0.008	0.001
	Glutamate	**GLU**	0	0.846	0.096	3.695	0.224	2.133	0.341	0.992	0.113	3.919	0.224	1.317	0.140
			24-N	0.250	0.016	4.499	0.527	0.062	0.037	0.928	0.153	6.141	0.793	0.026	0.014
			96-N	0.547	0.175	1.159	0.085	0.375	0.265	1.417	0.163	3.204	0.548	0.277	0.102

	Malonyl-CoA	**Ma-CoA**	0	0.007	0.001	0.002	0.000	0.001	0.003	0.001	0.000	0.005	0.003	0.001	0.000
			24-N	0.013	0.000	0.007	0.002	0.001	0.000	0.001	0.000	0.003	0.010	0.001	0.000
			96-N	0.033	0.000	0.053	0.003	0.001	0.000	0.001	0.000	0.008	0.003	0.002	0.001
	Sucrose	**SUCR**	0	0.004	0.002	0.003	0.001	0.028	0.004	0.002	0.001	0.007	0.003	0.012	0.005
			24-N	0.011	0.007	0.021	0.005	0.079	0.006	0.004	0.001	0.017	0.007	0.024	0.003
			96-N	0.046	0.016	0.034	0.019	0.100	0.005	0.011	0.002	0.018	0.002	0.062	0.036
Adenylates	**AMP**	**AMP**	0	0.450	0.173	0.585	0.077	0.309	0.013	0.303	0.014	0.803	0.197	0.401	0.064
			24-N	0.356	0.017	0.472	0.017	0.251	0.010	0.184	0.024	0.826	0.098	0.273	0.030
			96-N	0.243	0.040	0.337	0.012	0.224	0.005	0.185	0.036	0.434	0.086	0.207	0.029
	ADP	**ADP**	0	0.893	0.119	0.836	0.082	0.191	0.023	0.625	0.050	1.335	0.069	0.572	0.047
			24-N	0.597	0.005	0.762	0.031	0.207	0.025	0.388	0.039	1.129	0.238	0.364	0.043
			96-N	0.226	0.102	0.345	0.010	0.160	0.017	0.328	0.134	0.772	0.123	0.306	0.027
	ATP	**ATP**	0	0.790	0.057	0.899	0.169	0.457	0.064	0.558	0.041	1.219	0.005	0.694	0.053
			24-N	1.292	0.012	2.776	0.290	0.462	0.017	0.302	0.095	1.172	0.466	0.448	0.161
			96-N	0.254	0.013	0.344	0.045	0.168	0.058	0.121	0.044	0.375	0.469	0.170	0.191

Table 3-1: **LC-MS/MS results for various metabolites**. Standard error of mean are represented in columns adjacent to the average metabolite concentration calculated as μmoles per 10^8 cells.

Metabolic response to N starvation in starch containing strains:

In the absence of N, cellular levels of glutamate and glutamine decreased (1-50 fold) indicating the inability of the strains to synthesize nitrogenous compounds (Fig. 3-4 A). Within the first 24 h of nitrogen starvation, the pool sizes of several metabolites increased and then subsequently decreased back to the T_0 levels at 96 h, indicating a dynamic remodeling of metabolism over the course of N starvation (Fig. 3-4 A). Most metabolites of the TCA cycle increased by 1.5-3.5 fold within the first 24 h, except for citrate and acetyl-CoA. However, at 96 h, fumarate, succinate and malate decrease back to T_0 levels or lower while the α-ketoglutarate (AKG) and citrate (CIT) remained higher (2-5 fold higher than T_0). The inverse behavior between CIT-AKG and the rest of the TCA cycle metabolites suggest a slower conversion of AKG into succinate or a very high influx of carbon into AKG derived from either the deamination of glutamic acid by glutamate dehydrogenase or from newly fixed carbon entering the TCA cycle. Nonetheless, the high accumulation of CIT and AKG indicates a kinetic bottleneck at AKG.

Metabolites corresponding to upper gluconeogenesis, G1P, G6P and F6P, increased by 1.5-3 fold at 24 h and then decreased back to T_0 levels at 96 h of nitrogen starvation (Fig. 3-4 A). This increase correlates with an increase in the production of sucrose (albeit at low concentrations) at both 24 h and 96 h after N starvation, confirming the increased flux through gluconeogenesis. Contrary to the upper glycolytic intermediates, metabolites of lower glycolysis that lead to AcCoA and to the fatty-acid precursor MaCoA did not show any significant difference in the first 24 h. However, both AcCoA and MaCoA increased appreciably at 96 h of nitrogen starvation, indicating a major change in carbon allocation toward fatty acid synthesis following a 24 h lag.

The total adenylate nucleotides were also quantified at each of the time points and the cellular energy charge (CEC) was calculated (Fig 3-4 B-E). Overall, both CEC and the adenylates tend to decrease during the nitrogen starvation period across all the starch containing strains.

Metabolic response to nitrogen starvation in starchless mutant strains:

A main aim of these experiments is to identify the underlying metabolic changes to account for the higher lipid fraction in the starchless mutant strains. At 24 h of N starvation, a select few metabolites displayed different concentration profiles between starch producing and starchless mutant strains (Fig. 3-4 A). At 24 h, AcCoA and MaCoA increase (1.6-fold and 1.5-3-fold higher, respectively) in both *sta6* and *sta7* strains (Fig. 3-4 A), indicating an earlier onset of fatty acid biosynthesis in these mutants. Even though starch biosynthesis is blocked in both these mutants, the pool sizes of several upper gluconeogenic intermediates (G1P, G6P, F6P) and sucrose increase at 24 h and do not diminish at 96 h (Fig. 3-4 A). The starchless mutant strains also show an increased CEC at 24 h (unlike the starch containing strains) caused by an increase in the total ATP content at this time point (Fig. 3-4 B-E). These results indicate that in the absence of starch synthesis, carbon accumulates as intermediates of gluconeogenesis and excess ATP is not utilized.

The two-point timeline of metabolite concentrations (Fig. 3-4 A) suggests a temporal separation of the central carbon pathways leading to starch, and both lipids and amino acid precursors. In all of the starch synthesizing strains, there is an earlier allocation of carbon into gluconeogenesis, followed by intermediates of lipid synthesis (AcCoA, MaCoA) and the upper TCA cycle intermediates involved in amino acid synthesis (AcCoA, CIT, AKG). By contrast, in the starchless mutant strains, carbon allocation to all three pathways appears simultaneously within the limited time resolution.

We undertook a more detailed time course in two representative strains, *sta6* and *cw15*. These strains were chosen as additional literature on their transcriptomic response under nitrogen starvation is available (Blaby *et al.*, 2013), (Goodenough *et al.*, 2014). Samples were taken at intervals of 3, 6, 10, 24, 31, 48, 72 and 96 h post nitrogen starvation (Fig. 3-5 A-E). The experimental setup is schematically represented in Fig. 3-5 F.

Figure 4

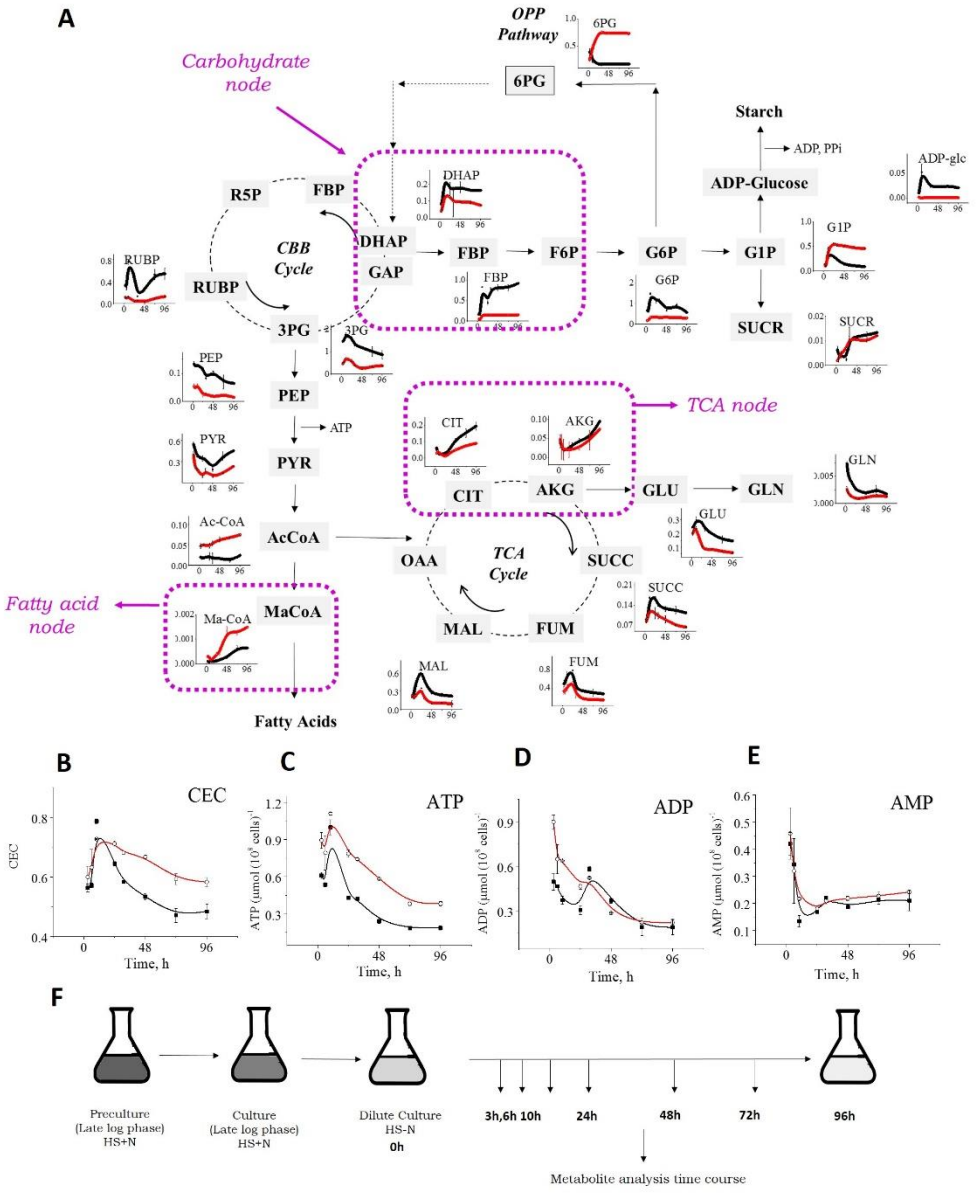

Figure 3-5 **Time resolved metabolite change.** A) Time course of the steady-state changes of metabolite concentrations following initiation of nitrogen starvation through 96 h. Two cell lines are shown *sta6* (red) and *cw15* (black). The pathways of central carbon metabolism are depicted and key nodes are highlighted where flux changes are prominent. Concentrations of three adenylate energy metabolites and CEC are listed. The Y axis units are μmol $(10^6$ cells$)^{-1}$. Values are the average of 3 measurements ± SE. B) Schematic representation of the experimental set up for the time resolved metabolic analysis.

Time-resolved carbon partitioning in control strain *cw15* after N starvation:

Gluconeogenesis: The first 10 h of nitrogen starvation acts as a preparatory phase, where the upper glycolytic metabolite levels increase in concentration, especially 3PG, DHAP, FBP, G6P, G1P and ADP-glucose (Fig. 3-5 A). Post 10 h, the gluconeogenic intermediates G6P, G1P and ADP-glucose start to decrease while, DHAP and FBP levels remain high. These results, taken together with high TRC content at both 24 h and 96 h (Fig. 3-3) indicate a sustained feeding of carbon into the gluconeogenic route via DHAP and FBP with a simultaneous drain of G6P into starch. As DHAP and FBP show a very different trend than both the preceding (3PG) and succeeding metabolites (G1P) (Fig. 3-5 A), we suggest that this junction is key to controlling carbon allocation to starch. We call this the 'Carbohydrate Node' and label it as such in Fig 3-5 A.

TCA cycle: Parallel to the increase in the gluconeogenic intermediates, there is also an initial increase in the TCA cycle metabolites, especially succinate, malate and fumarate while AKG and citrate decrease in concentration (Fig. 3-5 A). This occurs in coordination with a slight increase in protein content at 24 h (Fig. 3-3 B). Post 24 h, AKG and citrate start to accumulate, while succinate, malate and fumarate decrease. In addition, both glutamate and glutamine - products derived from AKG - show a large decreasing trend. Collectively, these temporally coordinated changes in metabolites indicate that the metabolic switch away from protein biosynthesis occurs at the level of CIT/AKG. This observation (Fig. 3-5 A) is in parallel to the results observed in Fig. 3-4 A. Henceforth, we call CIT-AKG node as the 'TCA cycle node' controlling carbon redirection.

Lipid metabolites: In parallel with the continuous accumulation of AKG over 96 h, the concentration of the FA precursors AcCoA and MaCoA increase continuously after a lag of 31 h following N starvation (Fig. 3-5 A). The concentration rise of MaCoA is particularly large reaching 12 fold increase. The lag time clearly shows the temporal separation of carbon allocation initially into carbohydrates/starch biosynthesis followed by build up of precursors to FA synthesis. To

emphasize this key metabolic control point, we highlight MaCoA as the 'FA node' in Figure 3-5 A.

Adenylate nucleotides: At the start of N starvation, there is an immediate increase in the level of ATP and CEC. The ATP and CEC levels then decrease (Fig. 3-5 B-E) in parallel with the consumption of the gluconeogenic precursors, G1P and G6P, eventually after 24-36 h dropping below the initial levels. The time resolved measurements give a better resolution of the changes in the in the coarse measurements. The results show that even the starch containing strains show an initial increase in the CEC levels till 10h (not seen in the coarse profiling) after which the CEC levels start to drop (seen in coarse profiling). Thus the time resolved measurements allow us to gain more resolved data that was not observed in the coarse profiling. Overall at the end of 96h of N starvation, the total adenylate nucleotide pool size decreased, reflecting the quantitative impact of N starvation on adenylate energy.

Time-resolved metabolic changes in the starchless mutant *sta6*:

Higher time resolution studies (Fig. 3-5) reveal that within the first 10 h of N starvation, *sta6* starts from a lower initial level of gluconeogenic intermediates (FBP and G6P) which then barely increase compared to their levels in the control strain *cw15*. On the other hand, significant accumulation of G1P and 6PG is observed. As it is previously established that the irreversible step in gluconeogenesis of green algae is the hydrolysis reaction of FBP to F6P and inorganic phosphate (Huppe *et al.*, 1989), the very low levels of the downstream metabolite G6P and high levels of G1P, indicates that it must be consumed by downstream reactions other than starch formation. The second difference observed is an earlier increase in both AcCoA and MaCoA levels; MaCoA starts to rise sharply at 24 h and reaches a higher level in *sta6* compared to onset at 31 h in *cw15* (Fig. 3-5 A). This indicates an earlier entry and greater accumulation of carbon at the 'FA node' in *sta6.* The onset and subsequent plateau of accumulation of malonyl-CoA occurs at the same time as corresponding changes occur in the concentration of G1P, the immediate precursor to starch

biosynthesis (Fig. 3-5). This suggests that in the starchless mutant blocking of the carbon flux into the TCA cycle at AKG/GLU due to N starvation leads to carbon allocation into FA biosynthesis pathway.

Similar to the starch synthesizing strains, *sta6* also shows an initial increase in both the ATP content and the CEC levels by *ca.* 60%, followed by recovery to even lower levels at 96 h. However, unlike *cw15*, both ATP and CEC are sustained at higher levels throughout the course of N starvation in *sta6* (Fig. 3-5). Thus, cells of the starchless mutant have an excess of adenylate energy relative to the control strain, which can potentially lead to greater inhibition of many enzymes involved in energy metabolism.

3.3) Carbon redirection away from starch occurs at the level of G6P in the sta6 strain.

To test how the loss of starch polymerization affects the flux through gluconeogenesis, we performed ^{13}C kinetic labeling experiment using LC-MS to determine the first order rate constant of the metabolites in *cw15* and *sta6*, using ^{13}C-$NaH^{13}CO_3$ to follow formation of ^{13}C-labeled metabolites. This was done in the presence and absence of N. As significant differences in carbon allocation into the metabolic pathways were observed at 24 h of N starvation (Figs. 3-4 and 3-5), this time point was chosen to inject 10 mM ^{13}C-sodium bicarbonate (100%), followed by sampling at 0.5, 1, 2, 4, 15 and 30 min to assess metabolite turnover (Fig. 3-6 B). To mimic the results from the time resolved metabolite analysis, samples resuspended in HS+N medium were used as the control for ^{13}C analysis while for HS-N analysis, samples were grown in HS-N medium for 24 h. The choice of 3h for the HS+N analysis is described in the methods section (See Materials and Methods). The ratio of ^{13}C to the total carbon in each metabolite was calculated from the mass isotopomer distributions (See Materials and Methods). Fig. 3-6 A gives the concentration of ^{13}C-labeled metabolites compared under +N and -N conditions. From this one can extract the rate of formation of labeled metabolite and the fraction of the total metabolite pool that is labeled. The initial slope of the ^{13}C -fraction versus time has been used as an estimate of the initial formation

rate of the metabolite via biosynthetic pathways (Hasunuma *et al.*, 2010), (Yang *et al.*, 2013). Fig. 3-7 gives the fitted initial slopes for both *sta6* and *cw15* under N replete and deplete conditions.

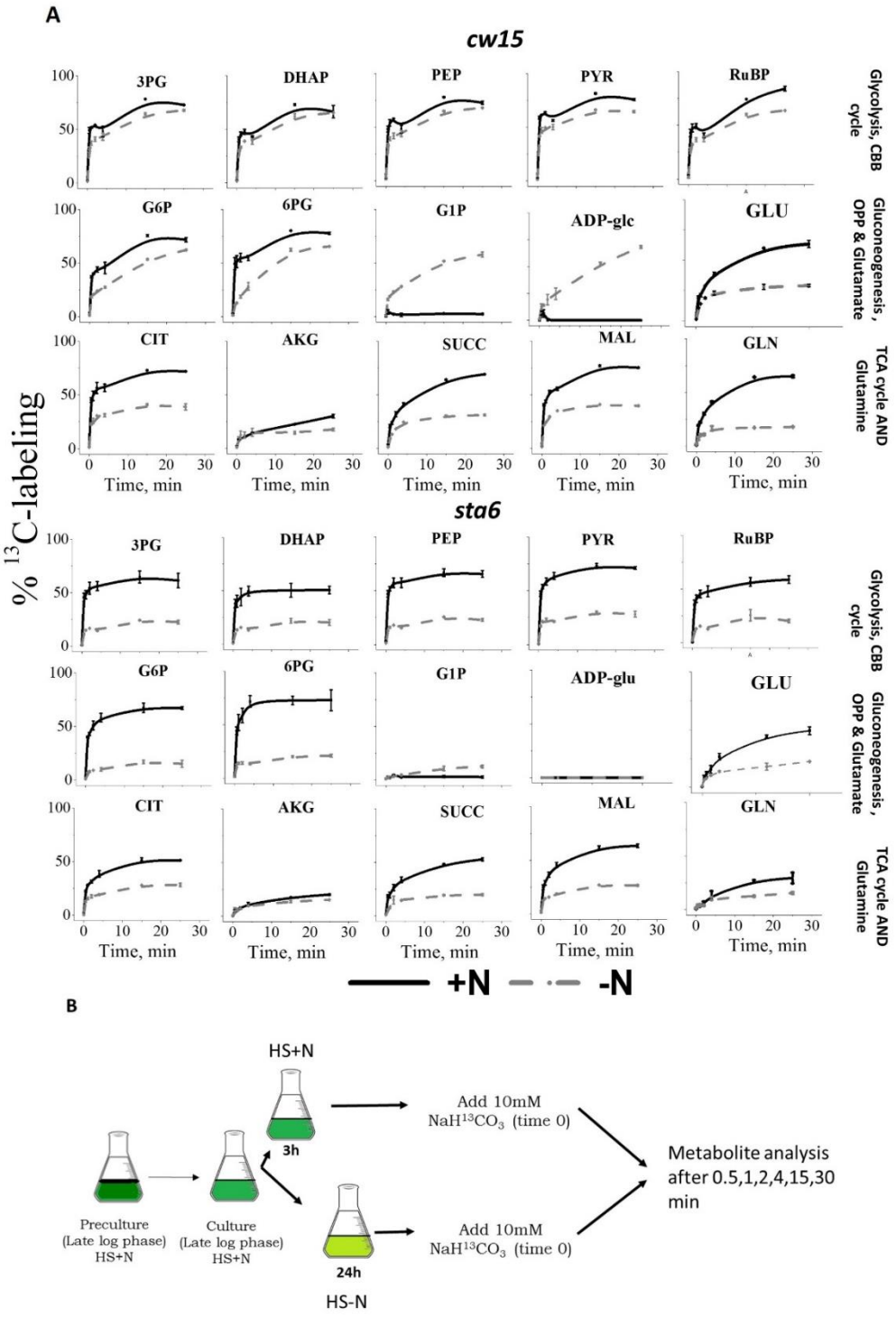

Figure 3-6 **13C analysis of N starvation.** Time course of formation of ^{13}C metabolites in intact cells of *cw15* and *sta6*, following transfer to N-replete media (solid black) and N-free media (grey dash). Y axis represents fraction of ^{13}C labeled metabolite. Values are the average of 2 measurements, ± SE. B) Schematic of the procedure for ^{13}C-labeling from $NaH^{13}CO_2$.

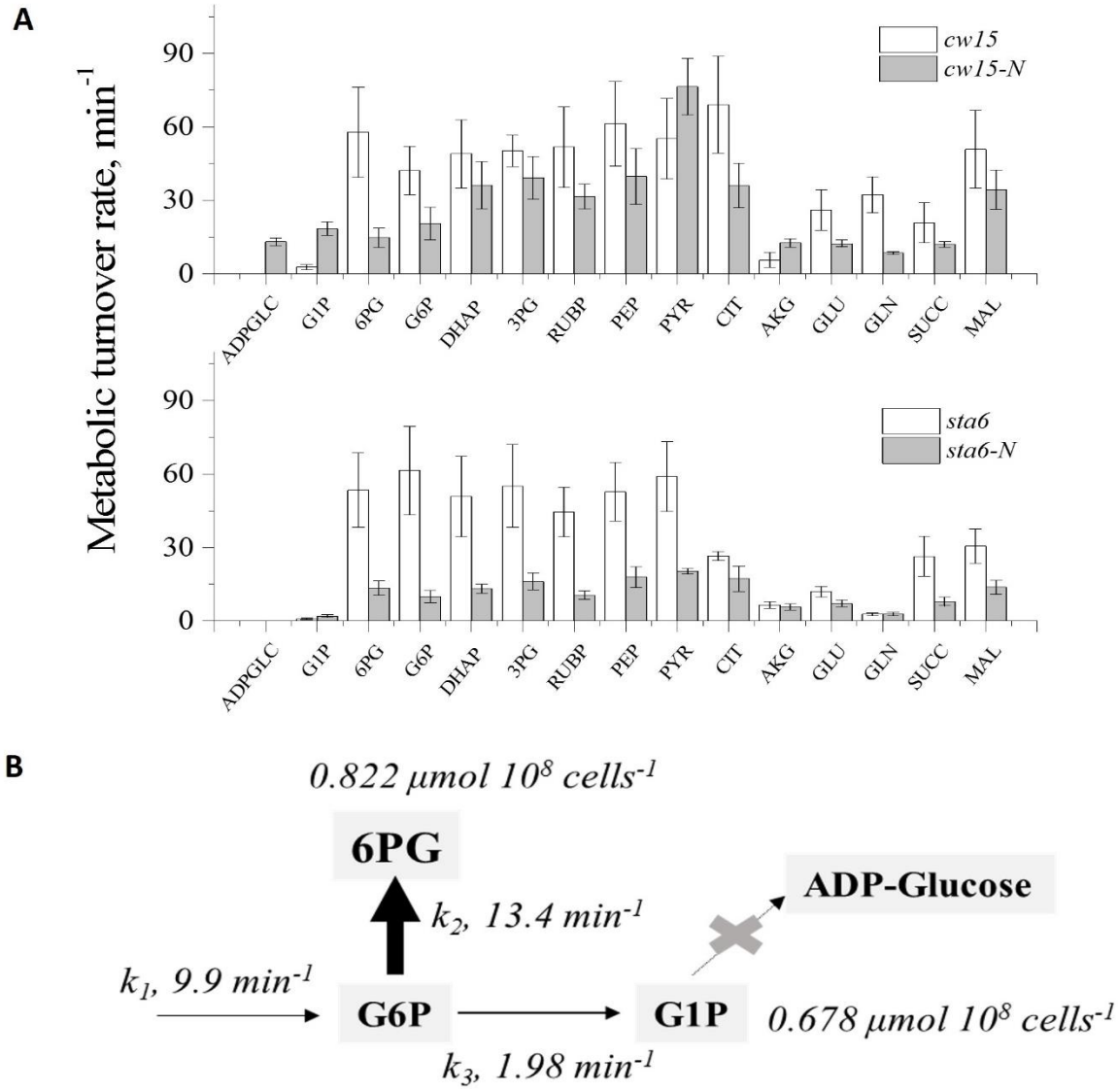

Figure 3-7 **Initial rate of formation of the metabolite.** The initial formation rate (min^{-1}) of ^{13}C-metabolites in C. reinhardtii following injection of $NaH^{13}CO_3$ (10 mM) with N-replete media (white bars) or without nitrogen (grey bars, -N). The rate is calculated by fitting the initial labelled fraction (0 min-2 min) to a straight line. Values are the averages of 2 biological replicates ± S.E. Top panel is for *cw15* and the bottom panel is for *sta6*. B) Carbon partitioning at G6P under N starvation condition. Turnover rates from Fig. 6A and the pool sizes from Table 3-1 for 6PG and G1P are presented.

Fig. 3-7 A shows that the most rapidly labeled metabolites in both *cw15* and *sta6* under nitrogen replete (+N) conditions (PYR, PEP, 3PG) are not confined to the Calvin cycle, although the first Calvin cycle product, 3PG, is among the fastest labelled metabolites. This outcome indicates that other CO_2/HCO_3^- reduction sites must contribute to the rapid labeling across so many diverse metabolites. *C. reinhardtii* has two other CO_2/HCO_3^- utilizing enzymes, pyruvate synthase ($AcCoA + 2Fd_{red} + CO_2 + 2H^+ \leftrightarrow PYR + 2Fd_{ox} + CoA$) and PEP carboxylase ($PEP + HCO_3^- \leftrightarrow OAA + Pi$) (Chen *et al.*, 1971), that function to restore metabolites that are consumed during biosynthesis. These anaplerotic reactions are required for proper functioning of the TCA cycle under normal conditions. Their possible contribution during –N nutrient stress is indicated. Pyruvate synthase requires high reductant poise (Fd_{red}), while PEP carboxylase is active only at high CEC, thus limiting both reactions to these special conditions. The slower labeling of metabolites such as DHAP and AKG than their downstream metabolites indicates the presence of subcellular compartmentation or enzymatic channeling of these metabolites (Yuan *et al.*, 2008). The kinetic data in Fig. 3-6 also reveals that in *cw15* significant labeling of G1P and ADP-glucose was only observed under –N conditions, consistent with significant accumulation of total reducing carbohydrate under these conditions *in cw15*.

For both *sta6* and *cw15*, N starvation lowers the maximum ^{13}C enrichment and the metabolite turnover rates (Fig. 3-6, 3-7 A) for all the measured metabolites (except G1P, ADP-glucose and PYR). Especially in *sta6*, the maximum ^{13}C enrichment of 3PG is reduced by more than 2-fold, indicating a significant reduction in carbon fixation upon N starvation. However, in both the strains, the turnover rates of the sugar phosphates remain at par with 3PG (except G1P in *sta6*). This indicates that irrespective of ability/inability to synthesize starch, the turnover of the sugar phosphates leading to G6P remains high.

In *cw15*, G1P turns over at rates significantly higher under –N than under +N conditions (Fig. 3-7 A). Even though in *sta6*, the kinetics of G6P labeling are at par with the 3PG labeling

rate, the turnover rates for G1P do not increase significantly under –N conditions. This indicates a redirection of carbon flux into G6P. G6P can be converted to either G1P or 6PG, depending on relative activities of the enzymes phosphoglucomutase or glucose-6 phosphate dehydrogenase, respectively. 6PG is an intermediate that occurs in the oxidative pentose phosphate (OPP) pathway or the Entner–Doudoroff (ED) pathway. As *Chlamydomonas* lacks the genes for the ED pathway, we attribute the labeling of 6PG to flux through the OPP pathway. Flux through a metabolite is calculated by multiplying the metabolite turnover rate and its pool size. Since G6P is the only ^{13}C labeled precursor to synthesize G1P or 6PG, the enrichment kinetics and pool sizes of both can be used quantitatively to compare the fluxes between the two metabolites. Both the metabolite pool size and the metabolic turnover rate for 6PG are larger as compared to the pool size and the metabolic turnover rate for G1P (Fig. 3-7 B), indicating a faster carbon influx from G6P into 6PG than into G1P for the *sta6* mutant.

We conclude that in *sta6,* under N starvation a greater fraction of the flux is diverted through the OPP. Activation of the OPP pathway converts G6P to GAP + 3 CO_2 + 3 NADPH, which in turn delivers additional GAP through lower glycolysis to make AcCoA and MaCoA, the carbon precursors to fatty acids. The OPP pathway generates three times more NADPH than does glycolysis, which is the essential nucleotide cofactor needed to power anabolic reactions, including fatty acid biosynthesis. To test this prediction, we investigated the intrinsic fluorescence emission from NAD(P)H to estimate the relative concentrations of NAD(P)H and $NAD(P)^+$, using a previously developed protocol and homebuilt fluorometer (Krishnan *et al.*, 2015).

3.4) NADPH measurements:

Figure 3-8 shows the intensity of fluorescence emission at 420 ∓10 nm from intact cells excited by weak light at 365 nm) following different durations of N starvation from 0 to 96 h. Emission intensity is proportional to the concentration of reduced pyridine nucleotides. Samples were concentrated to the same pyridine nucleotide concentration (0.25 μmol ml^{-1}). For this the total pool

size of ($NADP^+$+ NADPH) was measured at the each time point using LC-MS. The NADPH fluorescence time profile shows an illumination cycle of dark–light–dark induction transients produced by saturating red light (660 nm, Intensity =400 μE m^{-2} s^{-1}) which photoreduces $NADP^+$ via Photosystem I excitation. The light induced increase provides a direct measure of the relative amount of $NADP^+$ availability in the dark prior to illumination.

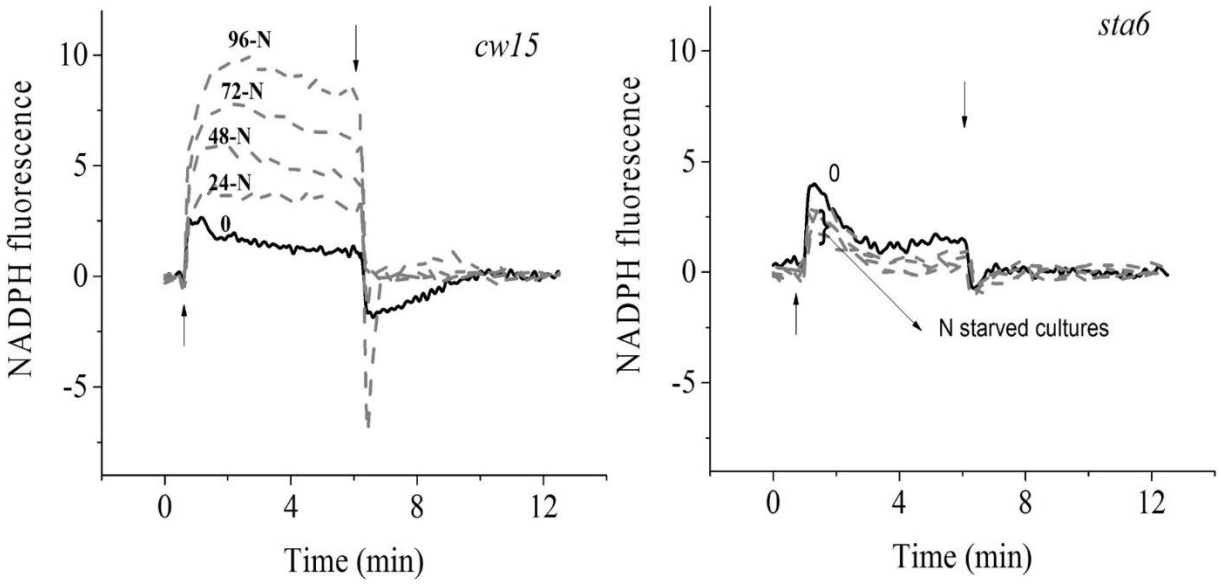

Figure 3-8 **Kinetics of NADPH fluorescence induction**. Intensity of fluorescence emission at wavelength 420 ∓10 nm from *Chlamydomonas reinhardtii* cells following different durations of N starvation from 0 to 96 h. Emission intensity is proportional to the concentration of reduced pyridine nucleotides, NAD(P)H (weak excitation at 365 nm). The time profile shows an illumination cycle of dark–light–dark induction transients produced by saturating red light (660 nm, Intensity =400 µE m^{-2} s^{-1}). Light was turned on at points indicated by upward arrow and turned off at time point indicated by downward arrow. Samples were concentrated to a pyridine nucleotide ($NADP^+$+NADPH) concentration 0.25 µmol ml^{-1}.

The data show that *cw15* and *sta6* have comparable initial light-induced amplitudes prior to N starvation, indicating comparable $NADP^+$ concentrations in the dark. As N starvation develops in *cw15* the oxidized $NADP^+$ signal increases by *ca* 4 fold at 96h, while *sta6* shows much smaller changes that decrease oxidized $NADP^+$. The data indicate that N starvation causes a significant increase in the relative amount of oxidized $NADP^+$ in the control strain due to oxidation of NADPH, while *sta6* is incapable of draining its reduced NADPH pool or has a higher activity of light independent pathways that reduce the oxidized $NADP^+$ pool (for example OPP).

4. Discussion

Pathway of carbon assimilation and the carbon redirection nodes under N starvation: Multiple starchless mutant strains showing enhanced lipid accumulation under N starvation condition have been generated and extensively investigated in the green microalga *C. reinhardtii* (Work *et al.*, 2010); (Blaby *et al.*, 2013); (Goodenough *et al.*, 2014); (Wang *et al.*, 2009); (Goodson *et al.*, 2011); (Siaut *et al.*, 2011); (Breuer *et al.*, 2014); (Li *et al.*, 2010); (Miller *et al.*, 2010). Herein we used time-resolved metabolite profiling as a tool to identify how two such strains (*sta6* and *sta7*) partition photosynthetically fixed carbon away from starch into lipids during N starvation. Scheme 3-1 gives a representation of the global metabolism occurring in the starchless and the starch synthesizing strains as a response to N starvation.

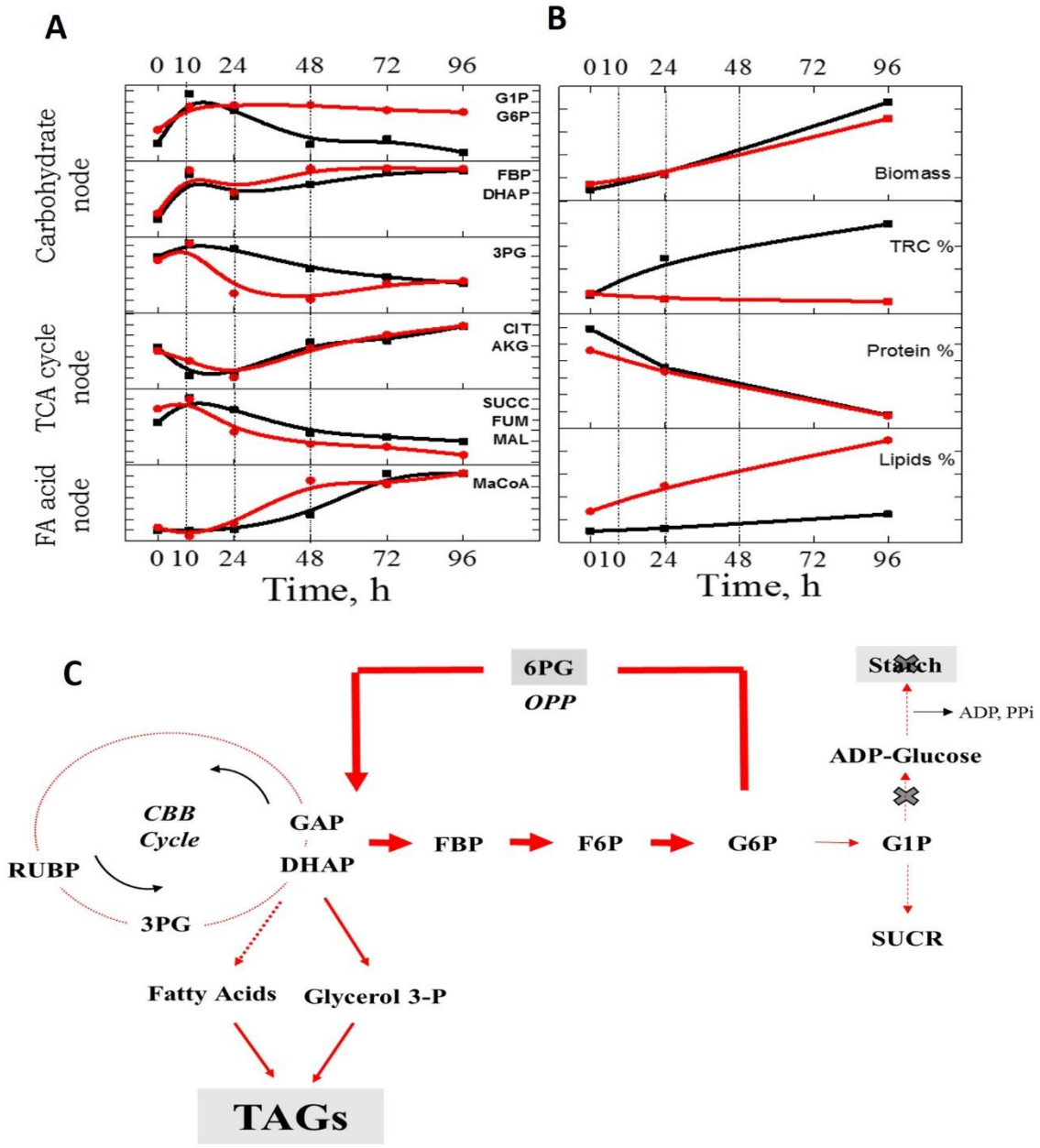

Scheme 3-1 **Global metabolic consequences of nitrogen starvation (–N) for two strains** as seen by: (A) steady-state concentration changes in key metabolic nodes. To generalize the metabolite trends and report the relative changes in the metabolite levels occurring during N starvation, the highest concentration reached by the metabolite was taken as 100% and the rest of the time points were normalized to this highest value. (B) Changes in downstream terminal product yields, and (C) transient flux changes in major metabolic pathways after 24 h of N starvation, as measured by ^{13}C-labeling. Black lines represent *cw15*, red lines represent *sta6*. In (C) the major flux change in sta6 through the oxidative pentose phosphate pathway is shown by thicknesses of arrows to represent large and small fluxes through the metabolites, dashed arrows represent fluxes that were not measured.

Time resolved profiling of metabolites shows that upon N starvation three metabolite nodes (flux choke points) exist whose steady-state concentrations change as N starvation develops, and are responsible for the changes in terminal products (proteins, carbohydrates and lipids): a) The Carbohydrate Node at GAP/FBP reports on the allocation of carbon between the upper and lower branches of the glycolytic/gluconeogenic pathways, which feeds into either starch or precursors to fatty acids and proteins; b) The TCA Node at CIT/AKG reports on metabolite fluxes to the biosynthesis of amino acids and from catabolism of proteins; and c) The Fatty Acid Node at Malonyl-CoA reports on metabolite fluxes to fatty acids and from catabolism.

We observe maintenance of gluconeogenic fluxes during N starvation even in mutants blocked at starch polymerization due by redirecting carbon into the OPP pathway via G6P, initially forming GAP and DHAP, and ultimately into fatty acid precursor (Mal-CoA) and a precursor to formation of both phospho-lipids and TAGs (glycerol-3-P) at the expense of the loss of fixed carbon as CO_2. This rerouting of fixed carbon through OPP generates the additional reductant (NADPH) necessary for biosynthesis of fatty acids, lipids and TAGS, thereby ensuring these soluble carbon metabolites are converted to more safely stored energy-rich fats.

Central carbon metabolism: Early in N starvation, there is an initial transient increase in many of the monitored metabolites (Fig. 3-5) and this acts as a preparatory phase needed to switch the metabolic pathways from protein synthesis to starch accumulation. The carbon allocation into lipids and starch are temporally separated (Fig. 3-4, Fig. 3-5) with gluconeogenesis preceding fatty acid (FA) biosynthesis (Fig. 3-3, Fig. 3-4, Scheme 3-1). Transcriptomic studies show a similar - temporal separation between the gluconeogenic and FA pathways (Blaby *et al.*, 2013) in *cw15* under N starvation.

Even in the absence of the ability to synthesize starch and during N starvation, gluconeogenesis occurs (Fig. 3-4, Fig. 3-5, Scheme 3-1) and the temporal separation between the gluconeogenic and the FA pathways is retained. However, the time period between the active

allocation of carbon into the two pathways is significantly reduced in both *sta6* and *sta7* (Fig. 3-4, Fig. 3-5, Scheme 3-1) as opposed to the control strains.

The 'Carbohydrate Node': DHAP and FBP metabolite levels were found to be sensitive reporters of flux changes at the junction of the CBB cycle and gluconeogenesis (Fig. 3-4, Scheme 3-1). On the downstream side, the irreversible hydrolysis reaction of FBP to F6P and inorganic phosphate is catalyzed by FBP phosphatase in green algae (Huppe *et al.*, 1989). The unidirectioinality of this reaction means it serves as the gatekeeper for formation of gluconeogenic products. On the downstream side, the greatly depressed levels of FBP and G6P in the starchless strain following N starvation implies FBPase is regulated "on" (its most active form) and these metabolites are being drained by the OPP pathway. This conclusion is confirmed by both the transient ^{13}C flux measurements and longer term steady-state concentration of 6PG (Figs. 3-5 and 3-6, respectively). On the supply side of this node, concentrations are governed by two reversible enzymes: triose phosphate isomerase (TPI) isomerizes GAP to DHAP, while fructose bisphosphate aldolase (FBA) generates FBP by an aldol condensation of GAP and DHAP. Not much is known about the regulation of TPI and FBA in *C. reinhardtii*. Interestingly, in the proteomic study by Schmollinger et al. (Schmollinger et al., 2014), TPI and FBA were the only CBB cycle proteins that increase in concentration upon N depletion (70% and 12% respectively), suggesting the importance of this node in directing carbon into gluconeogenesis products in the absence of N.

Pathway of carbon in starchless mutant strains: A major objective of our study was to understand how the starchless mutant strains direct a greater fraction of carbon towards TAGs under N depletion. Goodenough et al. (Goodenough *et al.*, 2014) had hypothesized a G6P backflow mechanism in *sta6*, wherein the G6P generated feeds into the plastid-localized OPP and lower glycolysis pathways to generate additional carbon and reductant necessary for TAG biosynthesis. This was proposed to occur under special conditions of "acetate boost" (Goodenough *et al.*, 2014).

Our results in *sta6* actually show the occurrence of the OPP pathway during N starvation and that this is not specific to "acetate boost" conditions. The pathway is shown in Scheme 3-1 C.

In response to N stress, the starchless mutant strains channel carbon through gluconeogenesis as a default response. The flux through both the gluconeogenic and the lower-glycolytic route remains high (Fig. 3-6, Fig. 3-7). However, in *sta6*, the carbon forming G6P gets funneled into 6PG at higher flux than G1P under –N conditions. Thus, the redirection of carbon in the starchless mutant strains occurs at the level of G6P (Fig. 3-7, Scheme 3-1). From here, the carbon cycles through the OPP pathway to generate GAP/DHAP that enters into lower glycolysis and into FA biosynthesis. Indeed, the formation of malonyl-CoA (FA node) in *sta6* has an earlier onset than in *cw15*. In addition, DHAP is also a substrate for the synthesis of the TAG backbone, glycerol 3-phosphate. Thus, the recycling of carbon via OPP generates both the precursors for the fatty acid chain, as well as the glycerol backbone of TAGs. We observe that under prolonged N starvation, *sta6* maintains a highly reduced pyridine nucleotide pool, consistent with our data demonstrating elevated OPP flux (~ 3x more reductant generated than glycolysis).

The gluconeogenic and CCB pathways shares a series of four reversible reactions involving 3PG, DHAP, GAP, FBP and F6P. Flux through gluconeogenesis may be necessary to replenish the CBB cycle intermediates and thus sustain carbon fixation. This may be a potential reason why the starchless mutant strains try to maintain a high flux through gluconeogenesis and recycle the fixed carbon through the OPP pathway. However, the use of the OPP pathway to redirect fixed carbon towards lipids has two disadvantages. For every molecule of G6P polymerized to starch one molecule of ATP is consumed to generate ADP-glucose. While the OPP pathway consumes a molecule of G6P by oxidative release of three CO_2 molecules and one 3 C molecule GAP with a net gain of six NADPH molecules (3G6P→F6P + G6P + GAP + 3 CO2 + 6 NADPH). Thus, while the OPP pathway generates the NADPH needed for FA biosynthesis, it also results in a significant loss in fixed CO_2 and does not regenerate or consume ATP. In addition to the lower

levels of photosynthetic carbon fixation (Fig. 3-6 A), the loss of already fixed carbon as CO_2 may be a contributing reason to the substantially lower levels of biomass accumulation in the starchless mutants upon nitrogen starvation (Fig. 3-3).

ATP regulation of gluconeogenesis: Reversible protein phosphorylation is known to play an important role in regulation of starch anabolism. Multiple enzymes including starch synthases, starch branching enzymes, phosphoglucose isomerase, AGPase (both small and large subunits) are targets for reversible protein phosphorylation (Tetlow et al., 2004; Tetlow et al., 2008; Grimaud et al., 2008; Heazlewood et al., 2008). The rise in ATP level that occurs before the conversion of gluconeogenic metabolites into starch (Fig. 3-43) may be essential to activate these enzymes and thus activate starch biosynthesis. In this aspect, the potential role of protein phosphorylation may be an important avenue to investigate to increase carbon allocation to desired sinks.

Chapter 4: Fermentative metabolism in the carbon concentrating mechanism repressor (*ccmR*) mutant of *Synechococcus* sp. PCC 7002

Anagha Krishnan[1], Shuyi Zhang[2], Yang Liu[2], Kinan A. Tadmori [1], Donald A. Bryant[2,3], G. Charles Dismukes[1,4]*

[1]Waksman Institute of Microbiology, Rutgers, the State University of New Jersey, Piscataway, NJ 08854. [2]Department of Biochemistry and Molecular Biology, The Pennsylvania State University, University Park, PA 16802, USA. [3]Department of Chemistry and Biochemistry, Montana State University, Bozeman, MT 59717 USA. [4]Department of Chemistry & Chemical Biology, Rutgers, the State University of New Jersey, Piscataway, NJ 08854.

Summary

CcmR, a LysR-type transcriptional regulator, represses the genes encoding components of the high-affinity carbon concentration mechanism in cyanobacteria. Unexpectedly, deletion of the *ccmR* gene was found to alter the expression of fermentative genes, especially the hydrogenase operon in the cyanobacterium *Synechococcus sp.* PCC 7002. To understand how CcmR influences fermentative metabolism, the kinetics of glycogen autofermentation were studied in *ccmR* deletion strains of *Synechococcus* 7002 following photoautotrophic growth. We quantified excreted metabolites and monitored the intracellular concentration of NAD(P)H by fluorescence. Inactivation of CcmR resulted in a 50% increase in H_2 production, while continuous removal of H_2 from the medium ("milking") to suppress uptake, boosted the yield by 2.6-fold (20 h) compared to the wild-type strain. Consistent with this greater reductant flux to H_2, the mutant excreted less lactate (NAD(P)H consuming pathway) during glycogen catabolism. To increase the glycolytic rate and conserve NADH, the *ccmR* mutant was further engineered to introduce GAPDH overexpression (more NADH production) and LDH deletion (less NADH consumption). The triple

mutant (*ccmR* deletion + GAPDH overexpression + LDH deletion) showed 6-8-fold greater H_2 yield than the WT strain, achieving conversion rates of 17 nmol 10^8 $cells^{-1}$ h^{-1} and conversion yield of 0.87 H_2 per glucose equivalent (8.9% theoretical maxima). Simultaneous monitoring of the intracellular NAD(P)H concentration and H_2 production rate by these mutants reveals an inverse correspondence between these variables, indicating hydrogenase-dependent H_2 production is a major reductant sink for balancing NAD(P)H energy resources in preference to loss of carbon as excreted lactate from these cells.

1. Introduction

Cyanobacteria are found to grow in a diverse range of habitats and are subjected to continuous fluctuations in the inorganic carbon (Ci) availability (Badger *et al.*, 2006). Limited Ci availability can rate-limit photosynthesis and thus growth of cyanobacteria. Therefore, to accommodate for sudden shifts in carbon availability, cyanobacteria have evolved several adaptive mechanisms to maximize CO_2 uptake and/or carbon fixation, which are collectively termed as carbon concentration mechanisms (CCM) (Kaplan *et al.*, 1999), (Kaplan *et al.*, 1991), (Badger *et al.*, 2003), (Price *et al.*, 2008), (Burnap *et al.*, 2015). Transcription factors belonging to the LysR-type transcriptional regulator family (LTTR) are known to regulate expression of genes encoding the structural components of CCM in cyanobacteria in response to dynamic changes in the external Ci availability (Figge *et al.*, 2001), (Omata *et al.*, 2001), (Wang *et al.*, 2004), (Daley *et al.*, 2012), (Burnap *et al.*, 2015) . The LTTR family is constituted of both transcriptional activators and repressors, including a) CcmR (Repressor of high affinity Ci uptake genes), b) CmpR (Activator of ABC-type bicarbonate transporter genes) c) ycf30 (Activator of Calvin-Benson-Bassham cycle genes) and d) NtcB (Activator of nitrate assimilation genes) (Figge *et al.*, 2001), (Omata *et al.*, 2001), (Wang *et al.*, 2004), (Daley *et al.*, 2012), (Burnap *et al.*, 2015). Of these, CcmR coordinates the transcriptional repression of genes encoding the high-affinity Ci transporters under Ci sufficiency conditions (Woodger *et al.*, 2007), (Wang *et al.*, 2004), (Figge *et al.*, 2001), (Omata *et al.*, 2001). Important targets for CcmR have been shown to be high-affinity CO_2 transporter genes, *ndhF-III, ndhD-III, chpY (cupA)* (Woodger *et al.*, 2007), (Wang *et al.*, 2004), inducible HCO_3^- transporter genes, *bicA* and *sbtA* and putative HCO_3^- porin gene, *porB* (Woodger *et al.*, 2007). Loss of *ccmR* gene has been shown to be sufficient to fully induce high affinity CCM even under Ci sufficiency conditions (Woodger *et al.*, 2007). However, the mechanism that CcmR detects the levels of Ci is still not fully understood, which was reported to be regulated by NADPH, 2-oxoglutarate or by direct interaction with Ci itself in the freshwater cyanobacterium *Synechocystis*

sp. PCC 6803 (Daley *et al.*, 2012). In summary, CcmR regulates the transition from a basal CCM to a CCM with high affinity for Ci when the external Ci conditions are low.

The photosynthetic metabolism and the genome wide expression pattern in the euryhaline cyanobacterium *Synechococus sp*. PCC 7002 (henceforth, *Synechococcus* 7002) with inactivated *ccmR* gene has been previously studied (Woodger *et al.*, 2007), (Zhang et al., in preparation). Expression levels of the high affinity CCM genes including *ndhF-III*, *ndhD-III*, *cupA*, *sbtA* and *bicA* were found to be highly up-regulated (Zhang et al., in preparation), (Woodger *et al.*, 2007) in the *ccmR* mutant compared to the wild type strain. Interestingly, together with the CCM related genes, in our studies (Zhang et al., in preparation) the *ccmR* mutant also revealed alterations in mRNA levels of multiple fermentative enzymes. Of note was the 2-9 fold enhanced expression of 12 of the 15 genes related to [Ni-Fe] bidirectional hydrogenase and associated maturation factors (Zhang et al., in preparation). Fig. 1-2 is a schematic representation of the fermentative metabolism in *Synechococcus* 7002.

Therefore, in an effort to understand the metabolic consequences of the *ccmR* gene on fermentation, the kinetics of autofermentation were studied in the *ccmR* mutant as well as the wild type strain of *Synechococcus* 7002 by analyzing the excreted fermentative metabolites, glycolytic rates, cellular energy charge (CEC) and by continuous monitoring of intracellular NAD(P)H levels. Even though lactate production is thermodynamically the most favorable fermentative pathway ($E_{0\,(pyruvate/lactate)}$=-185mV) for carbon, a greater fraction of the catabolized pyruvate was converted and excreted as acetate in the *ccmR* mutant, demonstrating the preference of ATP producing pathway over the NAD(P)H consuming lactate pathway under autofermentative conditions. However, cellular energy charge did not change significantly, indicating the presence of alternate ATP consuming pathways in the *ccmR* mutant. Continuous and simultaneous monitoring of H_2 and NADPH via milking strategy revealed that the excess redox poise caused by the loss in lactate production was in part dissipated by the higher H_2 production. These results indicate that *ccmR*

mutant remodels the fermentative metabolism to balance the ATP producing and the consuming pathways while using hydrogenase as a reductant vent. Further, we demonstrate the potential of using the *ccmR* mutant as a platform for metabolically engineering and improving H_2 production by 6-8 fold.

2. Experimental Procedures:

2.1) Growth conditions

All the strains were grown photoautotrophically in A^+ medium (Stevens *et al.*, 1973) bubbled with 2% CO_2 in air and supplemented with 2 µM $NiCl_2$. Cells were incubated at 38ºC and illuminated with 150 µE m^{-2} s^{-1} white light. Appropriate antibiotics were added in the following concentrations when needed: spectinomycin (50 µg ml^{-1}), kanamycin (100 µg ml^{-1}), gentamycin (20 µg ml^{-1}) and erythromycin (20 µg ml^{-1}).

2.2) Mutant construction and segregation:

The *ccmR* mutant was generated by deleting the coding sequence of SynPCC7002_A0171 (*ccmR*) in the wild type *Synechococcus* 7002 strain, and replaced by a DNA fragment encoding an antibiotic resistance gene (*aphAII*, kanamycin resistance) using the homologous recombination method as previously described (Frigaard *et al.*, 2004). The Δ*ccmR* + *gap1*$^+$ strain was generated using the same approach by deleting the coding sequence of SynPCC7002_A0171 in the *gap1*$^+$ strain (Kumaraswamy et al., 2013), and replaced with the erythromycin resistance gene (*erm*). Upstream and downstream regions of SynPCC7002_A0171 were amplified by PCR using primer sets ccmRD1-ccmRD2 and ccmRD3-ccmRD4 (Table 4-1). The *ldhA* gene (SynPCC7002_G0164) was then deleted in the Δ*ccmR* + *gap1*$^+$ strain and replaced by a DNA fragment encoding *aacC1*, which confers resistance to gentamycin, to generate the Δ*ccmR* + *gap1*$^+$ + *ldhA*$^-$ strain, using the homologous recombination method as previously described (Frigaard *et al.*, 2004). Primer sets ldhAD1-ldhAD2 and ldhAD3-ldhAD4 (Table 4-1) were used by PCR to amplify the upstream and downstream region of SynPCC7002_G0164. The complete segregation of alleles for *ccmR* or *ldhA*

was then verified by PCR using primer set ccmRD1-ccmRD4 or ldhAD1-ldhAD4, with template DNAs from both the wild type strain and mutants. In addition, the *ldh*$^{-}$ strain (McNeely *et al.*, 2010) and *gap1*$^{+}$ strain (Kumaraswamy *et al.*, 2013) were used as control strains.

2.3) Transcriptomic profiling and analysis

Transcriptome profiling of the Δ*ccmR* mutant as well as wild type strain was performed as described (Ludwig *et al.*, 2011). The *ccmR* mutant and wild-type strain were grown in A^{+} under standard conditions and harvested at $OD_{730\ nm}$ = 0.7 (Ludwig *et al.*, 2011). Total RNA was then extracted and rRNA depletion was performed in both strains as described (Gan et al., 2014). The cDNA libraries were then constructed and sequenced (Illumina) in the Genomic Core Facility at The Pennsylvania State University. The BWA software package was used to mapping the sequence reads against the *Synechococcus* sp. PCC 7002 genome (Li *et al.*, 2009). Self-developed scripts were then used to analyze the resulting alignment files and extract expression levels for each gene as described previously (Zhang *et al.*, 2015). The raw sequence data has been deposited to NCBI SRA database with accession number SRR2086086

2.4) Oxygen measurements

Light saturated oxygen evolution and dark respiration rates were measured using a membrane covered Clark-type O_2 (*Hansatech*) electrode at 38^{o}C in A^{+} media containing 25 mM $NaHCO_3$. Samples were illuminated with red light at an intensity of 680 µE m^{-2} s^{-1}. The gross oxygen evolution rate (the total oxygen evolved in light plus the respiration rate) is reported in the results.

2.5) In vitro hydrogenase assay

In vitro hydrogenase assay, was done as described in (King *et al.*, 2006). Autotrophically grown cells in the exponential phase of growth were washed in NO_3^{-} free A^{+} medium and concentrated to a density of 10^{10} cells/ml. Cells were incubated in anaerobic vials for two hours to activate hydrogenase after which the cells were lysed with BugBuster (EMD Millipore) and incubated with

1mM methyl viologen and 5mM sodium dithionite for 2 hrs. Headspace H_2 was measured by gas chromatography.

2.6) Autofermentation:

For autofermentation experiments, cells were grown to the early exponential phase (~7-8 x 10^7 cells ml^{-1} and comparable to the conditions under which transcriptomic profiling was performed) at which point, the cells were harvested, washed with A^+ medium lacking NO_3^- and resuspended in the same volume of NO_3^- free A^+ medium and supplemented with 2 µM $NiCl_2$. 4ml aliquots were placed into anaerobic vials. The headspace air in the vials was replaced with argon and autofermented for 5 days in the dark.

2.7) Analytical Assays

Hydrogen in the headspace of the assay vials were sampled with a gas-tight syringe and measured by gas chromatography using Perkin-Elmer Clarus 680 series equipped with a thermal conductivity detector and using argon as the carrier gas. After measuring the headspace gases, 1 ml of cells from the fermentation vials was harvested and the spent media was separated from the cells by centrifugation. The cell pellet was analyzed for total reducing carbohydrate content using anthrone reagent (Hassid *et al.*, 1957) as described previously (McNeely *et al.*, 2010). The cell-free supernatant was analyzed by Perkin-Elmer HPLC with a Rezex ROA column (300 x 7.8 mm, Phenomenex) equipped with UV detection at 210 nm for excreted fermentation metabolites including lactate, acetate and succinate. All of the above steps were done at 24, 72 and 120h after the onset of fermentation.

2.8) LC-MS

Adenylate and pyridine nucleotide levels were quantified using LC-MS as described previously (McNeely *et al.*, 2010) after 3 days of autofermentation. Briefly, aliquots of cultures from the fermentation vials were subjected to rapid vacuum filtration and the filter with cells were submerged and quenched in 80:20 MeOH:Water mixture incubated on dry ice. Cells were scrapped

off the filters and the solvent with cells was transferred into microcentrifuge tubes and incubated at -20^{o}C for 20 min for metabolite extraction. The supernatant with the metabolites was separated from the cells by centrifugation and vacuum dried (Labconco Centri-Vap concentrator). The vacuum dried pellet was resuspended in LC-MS grade water and analyzed using Agilent 1200 series HPLC coupled to a 6490 QQQ mass analyzer equipped with an ion spray source. The acquired data was analyzed using Agilent Mass Hunter software.

2.9) Real-time H_2 and NAD(P)H detection

Real-time dissolved H_2 and NAD(P)H were determined using a home-built reverse Clark-type electrode coupled to a fluorometer capable of detecting NAD(P)H fluorescence as described in (Ananyev *et al.*, 2012). The Clark-electrode continuously consumes the generated H_2 and therefore, the electrode measures the rate of H_2 production rather than the concentration of dissolved H_2. The rate is presented as electrical current (nA) and is converted to gas nmoles using Faraday's second law of electrolysis. For instantaneous NAD(P)H measurement the sample was illuminated by pulsed UV light (λmax=365 nm, 1000 $\mu W/cm^2$, T=250ms) and recorded by a photodiode. The fluorescence emission was filtered by an emission filter (λmax= 450 nm). For measurements, *Synechococcus spp.* 7002 cells were taken from photoautotrophically growing cultures at a density of 7-8 x 10^7 cells/ml and concentrated to 10^{10} cells/ml and transferred to sample cavity of the electrode. The sample was covered with a coverslip to prevent diffusion of air into the cavity. Cellular respiration consumes the internal O_2 pool and creates anoxic conditions within 2-3 minutes. Experiments were performed in triplicates. All figures presented in the results here are a representative single trace.

3. Results

3.1) Mutant construction

To investigate the possible implications of CcmR on fermentative metabolism and H_2 production, a *ccmR* deletion mutant of *Synechococcus* 7002 (*ΔccmR)* was constructed (Fig. 4-1 A) and the complete segregation of the alleles was confirmed (Fig. 4-1 B).

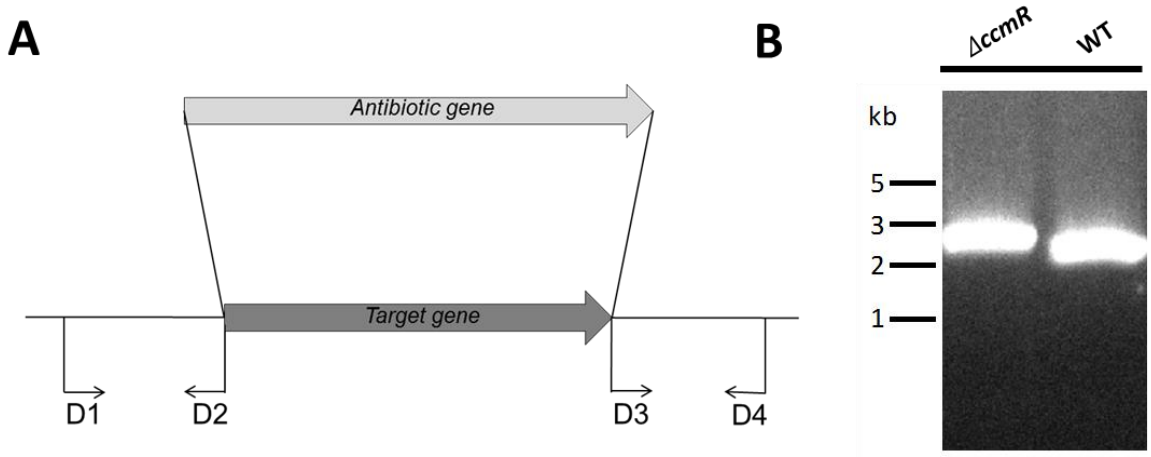

Figure 4-1 **Scheme for mutant construction and verification of mutants**. A) General scheme showing the homologous recombination methods by which the target gene is replaced with antibiotic resistance cassettes. In detail, the upstream and downstream flanking regions for a gene of interest was amplified by PCR using primer pairs D1-D2 and D3-D4, after which these fragments were ligated to the antibiotic cassette. The resulting construction was then used to generate fully segregated mutants as described in the Materials and Methods. B) Agarose gel electrophoretic analysis of PCR products using template DNA derived from wild type (WT) or *ΔccmR* mutants, verifying the complete segregation of alleles of the interested gene in mutants, lane 1 *ΔccmR*, using primer set ccmRD1-ccmRD4

Name	Sequence (5’ to 3’)
ccmRD1	ATCTAGGGCTTGGCGATCGCGGATAAAACT
ccmRD2	TAGGGTCGACGGGTTTACTCCTGAACTTGT
ccmRD3	GCCAGAATTCAAGCTCAAAATTGTTGGGCC
ccmRD4	TCAAGCCAGAGGTGTAAAGGAAATTGGGCG
ldhAD1	CAGACCCAGAAGACCAGAGGCGCTTAAGCT
ldhAD2	TATGATGTCGACGGTGCTTTGGGGTAATGG
ldhAD3	GCGCTGGAATTCAAACTGCGCCAAGAATAG
ldhAD4	TAGGATCAATTTACGTCTTTGTTGGCGCAA

Table 4-1 Primer sequences used for the construction of mutants.

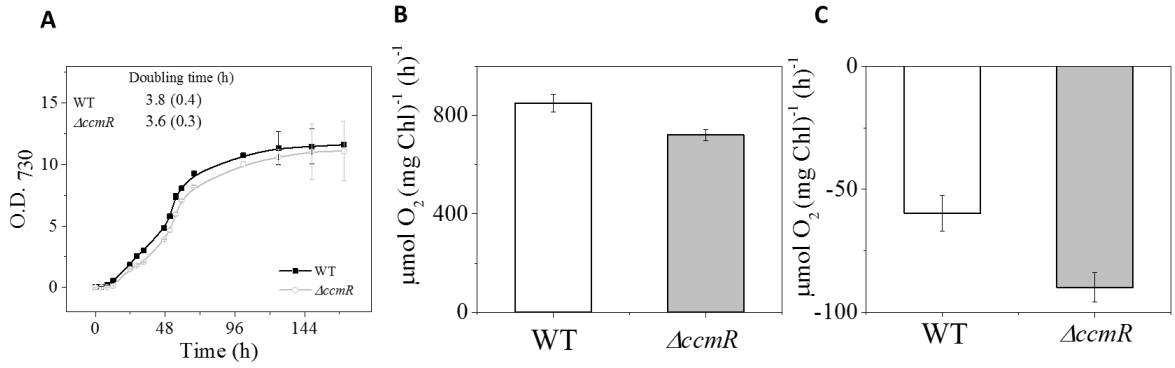

Figure 4-2 **Photoautotrophic phenotypes for *ΔccmR* and Wt**.A) Growth curve of *ΔccmR* and Wt. Data represents the mean of three biological replicates with standard error grown under 150 µE $m^{-2}s^{-1}$ illumination with constant bubbling of 2% CO_2. The inset shows the calculated doubling time based on fits to Gompertz curve. B) Gross photosynthetic oxygen evolution rate and C) respiration rate measured at 38ºC under light saturating conditions of 680 µE $m^{-2}s^{-1}$ of red light and in the presence of 25 mM bicarbonate.

Fig. 4-2 A compares photoautotrophic growth of the *ΔccmR* strain and the wild-type (WT) strain when grown under an irradiance of 150 µE $m^{-2}s^{-1}$ (white fluorescent light) and with constant bubbling with 2% CO_2 in air. The growth-rates were not significantly different between the mutant ($T_{doubling}$: 3.6 ± 0.3 h) and the WT ($T_{doubling}$: 3.8 ± 0.4 h) strains. The light-saturated (680 µE m^{-2} s^{-1} red light) photosynthetic oxygen evolution rate (Fig. 4-2 B) and the respiration rates (Fig. 4-2 C) were also measured. The oxygen evolution rate was lower in *ΔccmR* (720 ± 21.5 µmol O_2 $(mg\ Chl)^{-1}$ $(h)^{-1}$) vs. in WT (850 ± 35.6 µmol O_2 $(mg\ Chl)^{-1}$ $(h)^{-1}$). By contrast, the respiration rate was higher in the *ΔccmR* mutant (89 ± 6.02 µmol O_2 $(mg\ Chl)^{-1}$ $(h)^{-1}$ vs. in WT (59 ± 7.22 µmol O_2 $(mg\ Chl)^{-1}$ $(h)^{-1}$). These results suggest that under high light and Ci concentration, the loss of CcmR does not confer a growth/photosynthetic advantage (or disadvantage) and instead shows a 15% decrease in the photosynthetic oxygen evolution rate and a 50% increase in the respiration rate.

3.2) Transcript profiling:

To gain a deeper understanding of the possible relations between CcmR, fermentative metabolism and other metabolic pathways, rRNA-depleted total RNAs from the *ΔccmR* and WT strain were used for transcript profiling. The whole cell transcriptomic profiling was done with cells grown under photoautotrophic and Ci sufficient conditions. For analysis, an expression cut-off threshold of 2-fold higher or lower than the expression in the WT in combination with a *p-value* <0.05 was used. A few important genes based on the metabolic pathways were extracted and are displayed in Table 4-2.

Gene name	WT	*ΔccmR*	*Fold Change (ΔccmR/ WT)*	*p-value*	*Gene Symbol*		*Metabolic pathway*
Hydrogenase							
SYNPCC7002_A0194	1.13E-05	1.76E-05	1.566	0.05-0.02	hypE	hydrogenase expression/formation protein HypE	H2ase
SYNPCC7002_A0195	3.26E-05	0.000188424	5.773	<0.001	hoxE	hydrogenase subunit E ([NiFe] hydrogenase subunit)	H2ase/complex1
SYNPCC7002_A0196	4.25E-05	0.000169283	3.987	<0.001	hoxF	hydrogenase large diaphorase subunit F	H2ase/complex1
SYNPCC7002_A0197	2.28E-05	6.13E-05	2.687	<0.001	hoxU	hydrogenase small diaphorase subunit U	H2ase/complex1
SYNPCC7002_A0198	2.11E-05	5.68E-05	2.695	<0.001	hoxY	hydrogenase small subunit Y	H2ase
SYNPCC7002_A0199	2.80E-05	4.82E-05	1.719	<0.001	hyp3	CBS domain-containing protein; possibly associated with hydrogenase assembly	H2ase
SYNPCC7002_A0200	4.39E-05	7.75E-05	1.764	<0.001	hoxH	hydrogenase large subunit H	H2ase
SYNPCC7002_A0201	1.65E-05	2.39E-05	1.453	0.05-0.02	hoxW	hydrogenase maturation protease	H2ase
SYNPCC7002_A0202	5.20E-06	1.17E-05	2.243	0.01-0.001	hypA	hydrogenase nickel insertion protein HypA	H2ase
SYNPCC7002_A0203	1.53E-05	2.69E-05	1.758	<0.001	hypB	hydrogenase isoenzymes formation protein; HypB	H2ase
SYNPCC7002_A0204	1.56E-05	3.62E-05	2.320	<0.001	hypF	[NiFe] hydrogenase maturation protein HypF	H2ase
SYNPCC7002_A0205	1.56E-05	4.43E-05	2.838	<0.001	hypC	hydrogenase assembly chaperone HypC/HupF	H2ase
SYNPCC7002_A0206	6.35E-05	0.000148048	2.330	<0.001	hypD	hydrogenase expression/formation protein HypD	H2ase

SYNPCC7002_A1746	7.16E-05	0.000172573	2.409	<0.001	hypA	hydrogenase nickel insertion protein	H2ase
SYNPCC7002_A1747	8.38E-05	0.000170479	2.035	<0.001	hypB	hydrogenase accessory protein HypB	H2ase
SYNPCC7002_A1849	0.000107742	8.43E-05	0.783	0.01-0.001	lexA	LexA repressor	transcription/H2ase

CCM related genes

SYNPCC7002_A0171	0.000132872	3.89E-06	0.029	<0.001	rbcR	transcription regulator of rubisco operon, RbcR (LysR family)	CO2-conc-fix/transcription
SYNPCC7002_A0172	8.61E-05	0.000723789	8.409	<0.001	ndhF-III	NADH2 dehydrogenase (plastoquinone) chain 5	CO2-conc-fix
SYNPCC7002_A0173	4.33E-05	0.000380139	8.774	<0.001	ndhD-III	proton-translocating NADH-quinone oxidoreductase (NADH dehydrogenase subunit 4)	CO2-conc-fix
SYNPCC7002_A0174	3.93E-05	0.000282337	7.187	<0.001	cupA	CO2 hydration protein	CO2-conc-fix
SYNPCC7002_A0175	1.99E-05	0.000138477	6.948	<0.001	'cupS'	conserved hypothetical protein	CO2-conc-fix
SYNPCC7002_A0470	3.38E-05	0.008090281	239.388	<0.001	'sbtA'	sodium-dependent bicarbonate transporter	CO2-conc-fix
SYNPCC7002_A0690	0.000133161	0.000116644	0.876	0.1-0.05	-	probable bicarbonate transporter, ICT family protein	CO2-conc-fix
SYNPCC7002_A1414	0.000274987	0.000195901	0.712	<0.001	ppc	phosphoenolpyruvate carboxylase	CO2-conc-fix
SYNPCC7002_A1796	0.002537278	0.000720798	0.284	<0.001	rbcS	Ribulose bisphosphate carboxylase, small subunit	CO2-conc-fix/calvinCycle
SYNPCC7002_A1797	0.00316582	0.000951094	0.300	<0.001	rbcX	RbcX protein, possible rubisco chaperone	CO2-conc-fix
SYNPCC7002_A1798	0.009051184	0.002814401	0.311	<0.001	rbcL	ribulose-1,5-bisphosphate carboxylase, large subunit	CO2-conc-fix/calvinCycle

SYNPCC7002_A1799	0.000334491	0.000109466	0.327	<0.001	ccmN	Carbon dioxide concentrating mechanism protein	CO2-conc-fix
SYNPCC7002_A1800	0.002824397	0.000850003	0.301	<0.001	ccmM	carbon dioxide concentrating mechanism protein	CO2-conc-fix
SYNPCC7002_A1801	0.000615544	0.000154927	0.252	<0.001	ccmL	carbon dioxide concentrating mechanism protein	CO2-conc-fix
SYNPCC7002_A1802	0.000599657	0.000164497	0.274	<0.001	ccmK	Carbon dioxide concentrating mechanism protein	CO2-conc-fix
SYNPCC7002_A1803	0.000575682	0.000153132	0.266	<0.001	ccmK	carbon dioxide concentrating mechanism protein	CO2-conc-fix
SYNPCC7002_A1805	0.001395156	0.000960067	0.688	<0.001	ndhF4	NADH dehydrogenase subunit F4	CO2-conc-fix
SYNPCC7002_A1806	0.000811097	0.000611033	0.753	<0.001	ndhD4	NADH dehydrogenase subunit D4	CO2-conc-fix
SYNPCC7002_A1807	0.000482383	0.000393298	0.815	<0.001	'cupB'	CO2 hydration protein	CO2-conc-fix
SYNPCC7002_A1997	8.32E-05	4.91E-05	0.590	<0.001	icfA	carbonic anhydrase	CO2-conc-fix
SYNPCC7002_A2025	4.45E-05	3.38E-05	0.760	0.05-0.02	-	conserved hypothetical protein	CO2-conc-fix
SYNPCC7002_A2371	0.000123051	0.012784438	103.895	<0.001	bicA	bicarbonate transporter, BicA	CO2-conc-fix
SYNPCC7002_A2389	0.000175333	0.000122027	0.696	<0.001	ccmk1	carbon dioxide concentrating mechanism protein	CO2-conc-fix
SYNPCC7002_A2612	4.13E-05	3.17E-05	0.768	0.05-0.02	ccmK	carbon dioxide concentrating mechanism protein	CO2-conc-fix
SYNPCC7002_A2613	0.000140382	8.31E-05	0.592	<0.001	ccmK	carbon dioxide concentrating mechanism protein	CO2-conc-fix

Oxidative pentose phosphate pathway

SYNPCC7002_A0010	4.22E-05	5.44E-05	1.291	0.05-0.02	fbaB	fructose-bisphosphate aldolase class I	glycolysis/pentosePpathway/calvinCycle
SYNPCC7002_A0130	3.32E-05	2.45E-05	0.738	0.05-0.02	eda	2-dehydro-3-deoxyphosphogluconate aldolase/4-hydroxy-2-oxoglutarate aldolase	pentosePpathway
SYNPCC7002_A0162	0.000230215	0.000460892	2.002	<0.001	pfkA	6-phosphofructokinase PfkA	glycolysis/pentosePpathway
SYNPCC7002_A0221	0.000238881	0.001024968	4.291	<0.001	gnd	6-phosphogluconate dehydrogenase, decarboxylating	pentosePpathway
SYNPCC7002_A0324	0.000517045	0.000242559	0.469	<0.001	rpe	ribulose-phosphate 3-epimerase	pentosePpathway
SYNPCC7002_A0329	0.000241769	0.000439657	1.818	<0.001	fbp	fructose-1,6-bisphosphatase	glycolysis/pentosePpathway/calvinCycle
SYNPCC7002_A0928	9.56E-05	0.000177956	1.861	<0.001	pgl	6-phosphogluconolactonase	pentosePpathway
SYNPCC7002_A0964	0.000240036	0.000380438	1.585	<0.001	pgi	glucose-6-phosphate isomerase	glycolysis/pentosePpathway/StarchSucroseMetabolism
SYNPCC7002_A1022	0.002646753	0.002032889	0.768	<0.001	tkt	transketolase	pentosePpathway/calvinCycle
SYNPCC7002_A1269	0.000144137	5.95E-05	0.413	<0.001	rpiA	ribose 5-phosphate isomerase A	pentosePpathway/calvinCycle
SYNPCC7002_A1301	0.001543337	0.00063825	0.414	<0.001	-	Bacterial fructose-1,6-bisphosphatase, glpX-encoded superfamily	glycolysis/pentosePpathway/calvinCycle
SYNPCC7002_A1352	0.004438214	0.002276943	0.513	<0.001	fba	fructose-bisphosphate aldolase, class II, Calvin cycle subtype	glycolysis/pentosePpathway/calvinCycle
SYNPCC7002_A1459	9.68E-05	0.00063825	6.596	<0.001	zwf	glucose-6-phosphate 1-dehydrogenase	pentosePpathway
SYNPCC7002_A1460	0.000175044	0.001153575	6.590	<0.001	tal	transaldolase	pentosePpathway

SYNPCC7002_A2558	4.74E-05	2.36E-05	0.499	<0.001	talC	transaldolase	pentosePpathway
SYNPCC7002_A2726	0.000650495	0.000381036	0.586	<0.001	prs	ribose-phosphate pyrophosphokinase	pentosePpathway/Purine Metabolism

Glycolysis

SYNPCC7002_A0010	4.22E-05	5.44E-05	1.291	0.05-0.02	fbaB	fructose-bisphosphate aldolase class I	glycolysis/pentosePpathway/calvinCycle
SYNPCC7002_A0073	0.000434723	0.000186929	0.430	<0.001	eno	2-phosphopyruvate hydratase (enolase)	glycolysis
SYNPCC7002_A0106	0.001326698	0.000519214	0.391	<0.001	gap	glyceraldehyde-3-phosphate dehydrogenase, type I	glycolysis/calvinCycle
SYNPCC7002_A0162	0.000230215	0.000460892	2.002	<0.001	pfkA	6-phosphofructokinase PfkA	glycolysis/pentosePpathway
SYNPCC7002_A0329	0.000241769	0.000439657	1.818	<0.001	fbp	fructose-1,6-bisphosphatase	glycolysis/pentosePpathway/calvinCycle
SYNPCC7002_A0964	0.000240036	0.000380438	1.585	<0.001	pgi	glucose-6-phosphate isomerase	glycolysis/pentosePpathway/StarchSucroseMetabolism
SYNPCC7002_A1301	0.001543337	0.00063825	0.414	<0.001	-	Bacterial fructose-1,6-bisphosphatase, glpX-encoded superfamily	glycolysis/pentosePpathway/calvinCycle
SYNPCC7002_A1352	0.004438214	0.002276943	0.513	<0.001	fba	fructose-bisphosphate aldolase, class II, Calvin cycle subtype	glycolysis/pentosePpathway/calvinCycle
SYNPCC7002_A1585	0.001736868	0.000665766	0.383	<0.001	pgk	phosphoglycerate kinase	glycolysis/calvinCycle
SYNPCC7002_A2233	0.001014449	0.000605949	0.597	<0.001	gpm	2,3-bisphosphoglycerate-independent phosphoglycerate mutase	glycolysis
SYNPCC7002_A2560	7.13E-05	3.62E-05	0.507	<0.001	gpmB	phosphoglycerate mutase	glycolysis
SYNPCC7002_A2697	2.02E-05	0.000327798	16.212	<0.001	gap	glyceraldehyde-3-phosphate dehydrogenase, type I	glycolysis

Pyruvate Metabolism

SYNPCC7002_A0110	0.000303584	0.000195602	0.644	<0.001	-	dihydrolipoamide S-acetyltransferase; 2-oxo acid dehydrogenases acyltransferase (catalytic domain)	pyruvate
SYNPCC7002_A0250	0.000266322	0.000955879	3.589	<0.001	ppsA	phosphoenolpyruvate synthase	pyruvate
SYNPCC7002_A0291	0.000260545	0.00023568	0.905	0.05-0.02	-	conserved hypothetical PEP-utilizing protein	pyruvate
SYNPCC7002_A0353	0.00028943	0.000144758	0.500	<0.001	'pdhA'	pyruvate dehydrogenase E1 component, alpha chain	pyruvate
SYNPCC7002_A0655	0.000236859	0.000151637	0.640	<0.001	pdhB	pyruvate dehydrogenase E1 beta chain	pyruvate
SYNPCC7002_A1443	6.41E-05	0.000370568	5.779	<0.001	nifJ	pyruvate:ferredoxin (flavodoxin) oxidoreductase	pyruvate
SYNPCC7002_A1658	0.000280764	0.000175863	0.626	<0.001	pyk	pyruvate kinase	pyruvate

Calvin Cycle

SYNPCC7002_A0010	4.22E-05	5.44E-05	1.291	0.05-0.02	fbaB	fructose-bisphosphate aldolase class I	glycolysis/pentosePpathway/calvinCycle
SYNPCC7002_A0106	0.001326698	0.000519214	0.391	<0.001	gap	glyceraldehyde-3-phosphate dehydrogenase, type I	glycolysis/calvinCycle
SYNPCC7002_A0162	0.000230215	0.000460892	2.002	<0.001	pfkA	6-phosphofructokinase PfkA	glycolysis/pentosePpathway
SYNPCC7002_A0329	0.000241769	0.000439657	1.818	<0.001	fbp	fructose-1,6-bisphosphatase	glycolysis/pentosePpathway/calvinCycle
SYNPCC7002_A0595	0.000189198	0.000126214	0.667	<0.001	tpiA	triosephosphate isomerase	calvinCycle

SYNPCC7002_A1301	0.001543337	0.00063825	0.414	<0.001	-	Bacterial fructose-1,6-bisphosphatase, glpX-encoded superfamily	glycolysis/pentosePpathway/calvinCycle
SYNPCC7002_A1352	0.004438214	0.002276943	0.513	<0.001	fba	fructose-bisphosphate aldolase, class II, Calvin cycle subtype	glycolysis/pentosePpathway/calvinCycle
SYNPCC7002_A1585	0.001736868	0.000665766	0.383	<0.001	pgk	phosphoglycerate kinase	glycolysis/calvinCycle
SYNPCC7002_A1796	0.002537278	0.000720798	0.284	<0.001	rbcS	Ribulose bisphosphate carboxylase, small subunit	CO2-conc-fix/calvinCycle
SYNPCC7002_A1798	0.009051184	0.002814401	0.311	<0.001	rbcL	ribulose-1,5-bisphosphate carboxylase, large subunit	CO2-conc-fix/calvinCycle
SYNPCC7002_A2665	0.002403539	0.001985334	0.826	<0.001	prk	phosphoribulokinase	calvinCycle
SYNPCC7002_A2857	0.000419991	0.000256018	0.610	<0.001	prk	Phosphoribulokinase	calvinCycle

NADPH dehydrogenase

SYNPCC7002_A0195	3.26E-05	0.000188424	5.773	<0.001	hoxE	hydrogenase subunit E ([NiFe] hydrogenase subunit)	H2ase/complex1
SYNPCC7002_A0196	4.25E-05	0.000169283	3.987	<0.001	hoxF	hydrogenase large diaphorase subunit F	H2ase/complex1
SYNPCC7002_A0197	2.28E-05	6.13E-05	2.687	<0.001	hoxU	hydrogenase small diaphorase subunit U	H2ase/complex1
SYNPCC7002_A0560	2.34E-05	1.35E-05	0.575	0.01-0.001	ndhL	NADH dehydrogenase subunit L (inorganic carbon tranpsort protein)	complex1
SYNPCC7002_A0854	0.001572223	0.001497524	0.952	0.02-0.01	ndhF	NADH dehydrogenase subunit 5	complex1
SYNPCC7002_A0923	0.000186599	0.000220427	1.181	0.01-0.001	ndhE	NADH dehydrogenase subunit E	complex1

SYNPCC7002_A0924	0.000300406	0.000351725	1.171	<0.001	ndhG	NADH dehydrogenase subunit G	complex1
SYNPCC7002_A0926	0.000461008	0.000545234	1.183	<0.001	ndhA	NADH dehydrogenase subunit A	complex1
SYNPCC7002_A1143	0.000142404	0.000122625	0.861	0.05-0.02	'ndhN'	conserved hypothetical protein	complex1
SYNPCC7002_A1432	3.29E-05	5.98E-05	1.817	<0.001	-	Na+-transporting NADH:ubiquinone oxidoreductase subunit 2	complex1?
SYNPCC7002_A1973	6.07E-05	8.82E-05	1.455	<0.001	ndhD2	NADH dehydrogenase subunit D2	complex1
SYNPCC7002_A2000	0.001096194	0.001832202	1.671	<0.001	ndhD1	NADH dehydrogenase subunit D1	complex1
SYNPCC7002_A2311	0.000279609	0.000122326	0.437	<0.001	ndbA	type II NADH dehydrogenase A	complex1-B
SYNPCC7002_A2327	0.000178222	9.66E-05	0.542	<0.001	ndhD	NADH dehydrogenase subunit 4	complex1
SYNPCC7002_A2541	0.000608612	0.000524896	0.862	<0.001	ndhH	NADH dehydrogenase subunit H	complex1
SYNPCC7002_A2547	0.001838255	0.001596522	0.868	<0.001	ndhB	NADH dehydrogenase subunit B	complex1
SYNPCC7002_A2748	0.000179666	0.000234484	1.305	<0.001	ndhC	NADH dehydrogenase subunit C	complex1
SYNPCC7002_A2749	0.000434434	0.000523401	1.205	<0.001	ndhK	NADH dehydrogenase subunit K	complex1
SYNPCC7002_A2750	0.000303584	0.000397186	1.308	<0.001	ndhJ	NADH dehydrogenase subunit J	complex1

Terminal oxidase

SYNPCC7002_A0725	2.05E-05	4.19E-05	2.042	<0.001	ctaEII	cytochrome oxidase II small subunit	cytOxidase
SYNPCC7002_A0726	0.000172445	0.000275458	1.597	<0.001	ctaDII	cytochrome oxidase II large subunit	cytOxidase
SYNPCC7002_A0727	6.01E-05	7.69E-05	1.279	0.01-0.001	ctaCII	Cytochrome C oxidase subunit II	cytOxidase

SYNPCC7002_A1162	0.000238881	0.000837441	3.506	<0.001	ctaCI	cytochrome oxidase subunit II	cytOxidase
SYNPCC7002_A1163	0.000267477	0.000804243	3.007	<0.001	ctaDI	cytochrome oxidase large subunit (subunit I)	cytOxidase
SYNPCC7002_A1164	0.000129983	0.00028473	2.191	<0.001	ctaEI	cytochrome oxidase small subunit (subunit III)	cytOxidase

ATP synthase

SYNPCC7002_A0733	0.001631726	0.001300726	0.797	<0.001	atpG	ATP synthase F1, gamma subunit	ATPase
SYNPCC7002_A0734	0.002833929	0.002185124	0.771	<0.001	atpA	ATP synthase F1, alpha subunit	ATPase
SYNPCC7002_A0735	0.000810519	0.000591293	0.730	<0.001	atpH	ATP synthase F1, delta subunit	ATPase
SYNPCC7002_A0736	0.000904396	0.000637353	0.705	<0.001	atpF	ATP synthase B chain (Subunit I)	ATPase
SYNPCC7002_A0737	0.00100925	0.000731266	0.725	<0.001	atpG	ATP synthase B chain (Subunit II)	ATPase
SYNPCC7002_A0738	0.001033513	0.000750407	0.726	<0.001	atpE	ATP synthase C chain (Lipid-binding protein)	ATPase
SYNPCC7002_A0739	0.002569052	0.0019638	0.764	<0.001	atpB	ATP synthase F0, A subunit	ATPase
SYNPCC7002_A0740	0.00240845	0.002217425	0.921	<0.001	atp1	ATP synthase subunit I	ATPase
SYNPCC7002_A0749	0.003338554	0.002128297	0.637	<0.001	atpD	ATP synthase beta chain	ATPase
SYNPCC7002_A0750	0.000681114	0.000377148	0.554	<0.001	atpC	ATP synthase F1, epsilon subunit	ATPase
SYNPCC7002_G0144	8.69E-05	0.000287721	3.309	<0.001	atpD	ATP synthase F1, beta subunit	ATPase
SYNPCC7002_G0145	2.48E-05	6.73E-05	2.709	<0.001	atpC-II	ATP synthase epsilon subunit	ATPase
SYNPCC7002_G0146	1.99E-05	5.77E-05	2.896	<0.001	-	F0F1-ATPase subunit, putative	ATPase
SYNPCC7002_G0148	3.99E-05	0.000107073	2.686	<0.001	atpB-II	ATP synthase F0, A subunit	ATPase

SYNPCC7002_G0149	2.22E-05	4.46E-05	2.004	<0.001	atpH-II	ATP synthase c subunit	ATPase
SYNPCC7002_G0150	6.56E-05	9.90E-05	1.510	<0.001	atpF-II	ATP synthase b subunit	ATPase
SYNPCC7002_G0151	6.15E-05	8.64E-05	1.405	<0.001	atpA-II	ATP synthase F1, alpha subunit	ATPase

Color coding : **Fold Change ≥2 fold colored in red** **Fold Change ≤2 fold colored in blue**

Table 4-2: Transcript levels for selected protein-coding genes for WT and *ΔccmR*.

Fermentative metabolism and Pyruvate metabolism: Even though the transcriptomic profiling was done under photoautotrophic growth conditions, expression of multiple genes of the fermentative metabolism were differentially expressed. The expression levels of genes encoding subunits of the hydrogenase (Hox) and associated chaperone proteins (10 of the 16 known genes) were significantly enhanced by 2-6 fold (Table 4-2). The hydrogenase genes are co-localized in one operon and the increase in the transcription of multiple genes of this operon suggests a clear regulatory activity of CcmR on this operon.

Under fermentative conditions pyruvate, the end product of glycolysis, is an important intermediate of glycogen catabolism (Fig. 1-2). Pyruvate can be synthesized from precursor phosphoenolpuruvate by either pyruvate kinase (*pk*) which produces ATP from ADP or by phosphoenol puruvate synthase (*ppsA*) that generates ATP from AMP and 2Pi. The expression level of *ppsA* is enhanced by 3.5-fold with unchanged levels of *pk* in the mutant, suggesting *ppsA* being the preferred pathway for the conversion of phosphoenol pyruvate to pyruvate. Once generated, pyruvate may be converted to lactate via lactate dehydrogenase (*ldh*) or to acetyl-CoA by the action of either a) pyruvate:ferredoxin oxidoreductase (*pfor*), or via pyruvate dehydrogenase (*pdh*), both of which decarboxylate pyruvate to acetyl-CoA. PDH reduces NAD^+, while PFOR reduces ferredoxin. Of these, PFOR is sensitive to oxygen and was found to be the dominant enzyme of the two under anaerobic (fermentative) conditions (McNeely et al., 2011). The transcript level of PFOR (also called *nifJ*, SYNPCC7002_A1443) is 5.7-fold higher, while the LDH transcript remains unchanged in the *ccmR* mutant. This observation suggests that catabolic generation of CO_2 and Fd_{red} with retention of reduced carbon (as acetyl-CoA) is the preferred regulatory response to the lack of sufficient intracellular C_i (as opposed to production of the lower energy NADPH reductant via PDH). Interestingly, the expression of the *gap1* gene involved in glycolysis is 16-fold higher in the *ΔccmR* strain than WT. This reversible enzyme is the major site for NADH/NAD^+ dependent carbon fluxes going into gluconeogenesis and glycolytic catabolism.

Oxidative phosphorylation: The transcriptome reveals a considerable remodeling of the respiratory metabolism under photoautotrophic Ci sufficient conditions.*sdhB* (SYNPCC7002_A1094), one of the two subunits of respiratory Complex II and 4 of the 6 genes of terminal oxidase (Complex IV) show at least 2-fold or higher expression levels in the *ΔccmR* strain (Table 4-2). The *ΔccmR* strain also shows increased transcript levels (>2-fold) for genes coding for the Na^+-dependent ATPase subunits: *atpD* (SYNPCC7002_G0144), *atpC*-II (SYNPCC7002_G0145), *atpB*-II (SYNPCC7002_G0148) and *atpH*-II (SYNPCC7002_G0149). This expression difference of the oxidative phosphorylation genes together with the 50% higher respiration rate in the mutant (Fig. 4-2 C) indicates a significantly greater reliance on respiration for energy production in the *ΔccmR*.

Calvin-Benson-Bassham (CBB) Cycle: The genes belonging to the CBB cycle, including the small and large subunits of RuBisCO, *rbcS* (SYNPCC7002_A1796) and *rbcL* (SYNPCC7002_A1798) show a 3.5 and 3.2-fold lower expression levels in the *ΔccmR* mutant under photoautotrophic Ci sufficient condition. The implication of this finding could be that intracellular CO_2 levels are sufficient to induce normal expression levels of these inducible genes. CO_2 generated from the higher respiratory flux may play such a role.

Membrane Transporters: The transcriptome also suggests considerable remodeling of the ion transport system in the *ΔccmR* strain. The mRNA levels for genes encoding bicarbonate transport systems *bicA* (bicarbonate transporter: SYNPCC7002_A2371), *sbtA* (sodium-dependent bicarbonate transporter: SYNPCC7002_A0470) and the Na^+/H^+ antiporter (SYNPCC7002_A2372-A2375 and SYNPCC7002_A2380) are enhanced by 103-, 240- and 100-fold respectively. This, together with the increase in the expression of the Na^+-dependent ATPase show an internal compensatory mechanism to overcome the possible excess sodium import caused by sodium-dependent bicarbonate transport. Furthermore, the transcripts levels for three genes, co-located in one apparent operon, that encode the ABC transporter family proteins (SynPCC7002_A1733, SynPCC7002_A1734, SynPCC7002_A1735) were highly up-regulated (16-34-fold) (Table 4-2).

Thus, it is very likely that the expression of this operon is also regulated by *ccmR* and may also be involved in carbon assimilation or fixation.

In summation, the loss of CcmR results in a remodeling of metabolism with alterations in Ci uptake, bicarbonate transport, and fermentative metabolism, specifically [NiFe]-hydrogenase expression.

3.3) In vitro and in vivo hydrogenase activity and NAD(P)H availability

To establish whether the increased expression level of the *hox* operon translates into a higher hydrogenase activity, we measured extracellular H_2 using the standard methyl viologen (MV) assay on cell lysates from both the WT and the *ΔccmR* strains. After 2 h of dark anaerobic incubation with MV, *ΔccmR* produced a 50% higher yield of H_2 per mg total protein as compared to the WT strain (Fig. 4-3 A), validating that the increase in Hox gene expression does translate into higher hydrogenase activity.

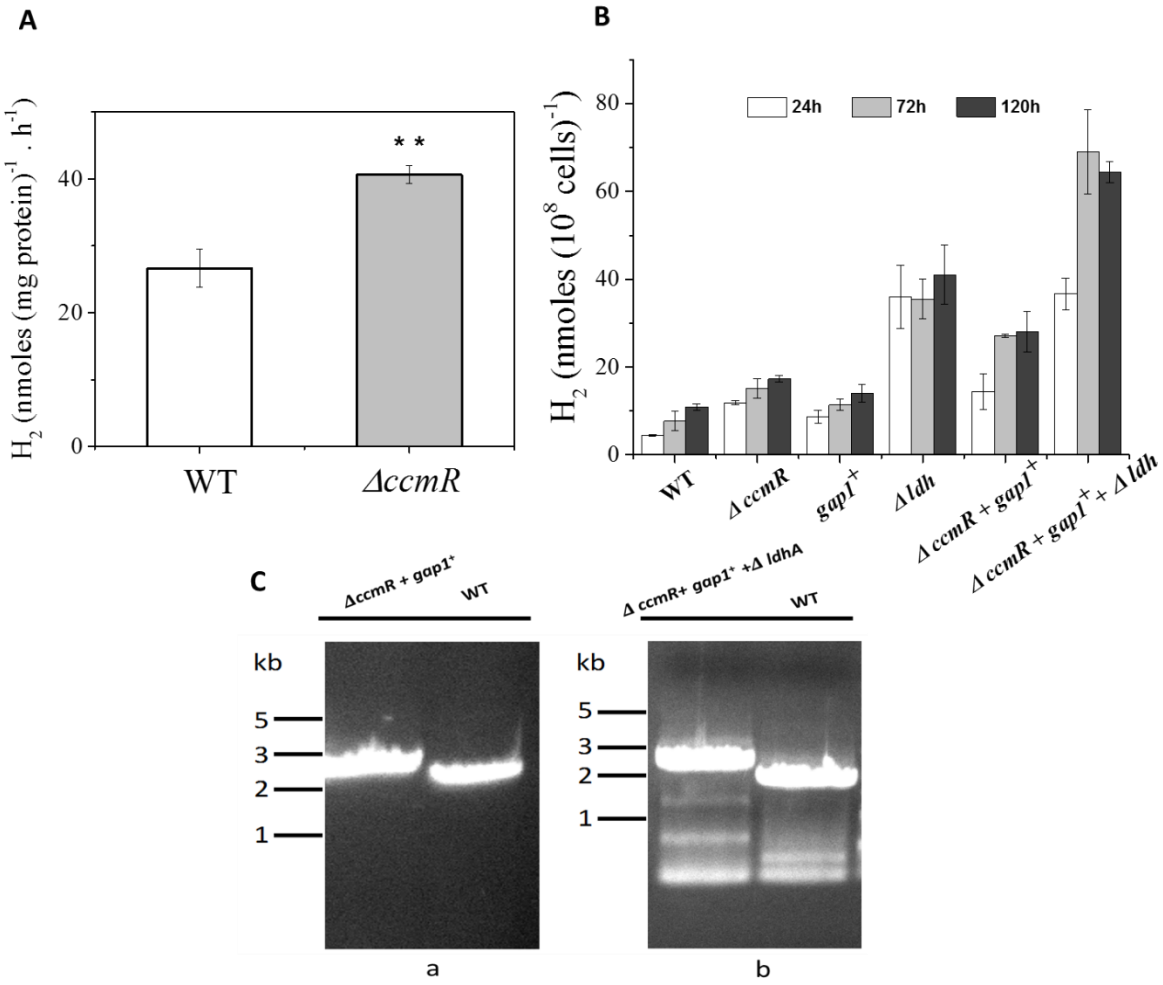

Figure 4-3 **Hydrogenase activity and mutant verification**. A) In vitro hydrogenase specific activity from WT and *ΔccmR* cell lysates after 2 h assayed by methyl viologen/dithionite under anaerobic conditions. B) Kinetics of autofermentative H_2 excretion measured over 120 h in sealed vials. Data represents the average and standard deviation of three biological replicates. ** represents a t-test *p-value* less than 0.005. C) Agarose gel electrophoretic analysis of PCR products using template DNA derived from wild type (WT) or mutants, verifying the complete segregation of alleles of the targeted gene in each mutant: a) *ΔccmR* + *gap1*$^+$ mutant (lane 1 *ΔccmR* + *gap1*$^+$), using primer set ccmRD1-ccmRD4; b) *ΔccmR* + *gap1*$^+$ + *Δldh* mutant (lane1 *ΔccmR* + *gap1*$^+$ + *Δldh*), using primer set ccmRD1-ccmRD4.

The hydrogen production rate of whole cells produced under dark fermentative conditions *(in vivo* activity) was measured either as the concentration of H_2 gas in the headspace by gas chromatography, or as dissolved H_2 in solution using a homebuilt electrochemical cell (Ananyev, 2012). The former method measures the H_2 concentration in equilibrium with cells and thus includes any loss due to the hydrogenase uptake reaction. It was monitored using sealed opaque anaerobic vials over a period of 5 days (Fig. 4-3 B). In these steady-state headspace measurements, *ΔccmR* mutant produced about 1.5-2-fold more H_2 than the WT. The glycolytic rate of the *ΔccmR* mutant was not significantly different than the WT (described later in Section 3.5) even though the *gap1* gene expression was 16-fold higher (Table 4-2). Earlier work has shown that improving *gap1* gene expression by more than 25-fold leads to an improvement in the glycolytic rates and H_2 production (Kumaraswamy et al., 2013). GAPDH1 being a highly regulated enzyme, we hypothesized that the inherent improvement in expression of *gap1* in the *ΔccmR* mutant may not have been sufficient to show a phenotypic difference in the mutant, perhaps owing to insufficient metabolites or altered regulation by changes in the NADH/NAD^+ redox poise (Koksharova et al., 1998), (Garrigues et al., 2001), (Clermont et al., 1993). To test if the glycolytic rate can be enhanced by increasing the GAPDH1 expression level further, we engineered two additional gene changes in the *ΔccmR* background. They are: a) overexpression of glyceraldehyde 3-phosphate dehydrogenase (GAPDH1) (*ΔccmR* +*gap1*$^+$), and b) both overexpression of GAPDH1 and deletion of lactate dehydrogenase (LDH) denoted as (*ΔccmR*+*gap1*$^+$+ *Δldh*). Mutant construction is described in Experimental Procedures and Fig. 4-1 A. Complete segregation of alleles in the mutants was confirmed by PCR (Fig. 4-3 C). The *gap1*$^+$ mutant was previously shown to improve both the glycogen accumulation rate under photoautotrophic growth and the glycogen catabolic rate under dark anaerobisis (Kumaraswamy et al., 2013). The *Δldh* knockout was previously shown to improve H_2 production by 5-fold (McNeely et al., 2010). The single mutants, *gap1*$^+$ and *Δldh* were used as appropriate controls for the experiments. Even though individually, *ΔccmR, Δldh* or

gap1^{+} did not exhibit any growth defect (Fig. 4-2 A), (McNeely et al., 2010), (Kumaraswamy et al., 2013), the double and the triple mutants showed a 25% and 50% slower growth rate, respectively (Fig. 4-4), although they reached the same final cell density at stationary phase.

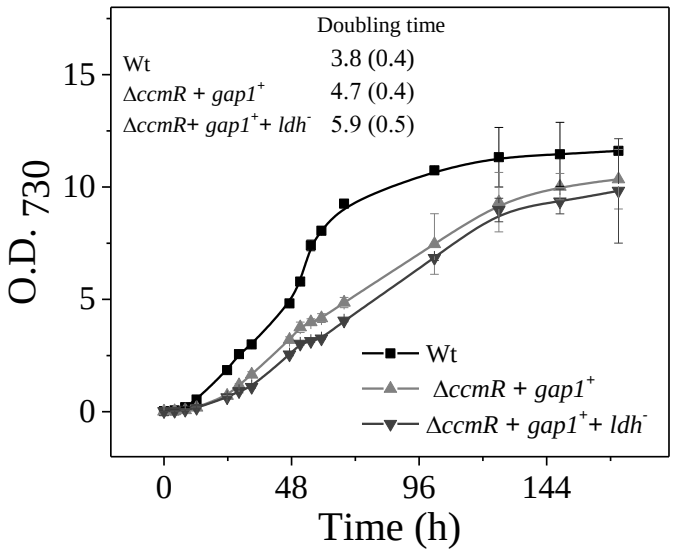

Figure 4-4 **Photoautotrophic phenotypes for mutants and Wt**. A) Growth curve of *ΔccmR* + *gap1*$^{+}$+ and *ΔccmR* + *gap1*$^{+}$+ *Δldh* and Wt. Data represents the mean of three biological replicates with standard error grown under 150 µE $m^{-2}s^{-1}$ illumination with constant bubbling of 2% CO_2. The inset shows the calculated doubling time based on fits to Gompertz curve.

H_2 production by the double and triple mutants was also measured via vial experiments (Fig. 4-3 B). The double mutant, (*ΔccmR* + *gap1*$^+$), produced about 2.5-3 fold higher H_2 than the WT strain and about 2-fold higher than the single mutants *ΔccmR* and *gap1*$^+$, respectively. The triple mutant (*ΔccmR* + *gap1*$^+$ + *Δldh*) produced about 6-8 fold higher H_2 than WT, 4-6 fold higher H_2 than Δ*ccmR* and *gap1*$^+$, and about 1-2 fold higher H_2 than the *ldh* strain. Thus, the overall the H_2 production rate was (*ΔccmR* + *gap1*$^+$ + *Δldh*) > *Δldh* > (*ΔccmR* + *gap1*$^+$) > *ΔccmR* > *gap1*$^+$ > WT, an inverse of the trend mirrored by the concentration of intracellular NAD(P)H. The dissolved H_2 production rate was measured continuously by electrochemical consumption under conditions when H_2 is not allowed to accumulate in the headspace. In this configuration the hydrogenase enzyme does not suffer from product inhibition that is otherwise observed in vial measurements. The kinetics from such a technique reflects the organismal rate of H_2 production. For this configuration, a homebuilt fuel-cell coupled to a fluorometer was used (Ananyev et al., 2012). The fuel cell consumes the produced H_2 (termed "milking"), shifting the equilibrium of the reaction $2H^+ + 2e^- \leftrightarrow H_2$ towards right, while the fluorometer measures the instantaneous changes in the intracellular NAD(P)H concentration in real-time parallel to the H_2 production. For the milking experiments, the measurements were limited to the 3 mutant strains in *ΔccmR* background.

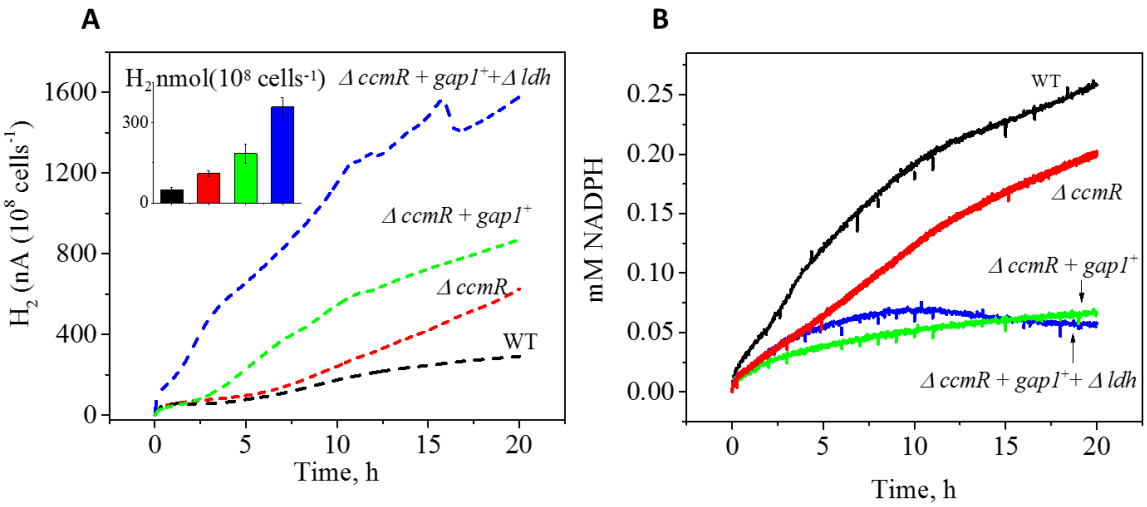

Figure 4-5 **Simultaneous detection of H_2 and NADH.** A) Excreted (extracellular) hydrogen oxidation current during 20 hrs of continuous dark anaerobic autofermentation is directly proportional to the rate of H_2 production ("Milking" conditions). Inset shows the yield of H_2 (nmol) at 20 h for the four strains (from integration of the curves and using Faraday's laws of electrolysis). (b) Simultaneous determination of the relative NAD(P)H fluorescence yield is directly proportional to the total concentration of intracellular reduced pyridine nucleotides under the same conditions as (A). The real time Data in (A) and (B) is one representative sample.

Within the first 20 h, all the strains produced about 50-fold higher H_2 (Fig. 4-5 A) than under the fixed headspace vial experiments (Fig. 4-3 B). Comparing across strains, the hydrogen production in the *ΔccmR* strain was about 2.3-fold higher than the WT, while the double and the triple mutants were 3.7 and 7.3 fold higher than the WT (Fig. 4-5 A). Simultaneous NAD(P)H fluorescence indicated that the highest intracellular levels were maintained in the WT cells with the lowest hydrogen production rate (Fig. 4-5 B), while in the *ΔccmR* mutant, the residual NADPH is lower, suggesting an improved consumption of reductant by hydrogenase. The double and the triple mutants show significantly lower amounts of residual reductant levels and corresponding higher H_2 production rate. Thus, taken together, there is a direct correspondence between higher H_2 production rate and lower intracellular NAD(P)H concentration is the four strains. Accordingly, the deletion of the *ccmR* gene, which upregulates the expression of hydrogenase genes, is an apparent response to elevated NAD(P)H availability and serves the purpose of a vent for elimination of excess reductant capacity as volatile H_2 gas.

3.4) Autofermentation products:

Because *nifJ* (PFOR) showed a 5.7-fold increase in expression (Table 4-2), additional fermentative pathways were also studied by quantifying excreted fermentative metabolites (acetate, lactate and pyruvate) using cell-free supernatants (Fig. 4-6 A-C) collected during the vial autofermentation experiments.

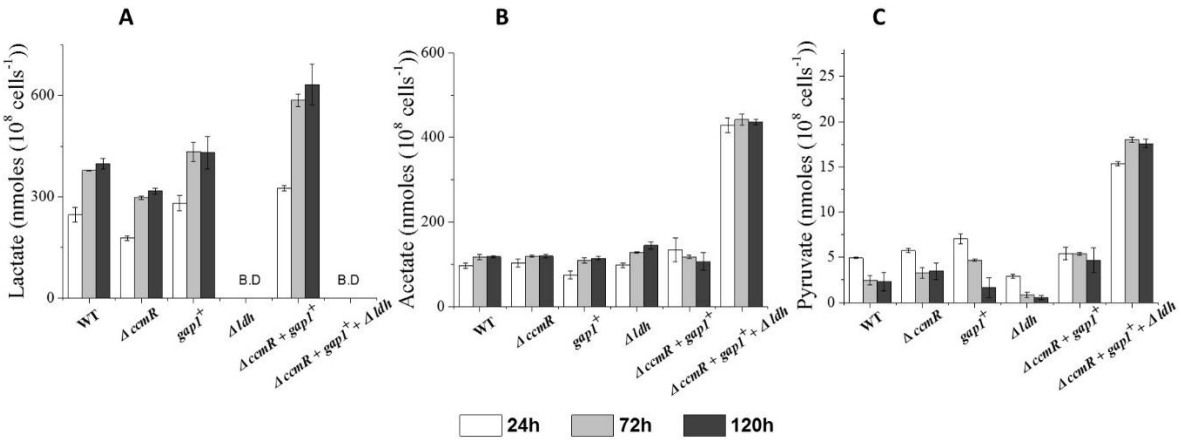

Figure 4-6 **The kinetics of autofermentative metabolite excretion measured over 120 h in sealed vials.** A) lactate, B) acetate and C) pyruvate present in the spent medium determined using HPLC. Data represents the mean and standard deviation of three biological replicates. B.D. = below detection limits

The *ΔccmR* mutant excreted about ~0.7-fold lower lactate as compared to the WT, while the double mutant (*ΔccmR* + *gap1*$^+$) excreted about 1.5-fold higher lactate, as compared to both the WT and the *gap1*$^+$ mutant strain. Finally, as expected, the *Δldh* and the triple mutant (Δ*ccmR* + *gap1*$^+$ + *Δldh*) did not show detectable levels of lactate in the extracellular medium (Fig. 4-6 A). All strains except for the triple mutant (Δ*ccmR* + *gap1*$^+$ + *Δldh)*, generated the same amount of acetate (~ 100 nmoles per 10^8 cells), as compared to the WT strain (Fig. 4-6 B), while the triple mutant produced 4-fold higher acetate levels compared to the WT. While all the strains had very low levels of excreted pyruvate (Fig. 4-6 C), the triple mutant (*ΔccmR*+ *gap1*$^+$ + *Δldh*), lacking the ability to excrete carbon as lactate, excreted about 3-7 fold higher levels of pyruvate as compared to the WT, suggesting that the loss of *ldh* and the overexpression of *gap1*, the cells are forced to excrete carbon through alternate pathways. The lactate/acetate ratio was found to be lower in the *ΔccmR* (1.5-2.5) than WT (2.5-3.5), suggesting a selective redirection of the glycolytically generated pyruvate into acetate rather than lactate in the mutant. Interestingly, the introduction of *gap1* overexpression selectively redirects the fermented carbon into lactate instead of acetate, and the same occurs when *gap1* is introduced in the *ΔccmR* background. However, on limiting the flux through lactate by deleting the lactate dehydrogenase gene in the triple mutant, the cells continue to break down glycogen, but now excrete significantly more pyruvate and acetate into the medium.

3.5) Glycolytic rate:

To investigate if the higher H_2 production in Δ*ccmR* was caused by higher hydrogenase activity or as a by-product of higher glycolytic rate leading to greater reductant production, we quantified the total intracellular reducing carbohydrate (TRC) as glucose equivalents using the anthrone assay (Fig.4-7). The cell pellets stored during the course of autofermentation were used for this purpose. Amongst the mutants, the triple mutant (*ΔccmR* + *gap1*$^+$ + *Δldh*) and the double mutant (Δ*ccmR* + *gap1*$^+$) accumulated the highest amounts of total reducing carbohydrate (TRC) equivalents during photoautotrophic growth (~1.2 μmoles glucose/10^8 cells) while the *ΔccmR* and

the WT strains had about ~0.8 μmoles glucose/10^8 cells at the start of dark anaerobisis (autofermentation). As shown previously, *gap1*$^+$ had a higher amount of TRC (0.95 μmoles glucose/10^8 cells) than WT. Linear fits to the TRC data gave the glycolytic rate (Fig. 4-7 B). In comparison, the *ΔccmR* strain had a marginally lower glycolytic rate (~15%) than the WT, although not statistically significant (p=0.3291). The introduction of *gap1* overexpression increased the glycolytic rate in the *ΔccmR* strain by about 60% more than the WT, consistent with previous results on single *gap1* ovexpression (Kumaraswamy et al., 2013). The *Δldh* strain had a 50% lower glycolytic rate, while as expected the *gap1*$^+$ had a 40% higher glycolytic rate. In summary, the results indicate that the loss of CcmR produces nearly no change in rate of anaerobic glycogen breakdown, in contrast to aerobic respiration, for which this rate is atleast 50% higher than the WT (Fig. 4-2 C, from respiration measurements). Additionally, these results also indicate that the gain in hydrogen in the *ΔccmR* mutant is indeed an effect of the increased hydrogenase activity, while that in the double and the triple mutant is a combined effect of higher glycolysis and higher hydrogenase activity.

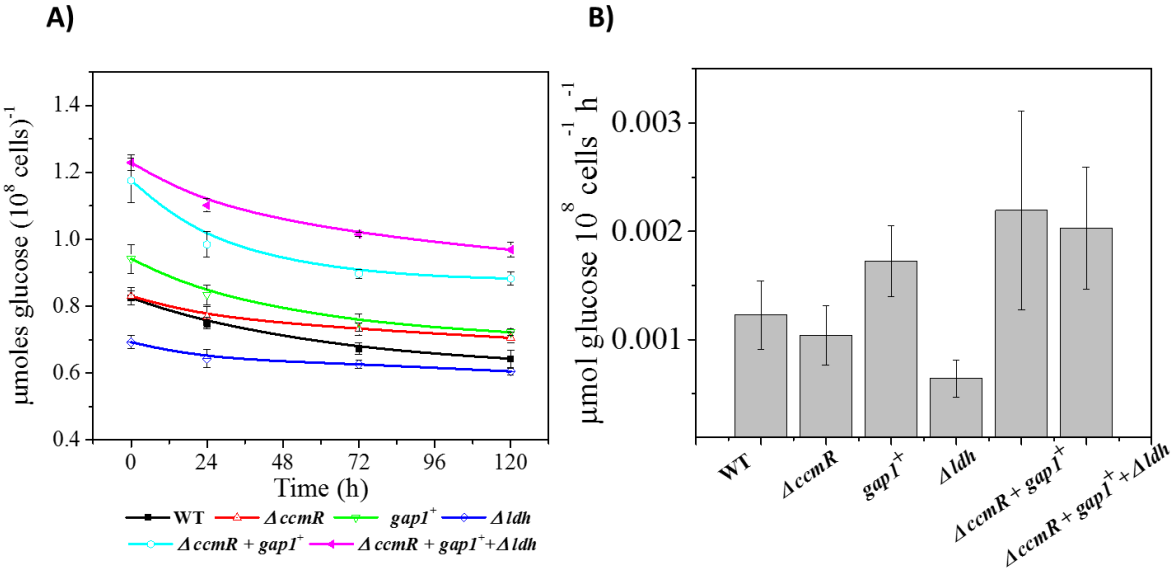

Figure 4-7 **Autofermentative catabolism of glycogen**.A) Autofermentative catabolism of glycogen. The total intracellular reducing carbohydrate content was measured via anthrone assay, following the dark anaerobic incubation at indicated time points. Data represents the mean and standard deviation of three biological replicates. B) Glycolytic rate. Data represents the fitted slope and standard error of three biological replicates calculated using GraphPad Prism6 statistical software.

3.6) Cellular energy charge:

To determine if the altered acetate production is accompanied by an increase in the cellular energy charge (CEC) or in the redox poise, the steady-state pool sizes of the adenylate energy carriers were measured by LC-MS/MS after 3 days of fermentation (Table 4-3). CEC was calculated as $CEC = (ATP + (0.5ADP))/(ATP + ADP + AMP)$, and redox poise as $(NAD(P)H)/(NAD(P))$. The *ccmR* mutant had neither a higher CEC nor a higher redox poise, even though lactate production was suppressed as compared to the WT. Both the double and the triple mutant had significantly higher CEC (Table 4-3) with unchanged redox poise.

	Wt	*ΔccmR*	*gap1*$^{+}$	*ldh*$^{-}$	*ΔccmR+ gap1*$^{+}$	*ΔccmR+ gap1*$^{+}$*ldh-*
AMP	2.7 (0.50)	3.4 (0.21)	3.2 (0.33)	3.3 (0.24)	3.2 (0.50)	1.9 (0.14)
ADP	0.39 (0.11)	0.53 (0.03)	0.99 (0.34)	0.58 (0.06)	1.8 (0.07)	1.0 (0.07)
ATP	0.09 (0.02)	0.08 (0.01)	0.38 (0.10)	0.16 (0.01)	0.98 (0.05)	0.82 (0.10)
CEC	**0.11 (0.01)**	**0.09 (0.01)**	**0.17 (0.01)**	**0.11 (0.01)**	**0.32 (0.06)**	**0.035 (0.07)**
NAD+	0.07 (0.01)	0.08 (0.01)	0.11 (0.02)	0.06 (0.01)	0.15 (0.01)	0.03 (0.00)
NADH	0.12 (0.01)	0.14 (0.05)	0.16 (0.03)	0.08 (0.02)	0.2 (0.03)	0.06 (0.01)
NADP+	0.01 (0.00)	0.03 (0.00)	0.04 (0.01)	0.03 (0.00)	0.12 (0.01)	0.03 (0.00)
NADPH	0.0 (0.00)	0.02 (0.00)	0.03 (0.01)	0.02 (0.00)	0.08 (0.01)	0.01 (0.01)
Redox poise	**1.5**	**1.6**	**1.3**	**1.2**	**1**	**1.2**

Table 4-3 LC-MS/MS results for adenylate and pyridine nucleotides. Values represent the concentration of the metabolites after 3 days of autofermentation calculated as µmoles per 10^8 cells. Experiment was performed on 4 biological replicates. Standard error of mean are represented in parentheses. CEC and redox poise calculation described in the Results section.

4. Discussion

4.1) CcmR *deletion remodels respiratory metabolism to enhance ATP production, but does not improve photoautotrophic growth under Ci sufficiency*

CcmR is a LysR-type transcription factor, which under Ci sufficient conditions, regulates the expression of the genes involved in carbon uptake (Woodger et al., 2007), (Price et al., 2008), (Daley et al., 2012), (Burnap et al., 2015). Loss of CcmR mimics a low Ci environment and is sufficient to derepress the genes involved in the high affinity Ci transport (Lieman-Hurwitz et al., 2009). The results presented here show that an increase in the Ci uptake genes (Table 4-2) does not guarantee an increase in overall growth under Ci sufficient conditions (Fig. 4-2 A). This is not unexpected as the CCM pathway has been previously suggested to decrease growth in air, not because of the lack of carbon but because of the high energetic demand for maintaining the high affinity CCM (Burnap et al., 2015). Depending on the mechanism, CCM-dependent Ci uptake may use 1 ATP, 1 proton or at least one NADPH per bicarbonate imported (Burnap et al., 2015), (Raven et al., 2014). To fulfill this higher requirement for ATP/ H^+, the oxidative phosphorylation pathway is preferred, a result supported by both the 50% higher respiration rate (Fig. 4-2 C), as well as enhanced expression of the subunits of respiratory Complex IV and Complex II (Table 4-2). Thus, the *ccmR* deletion strain appears to remodel its global photoautotrophic metabolism to enhance respiration and thus ATP production. The schematic representation of the overall changes occurring by the loss of *ccmR* is presented in Scheme 4-1.

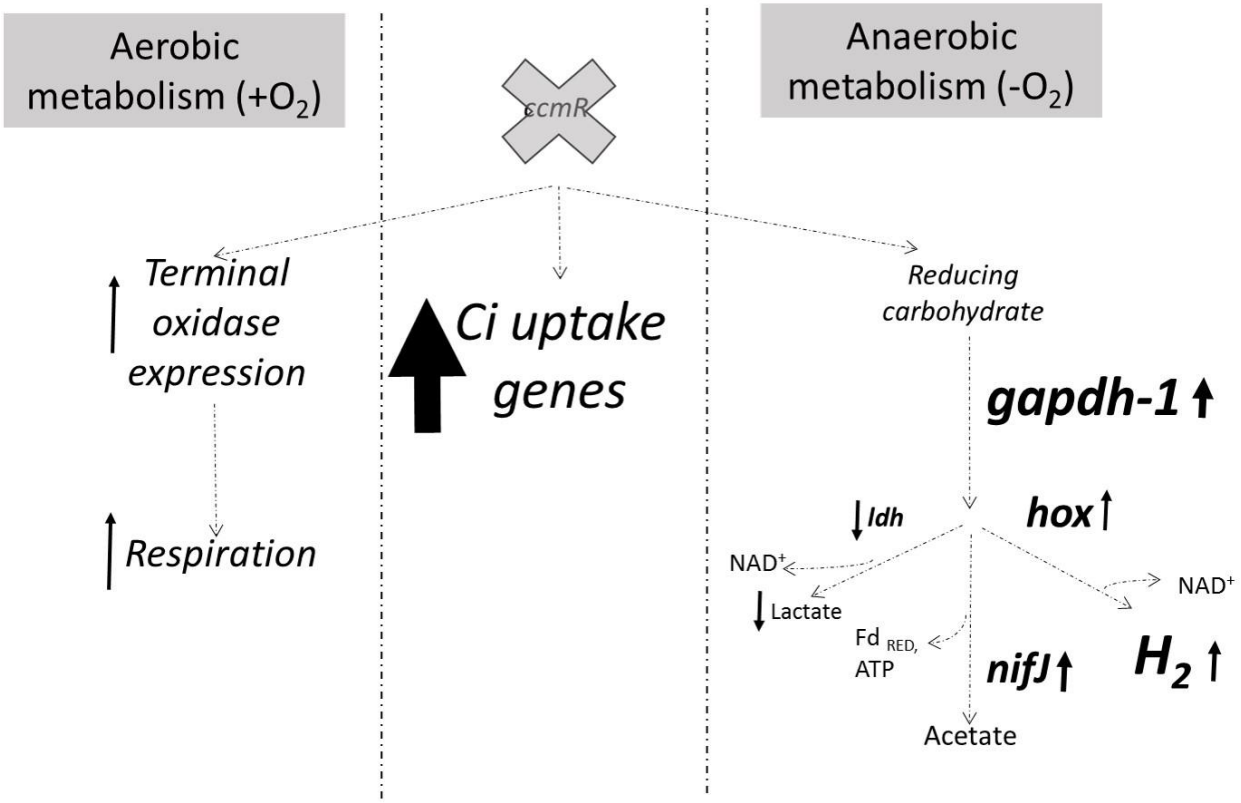

Scheme 4-1 **Schematic representation of key features of physiology and metabolism on the loss of ccmR in *Synechococcus* 7002**. Small and large font sizes are used for the various processes, metabolites and the gene expression to indicate the quantitative differences relative to the WT, with the fold size of 'Reducing carbohydrate' being 1. The solid up and down arrows qualitatively represent either the increase or the decrease in the process, metabolites or the gene expression relative to the WT.

4.2) Deletion of CcmR alters fermentative metabolism, enhances H_2 production and improves the flux of carbon towards acetate

Anaerobic metabolism in *ΔccmR* also occurs in a way as to maximally conserve the adenylate energy. Glycolysis, the dominant ATP-producing pathway under fermentative conditions, generates pyruvate as its end product. The generated pyruvate may have at least 2 dominant fates in *Synechococcus* 7002 (Fig. 1-2): a) reduction of pyruvate to lactate via lactate dehydrogenase with a concomitant oxidation of NADH, or b) conversion of pyruvate to acetyl-CoA using either pyruvate dehydrogenase (reduces NAD^+ to NADH) or via *nifJ* (reduces ferredoxin) (McNeely et al., 2011) . The acetyl-CoA can be converted to acetate producing ATP via substrate-level phosphorylation. At the metabolic level, the *ccmR* mutant strain still excretes lactate as the dominant fermentative end product than acetate (Fig. 4-6 A, B). However, comparing the fractions of excreted carbon as lactate and acetate between the mutant and the WT, a higher fraction of acetate is excreted in the *ΔccmR* strain. Consequently, *ΔccmR* redirects the catabolized carbohydrates into the acetogenic route (acetate) that generates ATP. In addition, transcripts for an alternate modified Embden-Meyerhof pathway using phosphoenolpyruvate synthase (*ppsA*), that converts phosphoenolpyruvate to pyruvate, is enhanced (3.6-fold) (Table 4-2). *ppsA* performs the same function as pyruvate kinase, but uses AMP as the substrate for ATP synthesis rather than ADP (Fig. 1-2) and is able to conserve a greater amount of energy as compared to the pyruvate kinase pathway. In addition, the rerouting of carbon flux through the *nifJ* pathway reduces ferredoxin which has a higher energy content than NADH produced by pyruvate dehydrogenase. This suggests that the normal glycolytic pathway may be replaced by the alternative pathway comprising *ppsA* and *nifJ* to conserve and maximize ATP and NADH, a result seen previously in *Synechococcus* 7002 under anoxic conditions (Ludwig and Bryant, 2011a). While a redirection of carbon to acetate occurs, the carbon partitioned into the lactate sink is diminished, which may be expected to cause an over-reduction of the electron carriers. *ΔccmR* maintains a steady redox poise

in vial experiments, while upon milking, the NAD(P)H levels are lowered as compared to the WT with improvements in hydrogenase activity. Therefore, we propose that to compensate for loss of carbon through lactate excretion, the cells enhance the carbon-neutral hydrogenase as a reductant vent in order to maintain redox homeostasis.

4.3) Insertion of gap1$^+$ overexpression removes the glycolytic chokepoint and improves H_2.

The loss of the *ccmR* expression resulted in an increase in the expression of hydrogenase genes as well as the hydrogenase activity – the *in vivo* hydrogenase activity as measured by headspace measurements increased by a modest 1.5- to 2-fold (Table 4-2, Fig. 4-3 B) and that under milking increased 2.3-fold (Fig. 4-5 A). Enhancing the glycolytic rate (Kumaraswamy et al., 2013) and removing alternate competing reductant sinks (McNeely et al., 2010) are proven methods to improve H_2 production further. The glycolytic bottleneck was alleviated by introducing *gap1* overexpression (Kumaraswamy et al., 2013) in the *ΔccmR* mutant strain, resulting in a 4-fold higher headspace H_2 production. This yield was further enhanced by the deletion of lactate dehydrogenase, resulting in 8-fold higher H_2 production. In both mutants containing *gap1* overexpression, the glycolytic rate and the glycogen accumulation improved (Fig. 4-7). This increase in glycolysis shifted the fermentative metabolism back towards lactate synthesis, while additional blocking of lactate biosynthesis in the *Δldh* strain causes excretion of pyruvate (Fig. 4-6 C). Interestingly, the *ΔccmR* strain itself has a 16-fold higher *gap1* gene expression (Table 4-2) with no improvement in the glycolytic rate (Fig. 4-7). However, when the *gap1* expression was artificially improved by introducing the overexpression construct, together with an increase in the total accumulated glycogen, it also resulted in an increase in the glycolytic rates and H_2 production. Taken together, loss of CcmR appears to regulate glycolysis tightly under fermentative conditions using hydrogenase as a vent for excess reducing equivalents. The introduction of *gap1*$^+$ appears to override the regulatory controls of glycolysis and gluconeogenesis, indicating that much higher GAPDH levels overcome the bottleneck in glycolysis.

4.4) Theoretical energy conversion efficiency (ECE):

The energy conversion efficiency (ECE) of fermentative H_2 production is the ratio of the combustion enthalpies of H_2 produced to that of the glucose consumed. Table 4-4 gives the glucose to H_2 molar conversion ratios and calculated ECE values for the WT, *ΔccmR*, (*ΔccmR* + *gap1*$^+$) and (*ΔccmR* + *gap1*$^+$ + *Δldh*) mutant under headspace measurements and under milking conditions. As exponential phase cultures were used in the study instead, the molar conversion ratios were significantly lower than the previously reported values for stationary cultures (McNeely et al., 2010). Autofermentation of the exponentially grown cells gave an ECE value of 0.34% for the WT strain (headspace measurement), which was improved to 1.8% upon milking. The *ΔccmR* mutant was found to have a higher ECE value than the WT under both non-milking (0.64%) and under milking (3.8% conditions) even though the glycolytic rate was marginally lower in the *ΔccmR* strain. Thus, the deletion of *ccmR* clearly results in improving the availability of reductant to hydrogenase. On the other hand, the double and the triple mutant had ECE values similar to the WT under non-milking conditions (0.53% and 1.3% respectively); however, upon milking, the ECE values increased to higher values of 4.2% and 8.9% respectively. These results are in complete agreement with the literature that the headspace accumulation does indeed limit H_2 production (McNeely et al., 2011), (Ananyev et al., 2012). The improvement in the ECE value between *ΔccmR* and WT clearly show that under non-milking conditions, introduction of *ΔccmR* deletion improves the availability of reductant to H_2, while introduction *gap1* overexpression increases the amount of reductant generated via glycolysis.

	WT	*ΔccmR*	*gap1*$^{+}$	*ldh*$^{-}$	*ΔccmR+ gap1*$^{+}$	*ΔccmR+ gap1*$^{+}$*ldh-*
Molar conversion (H2 mols/glucose mols) (headspace 120 h)	0.03	0.06	0.03	0.23	0.05	0.12
ECE (headspace 120 h)	0.34	0.64	0.34	2.4	0.53	1.3
Molar conversion (H2 mols/glucose mols)(milking 20h)	0.18	0.39	N.D	N.D	0.42	0.87
ECE (milking 20h)	1.8	3.9	N.D	N.D	4.2	8.9

Table 4-4. **Calculated energy conversion efficiency for H_2.** Calculated ECE values based on the H_2 produced to glycogen consumed under headspace and under milking conditions.

In conclusion, our results show that loss of *ccmR* gene expression remodels the fermentative carbon metabolism and uses hydrogenase as a terminal oxidase to rebalance excess reducing equivalents as volatile H_2. The CcmR deletion strain may serve as a good platform to improve H_2 production through further metabolic engineering.

Chapter 5: Conclusions

Understanding how microalgae partition photosynthetically fixed carbon into the terminal carbon sinks is fundamental for improving biofuel production. The objective of this thesis was to gain insights into the molecular basis of carbon partitioning in a model microalga *Chlamydomonas reinhardtii*. I have employed a series of starchless mutants in conjugation with nutrient starvation as a model system for modulating the normal carbon distribution in this microalga. In chapters 2 and 3, several experiments have been presented leading to a greater understanding of carbon partitioning and its coupling to photosynthesis. Chapter 4 is an example where prior knowledge of central carbon metabolism has been used to effectively enhance hydrogen production.

In chapter 2, we investigated the role of starch biosynthesis in affecting photosynthetic growth and carbon partitioning in *sta6*, a starchless mutant of *Chlamydomonas reinhardtii* lacking ADP-glucose pyrophosphorylase (AGPase). This mutant is unable to convert glucose-1-P to ADP-glucose, the precursor to starch biosynthesis. At the start of the project, we expected to observe that loss of starch biosynthesis would alter carbon partitioning among the other carbon products under photoautotrophic growth conditions. However, during the course of experimentation, we found that the mutant did not change its fraction of lipids and proteins but did produce 20% lower biomass. Probing the underlying mechanism revealed an intact photosynthetic electron transport chain in the mutant, but possessing a greatly attenuated rate of NADPH reoxidation and a 3 fold higher ATP pool size. This phenotype manifests only above a particular light threshold, indicating the importance of starch biosynthesis when excess energy is available and that, starch biosynthesis in *Chlamydomonas* plays a critical role in light energy storage and rebalancing energy.

As *sta6* did not exhibit an altered carbon partitioning under nutrient replete growing conditions, in chapter 3, we imposed nutrient starvation as a tool to shift microbial cellular metabolism to favor selected bioproducts. Prior work has shown that under nitrogen (N) starvation, *Chlamydomonas reinhardtii* redirects biosynthesis from proteins to starch and lipids, and in

mutants lacking starch biosynthesis genes, preferentially to lipids. Our results revealed three important metabolite nodes, 'the carbohydrate node', 'the TCA node' and 'the fatty acid node' that serve as indicators of possible flux changes during N starvation. Both transient ^{13}C-metabolite fluxes produced from fixed $H^{13}CO_3^-$ and steady-state metabolite pool sizes reveal reduced flux through the TCA cycle and increased flux through gluconeogenesis as system wide responses to N starvation in strains with or without starch biosynthesis. Interestingly, our results showed that even in the absence of starch biosynthesis, gluconeogenesis is the inherent response to N starvation. This is achieved by redirecting carbon into the oxidative pentose phosphate (OPP) pathway via G6P. Even though the use of OPP leads to a significant loss in CO_2, this pathway generates the additional reductant needed for lipid biosynthesis. Thus, the loss of starch biosynthesis forces a remodeling of metabolism that is necessary to increase the reductant available for lipid biosynthesis. Simultaneous measurements of adenylate nucleotides (ATP, ADP, AMP) revealed a tight correlation between elevated cellular energy charge (CEC) and the flux into gluconeogenesis. The three nodes and the CEC dependent changes of flux are important mutagenesis targets that could be explored further. From these studies of two starchless mutants, I conclude that together with the inherent (transcriptional/translational) response to nutrient stress, the energy requirements for the synthesis of the terminal carbon sink plays an important role in governing the metabolic fluxes. Thus, even in the absence of starch biosynthesis, gluconeogenesis is maintained and coupled to the oxidative pentose phosphate pathway to generate the excess reductant necessary for lipid biosynthesis. Therefore, in the future, modulating the ATP:NADPH ratio so as to improve the NADPH availability need to be devised to enhance the fluxes towards lipids.

In chapter 4, we enhanced biohydrogen production in a euryhaline cyanobacterium, *Synechococcus* sp. PCC 7002. We initiated our study with a carbon concentration mechanism mutant, CcmR. CcmR is a LysR-type transcriptional regulator that is known to represses the expression of genes encoding high-affinity components of the carbon concentration mechanism

(CCM) in cyanobacteria. Even though, CcmR was presumed to be unrelated to fermentative metabolism, prior results from our collaborator demonstrated that the inactivation of CcmR alters the expression of multiple fermentative genes, especially hydrogenase expression in *Synechococcus 7002*. Therefore, to test if the CCM affects dark anaerobic metabolism, we measured the kinetics of autofermentation in the wild type (WT) and the ccmR deletion strains of *Synechococcus* sp. PCC 7002, measuring both excreted metabolites by mass spectrometry and the intracellular concentration of NAD(P)H continuously by fluorescence. Upon fermentation, loss of CcmR resulted in a 1.5-fold increase in the *in vivo* hydrogenase activity, while continuous removal of produced H_2 (by milking) boosted H_2 production to 2.6-fold compared to the Wt. Further, by sequentially increasing glycolytic rate and removing alternate competing pathways, we were able to metabolically engineer the CcmR strain and further boost H_2 production levels by 6-8-fold above that from the wild type strain.

Taken together, the results from my thesis, furthers our understanding of carbon partitioning while simultaneously providing proof of concept of how targeted metabolic engineering can help in improving productivity. The carbohydrate node (DHAP-FBP junction) described in chapter 3 is definitely worth exploring as metabolic engineering target to modulate carbon partitioning between terminal sinks. The elucidation of the regulatory mechanisms would help make algal biofuels both commercially viable as well as a sustainable alternative fuel.

References:

Ananyev, G. and Dismukes, G. C. (2005) How fast can Photosystem II split water? Kinetic performance at high and low frequencies. *Photosynthesis Research,* **84**, (1-3), 355-365.

Ananyev, G. M., Skizim, N. J. and Dismukes, G. C. (2012) Enhancing biological hydrogen production from cyanobacteria by removal of excreted products. *J Biotechnol,* **162**, (1), 97-104.

Axelsson, R. and Lindblad, P. (2002) Transcriptional regulation of Nostoc hydrogenases: Effects of oxygen, hydrogen, and nickel. *Appl Environ Microb,* **68**, (1), 444-447.

Badger, M. R. and Price, G. D. (2003) CO2 concentrating mechanisms in cyanobacteria: molecular components, their diversity and evolution. *J Exp Bot,* **54**, (383), 609-622.

Badger, M. R., Price, G. D., Long, B. M. and Woodger, F. J. (2006) The environmental plasticity and ecological genomics of the cyanobacterial CO2 concentrating mechanism. *J Exp Bot,* **57**, (2), 249-265.

Ball, S. G., Dirick, L., Decq, A., Martiat, J. C. and Matagne, R. F. (1990) Physiology of Starch Storage in the Monocellular Alga Chlamydomonas-Reinhardtii. *Plant Science,* **66**, (1), 1-9.

Ballicora, M. A., Iglesias, A. A. and Preiss, J. (2004) ADP-glucose pyrophosphorylase: a regulatory enzyme for plant starch synthesis. *Photosynthesis Research,* **79**, (1), 1-24.

Batan, L., Quinn, J., Willson, B. and Bradley, T. (2010) Net Energy and Greenhouse Gas Emission Evaluation of Biodiesel Derived from Microalgae. *Environ Sci Technol,* **44**, (20), 7975-7980.

Becker, E. W. (1994). Microalgae: Biotechnology and Microbiology, Cambridge University Press.

Becker, E. W. (1994). Microalgae: Biotechnology and Microbiology, Cambridge Univeristy Press.

Benamotz, A., Tornabene, T. G. and Thomas, W. H. (1985) Chemical Profile of Selected Species of Microalgae with Emphasis on Lipids. *Journal of Phycology,* **21**, (1), 72-81.

Bennette, N. B., Eng, J. F. and Dismukes, G. C. (2011) An LC-MS-Based Chemical and Analytical Method for Targeted Metabolite Quantification in the Model Cyanobacterium Synechococcus sp. PCC 7002. *Analytical Chemistry,* **83**, (10), 3808-3816.

Blaby, I. K., Glaesener, A. G., Mettler, T., Fitz-Gibbon, S. T., Gallaher, S. D., Liu, B., Boyle, N. R., Kropat, J., Stitt, M., Johnson, S., Benning, C., Pellegrini, M., Casero, D. and Merchant, S. S. (2013) Systems-level analysis of nitrogen starvation-induced modifications of carbon metabolism in a Chlamydomonas reinhardtii starchless mutant. *Plant Cell,* **25**, (11), 4305-4323.

Boyle, N. R. and Morgan, J. A. (2009) Flux balance analysis of primary metabolism in Chlamydomonas reinhardtii. *BMC systems biology,* **3**, 4.

Boyle, N. R., Page, M. D., Liu, B. S., Blaby, I. K., Casero, D., Kropat, J., Cokus, S. J., Hong-Hermesdorf, A., Shaw, J., Karpowicz, S. J., Gallaher, S. D., Johnson, S., Benning, C., Pellegrini, M., Grossman, A. and Merchant, S. S. (2012) Three Acyltransferases and Nitrogen-responsive Regulator Are Implicated in Nitrogen Starvation-induced Triacylglycerol Accumulation in Chlamydomonas. *J Biol Chem,* **287**, (19), 15811-15825.

Brennan, L. and Owende, P. (2010) Biofuels from microalgae-A review of technologies for production, processing, and extractions of biofuels and co-products. *Renew Sust Energ Rev,* **14**, (2), 557-577.

Breuer, G., de Jaeger, L., Artus, V. P. G., Martens, D. E., Springer, J., Draaisma, R. B., Eggink, G., Wijffels, R. H. and Lamers, P. P. (2014) Superior triacylglycerol (TAG) accumulation in starchless mutants of Scenedesmus obliquus: (II) evaluation of TAG yield and productivity in controlled photobioreactors. *Biotechnol Biofuels,* **7**.

Breuer, G., Lamers, P. P., Martens, D. E., Draaisma, R. B. and Wijffels, R. H. (2012) The impact of nitrogen starvation on the dynamics of triacylglycerol accumulation in nine microalgae strains. *Bioresource Technol,* **124**, 217-226.

Brune, D. E., Lundquist, T. J. and Benemann, J. R. (2009) Microalgal Biomass for Greenhouse Gas Reductions: Potential for Replacement of Fossil Fuels and Animal Feeds. *J Environ Eng,* **135**, (11), 1136-1144.

Burnap, R. L., Hagemann, M. and Kaplan, A. (2015) Regulation of CO2 Concentrating Mechanism in Cyanobacteria. *Life*, **5**, (1), 348-371.
Campbell, P. K., Beer, T. and Batten, D. (2011) Life cycle assessment of biodiesel production from microalgae in ponds. *Bioresource Technol*, **102**, (1), 50-56.
Cardol, P., Forti, G. and Finazzi, G. (2011) Regulation of electron transport in microalgae. *Bba-Bioenergetics*, **1807**, (8), 912-918.
Caspar, T., Huber, S. C. and Somerville, C. (1985) Alterations in Growth, Photosynthesis, and Respiration in a Starchless Mutant of Arabidopsis thaliana (L.) Deficient in Chloroplast Phosphoglucomutase Activity. *Plant Physiol*, **79**, (1), 11-17.
Cerovic, Z. G., Bergher, M., Goulas, Y., Tosti, S. and Moya, I. (1993) Simultaneous Measurement of Changes in Red and Blue Fluorescence in Illuminated Isolated-Chloroplasts and Leaf Pieces - the Contribution of Nadph to the Blue Fluorescence Signal. *Photosynthesis Research*, **36**, (3), 193-204.
Chen, J. H. and Jones, R. F. (1971) Molecular properties of multiple forms of phosphoenolpyruvate carboxylase from Chlamydomonas reinhardtii. *Biochimica et biophysica acta*, **229**, (1), 208-215.
Chisti, Y. (2007) Biodiesel from microalgae. *Biotechnology Advances*, **25**, (3), 294-306.
Chisti, Y. (2008) Biodiesel from microalgae beats bioethanol. *Trends Biotechnol*, **26**, (3), 126-131.
Chisti, Y. (2013) Constraints to commercialization of algal fuels. *J Biotechnol*, **167**, (3), 201-214.
Daley, S. M. E., Kappell, A. D., Carrick, M. J. and Burnap, R. L. (2012) Regulation of the Cyanobacterial CO2-Concentrating Mechanism Involves Internal Sensing of NADP(+) and alpha-Ketogutarate Levels by Transcription Factor CcmR. *Plos One*, **7**, (7).
Dauvillee, D., Colleoni, C., Mouille, G., Morell, M. K., d'Hulst, C., Wattebled, F., Lienard, L., Delvalle, D., Ral, J. P., Myers, A. M. and Ball, S. G. (2001) Biochemical characterization of wild-type and mutant isoamylases of Chlamydomonas reinhardtii supports a function of the multimeric enzyme organization in amylopectin maturation. *Plant Physiol*, **125**, (4), 1723-1731.
Dismukes, G. C., Carrieri, D., Bennette, N., Ananyev, G. M. and Posewitz, M. C. (2008) Aquatic phototrophs: efficient alternatives to land-based crops for biofuels. *Curr Opin Biotech*, **19**, (3), 235-240.
Fan, J., Andre, C. and Xu, C. (2011) A chloroplast pathway for the de novo biosynthesis of triacylglycerol in Chlamydomonas reinhardtii. *Febs Lett*, **585**, (12), 1985-1991.
Fan, J. L., Yan, C. S., Andre, C., Shanklin, J., Schwender, J. and Xu, C. C. (2012) Oil accumulation is controlled by carbon precursor supply for fatty acid synthesis in Chlamydomonas reinhardtii. *Plant and Cell Physiology*, **53**, (8), 1380-1390.
Figge, R. M., Cassier-Chauvat, C., Chauvat, F. and Cerff, R. (2001) Characterization and analysis of an NAD(P)H dehydrogenase transcriptional regulator critical for the survival of cyanobacteria facing inorganic carbon starvation and osmotic stress. *Mol Microbiol*, **39**, (2), 455-468.
Fishman, D., Majumdar, R., Morello, J., Pate, R. and Yang, J. (2010). National Algal Biofuels Technology Roadmap. N. R. E. Laboratory. Maryland.
Frigaard, N. U., Sakuragi, Y. and Bryant, D. A. (2004) Gene inactivation in the cyanobacterium *Synechococcus* sp. PCC 7002 and the green sulfur bacterium *Chlorobium tepidum* using in vitro-made DNA constructs and natural transformation. *Methods Mol. Biol.*, **274**, (29), 325-340.
Geigenberger, P. (2011) Regulation of Starch Biosynthesis in Response to a Fluctuating Environment. *Plant Physiol*, **155**, (4), 1566-1577.
Genty, B., Briantais, J. M. and Baker, N. R. (1989) The Relationship between the Quantum Yield of Photosynthetic Electron-Transport and Quenching of Chlorophyll Fluorescence. *Biochim Biophys Acta*, **990**, (1), 87-92.
Georgianna, D. R. and Mayfield, S. P. (2012) Exploiting diversity and synthetic biology for the production of algal biofuels. *Nature*, **488**, (7411), 329-335.

Gfeller, R. P. and Gibbs, M. (1984) Fermentative Metabolism of Chlamydomonas-Reinhardtii .1. Analysis of Fermentative Products from Starch in Dark and Light. *Plant Physiol*, **75**, (1), 212-218.
Gimpel, J. A., Specht, E. A., Georgianna, D. R. and Mayfield, S. P. (2013) Advances in microalgae engineering and synthetic biology applications for biofuel production. *Curr Opin Chem Biol*, **17**, (3), 489-495.
Goodenough, U., Blaby, I., Casero, D., Gallaher, S. D., Goodson, C., Johnson, S., Lee, J. H., Merchant, S. S., Pellegrini, M., Roth, R., Rusch, J., Singh, M., Umen, J. G., Weiss, T. L. and Wulan, T. (2014) The Path to Triacylglyceride Obesity in the sta6 Strain of Chlamydomonas reinhardtii. *Eukaryot Cell*, **13**, (5), 591-613.
Goodenough, U., Blaby, I., Casero, D., Gallaher, S. D., Goodson, C., Johnson, S., Lee, J. H., Merchant, S. S., Pellegrini, M., Roth, R., Rusch, J., Singh, M., Umen, J. G., Weiss, T. L. and Wulan, T. (2014) The Path to Triacylglyceride Obesity in the sta6 Strain of Chlamydomonas reinhardtii. *Eukaryot Cell*.
Goodson, C., Roth, R., Wang, Z. T. and Goodenough, U. (2011) Structural correlates of cytoplasmic and chloroplast lipid body synthesis in Chlamydomonas reinhardtii and stimulation of lipid body production with acetate boost. *Eukaryot Cell*, **10**, (12), 1592-1606.
Griffiths, M. J. and Harrison, S. T. L. (2009) Lipid productivity as a key characteristic for choosing algal species for biodiesel production. *J Appl Phycol*, **21**, (5), 493-507.
Grundel, M., Scheunemann, R., Lockau, W. and Zilliges, Y. (2012) Impaired glycogen synthesis causes metabolic overflow reactions and affects stress responses in the cyanobacterium Synechocystis sp. PCC 6803. *Microbiology*, **158**, (Pt 12), 3032-3043.
Guschina, I. A. and Harwood, J. L. (2006) Lipids and lipid metabolism in eukaryotic algae. *Progress in Lipid Research*, **45**, (2), 160-186.
Guy, R. D., Vanlerberghe, G. C. and Turpin, D. H. (1989) Significance of Phosphoenolpyruvate Carboxylase during Ammonium Assimilation: Carbon Isotope Discrimination in Photosynthesis and Respiration by the N-Limited Green Alga Selenastrum minutum. *Plant Physiol*, **89**, (4), 1150-1157.
Hannon, M., Gimpel, J., Tran, M., Rasala, B. and Mayfield, S. (2010) Biofuels from algae: challenges and potential. *Biofuels*, **1**, (5), 763-784.
Harris, E. H. and Stern, D. (2009). The chlamydomonas sourcebook [electronic resource].
Hassid, W. Z. and Abraham, S. (1957) Chemical procedures for analysis of polysaccharides. *Methods in Enzymology*, **3**, 34-50.
Hasunuma, T., Harada, K., Miyazawa, S. I., Kondo, A., Fukusaki, E. and Miyake, C. (2010) Metabolic turnover analysis by a combination of in vivo C-13-labelling from (CO2)-C-13 and metabolic profiling with CE-MS/MS reveals rate-limiting steps of the C-3 photosynthetic pathway in Nicotiana tabacum leaves. *J Exp Bot*, **61**, (4), 1041-1051.
Hu, Q., Sommerfeld, M., Jarvis, E., Ghirardi, M., Posewitz, M., Seibert, M. and Darzins, A. (2008) Microalgal triacylglycerols as feedstocks for biofuel production: perspectives and advances. *Plant J*, **54**, (4), 621-639.
Huppe, H. C. and Buchanan, B. B. (1989) Activation of a Chloroplast Type of Fructose Bisphosphatase from Chlamydomonas-Reinhardtii by Light-Mediated Agents. *Z Naturforsch C*, **44**, (5-6), 487-494.
Illman, A. M., Scragg, A. H. and Shales, S. W. (2000) Increase in Chlorella strains calorific values when grown in low nitrogen medium. *Enzyme Microb Tech*, **27**, (8), 631-635.
Johnson, X. and Alric, J. (2012) Interaction between Starch Breakdown, Acetate Assimilation, and Photosynthetic Cyclic Electron Flow in Chlamydomonas reinhardtii. *J Biol Chem*, **287**, (31), 26445-26452.
Johnson, X. and Alric, J. (2013) Central Carbon Metabolism and Electron Transport in Chlamydomonas reinhardtii: Metabolic Constraints for Carbon Partitioning between Oil and Starch. *Eukaryot Cell*, **12**, (6), 776-793.

Kaplan, A. and Reinhold, L. (1999) Co2 Concentrating Mechanisms in Photosynthetic Microorganisms. *Annu Rev Plant Physiol Plant Mol Biol*, **50**, 539-570.
Kaplan, A., Schwarz, R., Lieman-Hurwitz, J. and Reinhold, L. (1991) Physiological and molecular aspects of the inorganic carbon-concentrating mechanism in cyanobacteria. *Plant Physiol*, **97**, (3), 851-855.
Kenchappa, K. G., Guerra, T., Qian, X., Zhang, S., Bryan, D. and Dismukes, G. C. (2013) Reprogramming the Glycolytic Pathway for Increased Hydrogen Production in Cyanobacteria: Metabolic Engineering of NAD+-dependent GAPDH *Energ Environ Sci*.
King, P. W., Posewitz, M. C., Ghirardi, M. L. and Seibert, M. (2006) Functional studies of [FeFe] hydrogenase maturation in an Escherichia coli biosynthetic system. *J Bacteriol*, **188**, (6), 2163-2172.
Kiss, E., Kos, P. B. and Vass, I. (2009) Transcriptional regulation of the bidirectional hydrogenase in the cyanobacterium Synechocystis 6803. *J Biotechnol*, **142**, (1), 31-37.
Kramer, D. M. and Evans, J. R. (2011) The Importance of Energy Balance in Improving Photosynthetic Productivity. *Plant Physiol*, **155**, (1), 70-78.
Krishnan, A., Kumaraswamy, G. K., Vinyard, D. J., Gu, H., Ananyev, G., Posewitz, M. C. and Dismukes, G. C. (2015) Metabolic and photosynthetic consequences of blocking starch biosynthesis in the green alga Chlamydomonas reinhardtii sta6 mutant. *The Plant journal : for cell and molecular biology*, **81**, (6), 947-960.
Kumaraswamy, G. K., Guerra, T., Qian, X., Zhang, S. Y., Bryant, D. A. and Dismukes, G. C. (2013) Reprogramming the glycolytic pathway for increased hydrogen production in cyanobacteria: metabolic engineering of NAD(+)-dependent GAPDH. *Energ Environ Sci*, **6**, (12), 3722-3731.
Li, H. and Durbin, R. (2009) Fast and accurate short read alignment with Burrows–Wheeler transform. *Bioinformatics*, **25**, (14), 1754-1760.
Li, Y., Han, D., Hu, G., Dauvillee, D., Sommerfeld, M., Ball, S. and Hu, Q. (2010) Chlamydomonas starchless mutant defective in ADP-glucose pyrophosphorylase hyper-accumulates triacylglycerol. *Metab Eng*, **12**, (4), 387-391.
Li, Y., Han, D., Hu, G., Sommerfeld, M. and Hu, Q. (2010) Inhibition of starch synthesis results in overproduction of lipids in Chlamydomonas reinhardtii. *Biotechnol Bioeng*, **107**, (2), 258-268.
Li, Y. T., Han, D. X., Hu, G. R., Dauvillee, D., Sommerfeld, M., Ball, S. and Hua, Q. (2010) Chlamydomonas starchless mutant defective in ADP-glucose pyrophosphorylase hyper-accumulates triacylglycerol. *Metab Eng*, **12**, (4), 387-391.
Liang, M. H. and Jiang, J. G. (2013) Advancing oleaginous microorganisms to produce lipid via metabolic engineering technology. *Prog Lipid Res*, **52**, (4), 395-408.
Lieman-Hurwitz, J., Haimovich, M., Shalev-Malul, G., Ishii, A., Hihara, Y., Gaathon, A., Lebendiker, M. and Kaplan, A. (2009) A cyanobacterial AbrB-like protein affects the apparent photosynthetic affinity for CO2 by modulating low-CO2-induced gene expression. *Environ Microbiol*, **11**, (4), 927-936.
Ludewig, F., Sonnewald, U., Kauder, F., Heineke, D., Geiger, M., Stitt, M., Muller-Rober, B. T., Gillissen, B., Kuhn, C. and Frommer, W. B. (1998) The role of transient starch in acclimation to elevated atmospheric CO2. *Febs Lett*, **429**, (2), 147-151.
Ludwig, M. and Bryant, D. A. (2011) Transcription profiling of the model cyanobacterium Synechococcus sp strain PCC 7002 by Next-Gen (SOLiD (TM)) sequencing of cDNA. *Front Microbiol*, **2**.
Ludwig, M. and Bryant, D. A. (2011) Transcription profiling of the model cyanobacterium *Synechococcus* sp. strain PCC 7002 by Next-Gen (SOLiD) sequencing of cDNA. *Front. Microbiol.*, **2**, (41), 41.

Ludwig, M. and Bryant, D. A. (2012) Acclimation of the global transcriptome of the cyanobacterium Synechococcus sp strain PCC 7002 to nutrient limitations and different nitrogen sources. *Front Microbiol*, **3**.
Maxwell, K. and Johnson, G. N. (2000) Chlorophyll fluorescence - a practical guide. *J Exp Bot*, **51**, (345), 659-668.
McKendry, P. (2002) Energy production from biomass (part 2): conversion technologies. *Bioresource Technol*, **83**, (1), 47-54.
McKendry, P. (2002) Energy production from biomass (part 3): gasification technologies. *Bioresource Technol*, **83**, (1), 55-63.
McNeely, K., Xu, Y., Ananyev, G., Bennette, N., Bryant, D. A. and Dismukes, G. C. (2011) Synechococcus sp. Strain PCC 7002 nifJ Mutant Lacking Pyruvate:Ferredoxin Oxidoreductase. *Appl Environ Microb*, **77**, (7), 2435-2444.
McNeely, K., Xu, Y., Bennette, N., Bryant, D. A. and Dismukes, G. C. (2010) Redirecting Reductant Flux into Hydrogen Production via Metabolic Engineering of Fermentative Carbon Metabolism in a Cyanobacterium. *Appl Environ Microb*, **76**, (15), 5032-5038.
Meier, R. L. (1955). Biological Cycles in the Transformation of Solar Energy into Useful Fuels., Madison University Wisconsin Press.
Melis, A. (2002) Green alga hydrogen production: progress, challenges and prospects. *Int J Hydrogen Energ*, **27**, (11-12), 1217-1228.
Melis, A. (2009) Solar energy conversion efficiencies in photosynthesis: Minimizing the chlorophyll antennae to maximize efficiency. *Plant Sci*, **177**, (4), 272-280.
Melis, A. (2013) Carbon partitioning in photosynthesis. *Curr Opin Chem Biol*, **17**, (3), 453-456.
Meuser, J. E., D‚ÄôAdamo, S., Jinkerson, R. E., Mus, F., Yang, W., Ghirardi, M. L., Seibert, M., Grossman, A. R. and Posewitz, M. C. (2012) Genetic disruption of both Chlamydomonas reinhardtii [FeFe]-hydrogenases: Insight into the role of HYDA2 in H2 production. *Biochemical and Biophysical Research Communications*, **417**, (2), 704-709.
Mi, H. L., Klughammer, C. and Schreiber, U. (2000) Light-induced dynamic changes of NADPH fluorescence in Synechocystis PCC 6803 and its ndhB-defective mutant M55. *Plant Cell Physiol*, **41**, (10), 1129-1135.
Miao, X. L. and Wu, Q. Y. (2004) High yield bio-oil production from fast pyrolysis by metabolic controlling of Chlorella protothecoides. *J Biotechnol*, **110**, (1), 85-93.
Miller, R., Wu, G. X., Deshpande, R. R., Vieler, A., Gartner, K., Li, X. B., Moellering, E. R., Zauner, S., Cornish, A. J., Liu, B. S., Bullard, B., Sears, B. B., Kuo, M. H., Hegg, E. L., Shachar-Hill, Y., Shiu, S. H. and Benning, C. (2010) Changes in Transcript Abundance in Chlamydomonas reinhardtii following Nitrogen Deprivation Predict Diversion of Metabolism. *Plant Physiol*, **154**, (4), 1737-1752.
Moellering, E. R. and Benning, C. (2010) RNA interference silencing of a major lipid droplet protein affects lipid droplet size in Chlamydomonas reinhardtii. *Eukaryot Cell*, **9**, (1), 97-106.
Morris, D. L. (1948) Quantitative determination of carbohydrates with Dreywood's anthrone reagent. *Science*, **107**, (2775), 254-255.
Mouille, G., Maddelein, M. L., Libessart, N., Talaga, P., Decq, A., Delrue, B. and Ball, S. (1996) Preamylopectin processing: A mandatory step for starch biosynthesis in plants. *Plant Cell*, **8**, (8), 1353-1366.
Msanne, J., Xu, D., Konda, A. R., Casas-Mollano, J. A., Awada, T., Cahoon, E. B. and Cerutti, H. (2012) Metabolic and gene expression changes triggered by nitrogen deprivation in the photoautotrophically grown microalgae Chlamydomonas reinhardtii and Coccomyxa sp. C-169. *Phytochemistry*, **75**, 50-59.
Omata, T., Gohta, S., Takahashi, Y., Harano, Y. and Maeda, S. (2001) Involvement of a CbbR homolog in low CO2-induced activation of the bicarbonate transporter operon in cyanobacteria. *J Bacteriol*, **183**, (6), 1891-1898.

Ott, T., Clarke, J., Birks, K. and Johnson, G. (1999) Regulation of the photosynthetic electron transport chain. *Planta,* **209**, (2), 250-258.

Pienkos, P. T. and Darzins, A. (2009) The promise and challenges of microalgal-derived biofuels. *Biofuel Bioprod Bior,* **3**, (4), 431-440.

Porra, R. J., Thompson, W. A. and Kriedemann, P. E. (1989) Determination of Accurate Extinction Coefficients and Simultaneous-Equations for Assaying Chlorophyll-a and Chlorophyll-B Extracted with 4 Different Solvents - Verification of the Concentration of Chlorophyll Standards by Atomic-Absorption Spectroscopy. *Biochim Biophys Acta,* **975**, (3), 384-394.

Price, G. D., Badger, M. R., Woodger, F. J. and Long, B. M. (2008) Advances in understanding the cyanobacterial CO(2)-concentrating-mechanism (CCM): functional components, Ci transporters, diversity, genetic regulation and prospects for engineering into plants. *J Exp Bot,* **59**, (7), 1441-1461.

Radakovits, R., Jinkerson, R. E., Darzins, A. and Posewitz, M. C. (2010) Genetic Engineering of Algae for Enhanced Biofuel Production. *Eukaryotic Cell,* **9**, (4), 486-501.

Radakovits, R., Jinkerson, R. E., Fuerstenberg, S. I., Tae, H., Settlage, R. E., Boore, J. L. and Posewitz, M. C. (2012) Draft genome sequence and genetic transformation of the oleaginous alga Nannochloropis gaditana. *Nature communications,* **3**, 686.

Ramazanov, A. and Ramazanov, Z. (2006) Isolation and characterization of a starchless mutant of Chlorella pyrenoidosa STL-PI with a high growth rate, and high protein and polyunsaturated fatty acid content. *Phycol Res,* **54**, (4), 255-259.

Raven, J. A. (1982) The Energetics of Fresh-Water Algae - Energy-Requirements for Biosynthesis and Volume Regulation. *New Phytol,* **92**, (1), 1-20.

Raven, J. A., Beardall, J. and Giordano, M. (2014) Energy costs of carbon dioxide concentrating mechanisms in aquatic organisms. *Photosynth Res,* **121**, (2-3), 111-124.

Richmond, A. (2004). Handbook of microalgal culture: biotechnology and applied phycology, Blackwell Science Ltd.

Rittmann, B. E. (2008) Opportunities for renewable bioenergy using microorganisms. *Biotechnology and Bioengineering,* **100**, (2), 203-212.

Rodolfi, L., Chini Zittelli, G., Bassi, N., Padovani, G., Biondi, N., Bonini, G. and Tredici, M. R. (2009) Microalgae for oil: strain selection, induction of lipid synthesis and outdoor mass cultivation in a low-cost photobioreactor. *Biotechnol Bioeng,* **102**, (1), 100-112.

Schenk, P. M., Thomas-Hall, S. R., Stephens, E., Marx, U. C., Mussgnug, J. H., Posten, C., Kruse, O. and Hankamer, B. (2008) Second Generation Biofuels: High-Efficiency Microalgae for Biodiesel Production. *Bioenerg Res,* **1**, (1), 20-43.

Schreiber, U., Gademann, R., Ralph, P. J. and Larkum, A. W. D. (1997) Assessment of photosynthetic performance of Prochloron in Lissoclinum patella in hospite by chlorophyll fluorescence measurements. *Plant and Cell Physiology,* **38**, (8), 945-951.

Sharkey, T. D., Stitt, M., Heineke, D., Gerhardt, R., Raschke, K. and Heldt, H. W. (1986) Limitation of Photosynthesis by Carbon Metabolism .2. O-2-Insensitive Co2 Uptake Results from Limitation of Triose Phosphate Utilization. *Plant Physiol,* **81**, (4), 1123-1129.

Sharma, K. K., Schuhmann, H. and Schenk, P. M. (2012) High Lipid Induction in Microalgae for Biodiesel Production. *Energies,* **5**, (5), 1532-1553.

Sheehan, J., Dunahay, T, Benemann, J, Roessler, P. (1998). A look back at the US Department of Energy's Aquatic Species Program—biodiesel from algae. Golden, National Renewable Energy Laboratory.

Siaut, M., Cuine, S., Cagnon, C., Fessler, B., Nguyen, M., Carrier, P., Beyly, A., Beisson, F., Triantaphylides, C., Li-Beisson, Y. and Peltier, G. (2011) Oil accumulation in the model green alga Chlamydomonas reinhardtii: characterization, variability between common laboratory strains and relationship with starch reserves. *BMC Biotechnol,* **11**, 7.

Siaut, M., Cuine, S., Cagnon, C., Fessler, B., Nguyen, M., Carrier, P., Beyly, A., Beisson, F., Triantaphylides, C., Li-Beisson, Y. H. and Peltier, G. (2011) Oil accumulation in the model green alga Chlamydomonas reinhardtii: characterization, variability between common laboratory strains and relationship with starch reserves. *Bmc Biotechnol,* **11**.

Stevens, S. E., Patterson, C. O. P. and Myers, J. (1973) The production of hydrogen peroxide by blue-green algae: a survey. *Journal of Phycology,* **9**, 427-430.

Stitt, M. and Quick, P. (1989) Photosynthetic Carbon Partitioning - Its Regulation and Possibilities for Manipulation. *Physiol Plantarum,* **77**, (4), 633-641.

Subramanian, S., Barry, A. N., Pieris, S. and Sayre, R. T. (2013) Comparative energetics and kinetics of autotrophic lipid and starch metabolism in chlorophytic microalgae: implications for biomass and biofuel production. *Biotechnol Biofuels,* **6**.

Subramanian, S., Barry, A. N., Pieris, S. and Sayre, R. T. (2013) Comparative energetics and kinetics of autotrophic lipid and starch metabolism in chlorophytic microalgae: implications for biomass and biofuel production. *Biotechnol Biofuels,* **6**, (1), 150.

Sun, A., Davis, R., Starbuck, M., Ben-Amotz, A., Pate, R. and Pienkos, P. T. (2011) Comparative cost analysis of algal oil production for biofuels. *Energy,* **36**, (8), 5169-5179.

Sun, J. D., Okita, T. W. and Edwards, G. E. (1999) Modification of carbon partitioning, photosynthetic capacity, and O-2 sensitivity in arabidopsis plants with low ADP-glucose pyrophosphorylase activity. *Plant Physiol,* **119**, (1), 267-276.

Suzuki, E., Ohkawa, H., Moriya, K., Matsubara, T., Nagaike, Y., Iwasaki, I., Fujiwara, S., Tsuzuki, M. and Nakamura, Y. (2010) Carbohydrate Metabolism in Mutants of the Cyanobacterium Synechococcus elongatus PCC 7942 Defective in Glycogen Synthesis. *Applied and Environmental Microbiology,* **76**, (10), 3153-3159.

Toepel, J., McDermott, J. E., Summerfield, T. C. and Sherman, L. A. (2009) Transcriptional Analysis of the Unicellular, Diazotrophic Cyanobacterium Cyanothece Sp Atcc 51142 Grown under Short Day/Night Cycles. *Journal of Phycology,* **45**, (3), 610-620.

Tornabene, T. G., Holzer, G., Lien, S. and Burris, N. (1983) Lipid-Composition of the Nitrogen Starved Green-Alga Neochloris-Oleoabundans. *Enzyme Microb Tech,* **5**, (6), 435-440.

Venteris, E. R., Skaggs, R. L., Coleman, A. M. and Wigmosta, M. S. (2013) A GIS Cost Model to Assess the Availability of Freshwater, Seawater, and Saline Groundwater for Algal Biofuel Production in the United States. *Environ Sci Technol,* **47**, (9), 4840-4849.

Vinyard, D. J., Zachary, C. E., Ananyev, G. and Dismukes, G. C. (2013) Thermodynamically accurate modeling of the catalytic cycle of photosynthetic oxygen evolution: A mathematical solution to asymmetric Markov chains. *Biochimica Et Biophysica Acta-Bioenergetics,* **1827**, (7), 861-868.

Wang, H. L., Postier, B. L. and Burnap, R. L. (2004) Alterations in global patterns of gene expression in Synechocystis sp PCC 6803 in response to inorganic carbon limitation and the inactivation of ndhR, a LysR family regulator. *J Biol Chem,* **279**, (7), 5739-5751.

Wang, Z. T., Ullrich, N., Joo, S., Waffenschmidt, S. and Goodenough, U. (2009) Algal Lipid Bodies: Stress Induction, Purification, and Biochemical Characterization in Wild-Type and Starchless Chlamydomonas reinhardtii. *Eukaryotic Cell,* **8**, (12), 1856-1868.

Wang, Z. T., Ullrich, N., Joo, S., Waffenschmidt, S. and Goodenough, U. (2009) Algal lipid bodies: stress induction, purification, and biochemical characterization in wild-type and starchless Chlamydomonas reinhardtii. *Eukaryot Cell,* **8**, (12), 1856-1868.

Wase, N., Black, P. N., Stanley, B. A. and DiRusso, C. C. (2014) Integrated Quantitative Analysis of Nitrogen Stress Response in Chlamydomonas reinhardtii Using Metabolite and Protein Profiling. *J Proteome Res,* **13**, (3), 1373-1396.

Weise, S. E., van Wijk, K. J. and Sharkey, T. D. (2011) The role of transitory starch in C-3, CAM, and C-4 metabolism and opportunities for engineering leaf starch accumulation. *J Exp Bot,* **62**, (9), 3109-3118.

Wiessner, W., Schnepf, E. and Starr, R. C. (1995). Algae, Environment and Human Affairs. Bristol, Biopress Ltd.

Wijffels, R. H. and Barbosa, M. J. (2010) An outlook on microalgal biofuels (vol 10, pg 67, 2008). *Science,* **330**, (6006), 913-913.

Williams, P. J. L. and Laurens, L. M. L. (2010) Microalgae as biodiesel & biomass feedstocks: Review & analysis of the biochemistry, energetics & economics. *Energ Environ Sci,* **3**, (5), 554-590.

Woodger, F. J., Bryant, D. A. and Price, G. D. (2007) Transcriptional regulation of the CO2-concentrating mechanism in a euryhaline, coastal marine cyanobacterium, Synechococcus sp strain PCC 7002: Role of NdhR/CcmR. *J Bacteriol,* **189**, (9), 3335-3347.

Work, V. H., Radakovits, R., Jinkerson, R. E., Meuser, J. E., Elliott, L. G., Vinyard, D. J., Laurens, L. M., Dismukes, G. C. and Posewitz, M. C. (2010) Increased lipid accumulation in the Chlamydomonas reinhardtii sta7-10 starchless isoamylase mutant and increased carbohydrate synthesis in complemented strains. *Eukaryot Cell,* **9**, (8), 1251-1261.

Work, V. H., Radakovits, R., Jinkerson, R. E., Meuser, J. E., Elliott, L. G., Vinyard, D. J., Laurens, L. M. L., Dismukes, G. C. and Posewitz, M. C. (2010) Increased Lipid Accumulation in the Chlamydomonas reinhardtii sta7-10 Starchless Isoamylase Mutant and Increased Carbohydrate Synthesis in Complemented Strains. *Eukaryotic Cell,* **9**, (8), 1251-1261.

Yang, S., Matsen, J. B., Konopka, M., Green-Saxena, A., Clubb, J., Sadilek, M., Orphan, V. J., Beck, D. and Kalyuzhnaya, M. G. (2013) Global Molecular Analyses of Methane Metabolism in Methanotrophic Alphaproteobacterium, Methylosinus trichosporium OB3b. Part II. Metabolomics and 13C-Labeling Study. *Frontiers in microbiology,* **4**, 70.

Yuan, J., Bennett, B. D. and Rabinowitz, J. D. (2008) Kinetic flux profiling for quantitation of cellular metabolic fluxes. *Nature protocols,* **3**, (8), 1328-1340.

Zabawinski, C., Van den Koornhuyse, N., D'Hulst, C., Schlichting, R., Giersch, C., Delrue, B., Lacroix, J. M., Preiss, J. and Ball, S. (2001) Starchless mutants of Chlamydomonas reinhardtii lack the small subunit of a heterotetrameric ADP-glucose pyrophosphorylase. *J Bacteriol,* **183**, (3), 1069-1077.

Zakrzhevskii, D. A., Ananyev, G. A. and Gerts, S. M. (1978) Kinetics of oxygen evolution by Chlorella cells ducing the initial period of illumination. *Soviet plant physiology,* **25**, 653-658

Zhang, S. and Bryant, D. A. (2015) Biochemical validation of the glyoxylate cycle in the cyanobacterium *Chlorogloeopsis fritschii* strain PCC 9212. *J. Biol. Chem.*, **In press**.

Zhu, S. N., Huang, W., Xu, J., Wang, Z. M., Xu, J. L. and Yuan, Z. H. (2014) Metabolic changes of starch and lipid triggered by nitrogen starvation in the microalga Chlorella zofingiensis. *Bioresource Technol,* **152**, 292-298.

Zwietering, M. H., Jongenburger, I., Rombouts, F. M. and Vantriet, K. (1990) Modeling of the Bacterial-Growth Curve. *Applied and Environmental Microbiology,* **56**, (6), 1875-1881.